



저작자표시-비영리-변경금지 2.0 대한민국

이용자는 아래의 조건을 따르는 경우에 한하여 자유롭게

- 이 저작물을 복제, 배포, 전송, 전시, 공연 및 방송할 수 있습니다.

다음과 같은 조건을 따라야 합니다:



저작자표시. 귀하는 원저작자를 표시하여야 합니다.



비영리. 귀하는 이 저작물을 영리 목적으로 이용할 수 없습니다.



변경금지. 귀하는 이 저작물을 개작, 변형 또는 가공할 수 없습니다.

- 귀하는, 이 저작물의 재이용이나 배포의 경우, 이 저작물에 적용된 이용허락조건을 명확하게 나타내어야 합니다.
- 저작권자로부터 별도의 허가를 받으면 이러한 조건들은 적용되지 않습니다.

저작권법에 따른 이용자의 권리는 위의 내용에 의하여 영향을 받지 않습니다.

이것은 [이용허락규약\(Legal Code\)](#)을 이해하기 쉽게 요약한 것입니다.

[Disclaimer](#)

공학박사 학위논문

**Triton Burnup Analyses with  
Fusion Neutron Measurements for  
1 MeV Triton Confinement Study in KSTAR**

KSTAR에서의 1 MeV 트리톤 가둠 특성 연구를 위한  
핵융합 중성자 측정을 이용한 트리톤 연소 해석

2019년 8월

서울대학교 대학원  
에너지시스템공학부  
조 정 민

# **Triton Burnup Analyses with Fusion Neutron Measurements for 1 MeV Triton Confinement Study in KSTAR**

지도 교수 황 용 석

이 논문을 공학박사 학위논문으로 제출함

2019 년 8 월

서울대학교 대학원

에너지시스템공학부

조 정 민

조정민의 박사 학위논문을 인준함

2019 년 8 월

위 원 장 \_\_\_\_\_ 나 용 수 \_\_\_\_\_ (인)

부위원장 \_\_\_\_\_ 황 용 석 \_\_\_\_\_ (인)

위 원 \_\_\_\_\_ 정 경 재 \_\_\_\_\_ (인)

위 원 \_\_\_\_\_ 천 문 성 \_\_\_\_\_ (인)

위 원 \_\_\_\_\_ 김 정 희 \_\_\_\_\_ (인)

## **Abstract**

# **Triton Burnup Analyses with Fusion Neutron Measurements for 1 MeV Triton Confinement Study in KSTAR**

Jungmin Jo

Department of Energy Systems Engineering

(Fusion & Plasma Engineering)

The Graduate School

Seoul National University

Understanding the 3.5 MeV alpha particle confinement physics in deuterium (D) – tritium (T) fusion plasma is important in terms of achieving burning plasma which is internal heating dominant and for vacuum vessel wall protection. The kinetic property of 1 MeV triton which is generated by the d-d fusion reaction is similar to that of 3.5 MeV fusion alpha particle. Thus it can be useful as a test particle to simulate a certain characteristics of the alpha particle in the D-T plasma.

A fraction of the produced 1 MeV fusion triton cannot be confined inside the bulk plasma and promptly loss to the wall due to its large drift orbit. Confined tritons without prompt loss, slowed down via Coulomb collision with background plasma and became thermalize. During the slowing down, secondary fusion reaction with background deuteron can occur and the 14 MeV d-t neutron can be produced. This secondary fusion reaction is called triton burnup and the d-t neutron from the triton burnup is called triton

burnup neutron (TBN). Among the produced tritons, about 1% of tritons are burned-up and produce TBN. Two branches in d-d fusion reactions, 2.5 MeV neutron production branch and 1 MeV triton production branch, have nearly the same reaction cross-section, thus the birth rate of triton can be determined by 2.5 MeV neutron emission rate. Thus triton burnup ratio can be determined by d-d neutron and TBN measurements in deuterium plasma.

As the peak energy of the d-t fusion reaction cross-section is located at triton energy of about 170 keV, which is lower than the triton birth energy (1 MeV), the emission of TBN is affected by certain events that occur during the slowing down, as well as prompt loss. Thus the overall confinement characteristics of triton can be deduced from the triton burnup ratio.

For the confinement study of 1 MeV triton under various high performance plasma experiment in KSTAR, diagnostics for d-d neutron and TBN measurements are developed, and in order to analyze the measurements analyses codes are prepared. By using developed diagnostics triton burnup ratio is measured and analyzed based on the codes.

The diagnostics are composed of shot-integrated neutron yield diagnostics and time-resolved neutron emission rate diagnostics. The neutron yield of d-d neutron and TBN during the plasma discharge duration time is measured by neutron activation system (NAS). For d-d neutron yield measurement, indium sample has been used since 2011 campaign. For TBN yield measurement silicon sample which is selected based on the neutronics calculation is utilized. At the position of counting station, there is a background gamma-ray which is exactly the same energy with the gamma-ray radiated from the

activated silicon sample. The background gamma-ray can interfere sample gamma counting and also evaluation of TBN yield. By using routinely available neutron flux monitor, the effect of the background gamma-ray on sample gamma counting is evaluated without separate measurement of the background gamma-ray. The activity of the silicon sample is evaluated by considering the effect of the background.

The time resolved d-d neutron and TBN emission rates are measured by using scintillation detectors. For simultaneous measurements of d-d neutron and TBN, organic scintillator is chosen. Two organic scintillators, stilbene and NE213 are operated independently. Each organic scintillator is optically coupled with a photo-multiplier tube (PMT). An irradiation test is carried out at accelerator based d-t neutron generator and appropriate PMT bias voltage level is determined which is adequate for analog input range of a digitizer. The digitizer can record the raw-waveform of triggered pulse during preset recording time window. The recorded data are offline processed then triggered time, induced charge and pulse shape information are extracted. Based on the charge comparison method, neutron and gamma-ray signals are discriminated. The discrimination performance is evaluated in terms of figure of merit and misclassification probability. For a total charge range of 0.6 V·ns or more, the probability of containing gamma-ray signal in the neutron branch is less than 0.1%.

For cross-check of TBN emission rate measurements from organic scintillators and for future high time resolution TBN diagnostics development, two scintillating fiber detectors are installed and tested. From its operation principle, the scintillating fiber detector can produce larger pulse signal only for the d-t neutron. Thus TBN signal can be discriminated

by setting discrimination level in pulse height. From the test results on KSTAR plasma discharges whose triton birth rate and confinement characteristics are expected to be different, clearly different pulse height spectra are observed in the expected way. Based on this difference the discrimination level for TBN is determined.

A good linearity is found between TBN yield from NAS and shot-integrated TBN counts from each TBN emission rate detectors. Based on this linearity, TBN ranges in each detector is absolutely calibrated. There is also good linearity between d-d yield from NAS and shot-integrated d-d counts from the organic scintillators. Each organic scintillator d-d neutron range is absolutely calibrated based on the linearity.

In order to analyze measured triton burnup ratio, two codes are prepared. One is for prompt loss calculation and the other is for slowing down and burnup calculation. Prompt loss characteristics is evaluated by using full gyro-orbit following code Lorentz orbit (LORBIT) and plasma equilibrium data. A prompt loss rate on each flux surface is derived based on the statistically evaluated prompt loss rate on the 680 points in a poloidal cross-section. The calculations of slowing down and d-t fusion reaction of confined triton are carried out by using newly developed code based on previous studies in other devices. In this code, it is assumed that each triton is slowed down on their birth position via Coulomb interaction with background plasma. Additionally, in this code volume averaged effective diffusion coefficient can be evaluated in semi-empirical way.

The estimated triton burnup ratio using analyses tools and assumed plasma parameters increases as plasma current and slowing down time increase, as expected from the classical burnup theory. The measured triton burnup ratio from NAS also increases as

plasma current increases. Within the same plasma current however, a deviation is observed. The deviation can be caused by combined effect among the different plasma current density profile, triton birth profile and MHD activities.

More detailed analyses are carried out by using time resolved measurement results on triton burnup ratio from the scintillation detector. The target plasma is the discharge #21695 where the Alfvén instability control experiment was carried out. The analysis timing is 7.4 s when the instability is mitigated. At this timing, there is no strong amplitude MHD activity which can degrade the confinement of 1 MeV triton, therefore it is good to compare with the expected triton burnup ratio from the classical burnup theory. The  $I_p$  of this discharge is 0.5 MA and the amount of prompt loss is expected to be large. The confined triton density ( $n_t$ ) at this timing is evaluated based on the confined fraction profile from LORBIT calculation, triton birth profile from TRANSP calculation, and measured d-d fusion neutron emission rate. Since d-t fusion reaction cross-section peak position is located lower than the birth energy of the triton, the calculation of the slowing down and burnup is carried out under the assumption that the plasma condition is retained for 0.6 s, which is the triton slowing down time in the plasma condition. The estimated triton burnup ratio based on the above process is consistent with the measurement within measurement error.

From the present study, the diagnostic systems are developed to measure the triton burnup ratio, and the codes for measured triton burnup analyses are prepared. In KSTAR deuterium plasma discharge, the triton burnup ratio is measured by using the developed diagnostics and analyzed using the prepared codes. The measured and estimated triton

burnup ratio, under the quiescent and high prompt loss rate (~87%) plasma condition, are in a good agreement within measurement error. From this result, it might be inferred that the confinement characteristics of triton in KSTAR stable plasma condition can be explained through the classical theory.

The developed diagnostics can be routinely operated in various high performance experiments in KSTAR and database of triton burnup in various condition can be established. Triton confinement characteristics can be deduced from the database by using the analyses codes, and based on the deduced characteristics 3.5 MeV alpha behavior can be inferred.

**Keywords: fusion plasma, 1 MeV triton, triton burnup, triton burnup neutron, d-d neutron, neutron diagnostics, KSTAR, Neutron activation system, Scintillation detector, Plasma diagnostics, Energetic particle confinement**

**Student Number: 2014-31126**

# Contents

<b>Abstract</b>	<b>i</b>
<b>Contents</b>	<b>vii</b>
<b>List of Tables</b> .....	<b>ix</b>
<b>List of Figures</b> .....	<b>x</b>
<b>Chapter 1. Introduction</b> .....	<b>1</b>
1.1. 3.5 MeV alpha from d-t fusion reaction.....	1
1.2. 1 MeV triton from d-d fusion reaction.....	2
1.3. Motivation.....	8
1.4. Objective and approach.....	9
<b>Chapter 2. Fusion neutron diagnostics</b> .....	<b>11</b>
2.1. Neutron activation system (NAS).....	11
2.1.1. Operation principle.....	11
2.1.2. Experimental setup.....	14
2.1.3. Neutron yield evaluation.....	18
2.1.3.1. KSTAR neutron transport model.....	18
2.1.3.2. d-d neutron yield.....	19
2.1.3.3. Triton burnup neutron yield.....	22
2.2. Scintillation detectors.....	30
2.2.1. Overview of the system.....	30
2.2.2. Organic scintillators: NE213 and stilbene.....	32
2.2.2.1. Operation principle.....	32
2.2.2.2. Experimental setup.....	34
2.2.2.2.1. Scintillator and photo-detector.....	34
2.2.2.2.2. Digitizer.....	38
2.2.2.2.3. Radiation shielding and installation in KSTAR.....	42

2.2.2.3. Operation stability and discrimination level setting .....	53
2.2.3. Scintillating fiber detector.....	72
<b>Chapter 3. Triton burnup analyses tools .....</b>	<b>80</b>
3.1. Prompt loss calculation.....	80
3.1.1. Lorentz Orbit code .....	80
3.1.2. Confined fraction calculation result.....	82
3.2. Slowing down and burnup calculation .....	89
3.2.1. Governing equation and calculation scheme .....	89
3.2.2. Ad-hoc diffusive model .....	94
3.2.3. Slowing down and burnup calculation result.....	97
<b>Chapter 4. Analyses of triton burnup in KSTAR.....</b>	<b>99</b>
4.1. Analyses of NAS measured result.....	99
4.2. Analyses of the scintillation detector result .....	103
<b>Chapter 5. Summary and conclusion .....</b>	<b>112</b>
<b>Bibliography .....</b>	<b>115</b>
<b>국 문 초 록.....</b>	<b>124</b>

## **List of Tables**

Table 1.1 Kinetic properties of 1 MeV triton, 3.5 MeV alpha and 100 keV deuteron. .....	2
Table 2.1 Discrimination ranges for d-d neutron and triton burnup neutron in the organic scintillation detectors. ....	68
Table 3.1 Coefficient for d-t fusion reaction cross-section [6] .....	90

## List of Figures

Figure 1.1 Drift orbits of 3.5 MeV alpha (left) and 1 MeV triton (right) in the same initial birth position and pitch ( $v_{  }/v$ ) condition. ....	3
Figure 1.2 D(t,n) $\alpha$ reaction cross-section according to the triton energy. Cross-section reached its maximum value at around 170 keV [8]. ....	4
Figure 2.1 The overall layout of KSTAR NAS [34]. Counter-clockwise from top left, irradiation end, capsule position monitoring system at the irradiation end and the capsule, pneumatic transfer system and counting station, and transfer line. ....	14
Figure 2.2 The cross-section of $^{115}\text{In}(n,n')^{115m}\text{In}$ reaction [45] .....	16
Figure 2.3 The cross-section of $^{28}\text{Si}(n,p)^{28}\text{Al}$ reaction [45] .....	17
Figure 2.4 Measured gamma-ray spectrum from activated indium sample which irradiated during the discharge #20939. The radiation cooling time was 13201 s, and gamma counting time was 5000 s. ....	20
Figure 2.5 (a) d-d neutron yield and (b) d-d neutron average emission rate from NAS with indidium sample. In the error bar, only counting error is included.....	21
Figure 2.6 Measured gamma-ray spectrum from activated silicon sample which irradiated during discharge #21574. Radiation cooling time and gamma-ray counting time were 56 s and 500 s respectively. ....	23
Figure 2.7 Background gamma spectrum at the KSTAR NAS counting station right after the typical neutral beam injected plasma discharge [46].	24
Figure 2.8 Evaluated $\beta$ value in different plasma discharges. For neutron flux monitor data, the stilbene detector neutron branch data is used (Ch. 2.2.2). For the background gamma counts the 1779 keV gamma-peak is fitted by Gaussian function. In order to have good fitting result,	

background was measured when discharge (NB heated) time is over 15 s. In all the cases the error from the evaluated gamma peak area by Gaussian fitting is less than 5%. The error bar in the figure contains gamma peak fitting error and stilbene data counting error both. ....27

Figure 2.9 (a) Triton burnup neutron yield and (b) average emission rate from NAS silicon sample measurements during 2018 KSTAR campaign. The average neutron emission rate is evaluated by the yield divided by neutral beam injection duration time. In the error bar sample gamma counting error and error in background radiation compensation are included. ....29

Figure 2.10 Schematic diagram for operation principle of organic scintillator. ..33

Figure 2.11 Pulse height spectrum of neutron branch of the NE213 detector. Data obtained by APV8104- 14MW (Techno-AP). Bias voltage of PMT is -1400 V. ....36

Figure 2.12 Pulse height spectrum of neutron branch of the stilbene detector. Data obtained by APV8104- 14MW (Techno-AP). Bias voltage setting of PMT: (a) -650 V, gain $\sim 4.5 \times 10^4$ , (b) -700 V, gain $\sim 1 \times 10^5$ . For bias voltage of -675 V the gain is  $\sim 6.5 \times 10^4$ . ....37

Figure 2.13 Photo of NKFADC500 .....39

Figure 2.14 Example of the recorded waveform of stilbene scintillation detector. ....40

Figure 2.15 The baseline variation in recorded pulses. ....40

Figure 2.16 (a) A changes of  $Q_{total}$  of induced pulse on H11934-100-10 PMT according to the repetition rate and pulse height. (b) The same data but the amount of variation in  $Q_{total}$  according to the repetition rate is expressed by the difference from the  $Q_{total}$  at the 10 kHz repetition rate condition. ....44

Figure 2.17 Radiation shielding of NE213 scintillation detector. From the inside, the detector is surrounded by 10 mm thickness soft iron, lead blocks and boron-polyethylene blocks for magnetic field, gamma-ray and neutron shielding respectively.....	48
Figure 2.18 (a) Radiation shielding of stilbene scintillation detector and (b) inside of the stilbene detector radiation shielding .....	50
Figure 2.19 Diagnostic cubicle .....	51
Figure 2.20 Installation position of each component, a: NE213 detector, b: stilbene detector, c: diagnostic cubicle and d: NE213 test position .....	52
Figure 2.21 Two-dimensional histogram of PSD value as function of $Q_{total}$ . In this plot, all the data points recorded during the plasma discharge #21711 by stilbene detector are used. If some specific time information is required, this kind of 2D histogram also can be made by using data points which contained in that time-interval. Since neutron signal has larger tail charge to total charge ratio, i.e. larger PSD value, the neutron branch is located in the higher PSD value ( $> 0.14$ ), and the gamma-ray branch is located in the lower PSD value ( $< 0.14$ ). .....	54
Figure 2.22 Linearity check between NE213 scintillation detector and fission chamber [62] .....	56
Figure 2.23 Linearity check between stilben scintillation detector and NE213 ..	57
Figure 2.24 Plasma discharge #21711. Two different counting rate regions are shown. The time range in each region is set so that the number of counts in each region is similar.....	59
Figure 2.25 One-dimensional histogram of PSD in specific $Q_{total}$ range. Figure of merit (FOM) = $D/(FWHM_{\gamma} + FWHM_n)$ .....	60
Figure 2.26 Misclassification probability in the neutron branch. ....	61
Figure 2.27 FOM and misclassification probability of NE213 detector in each	

counting rate region. ....	63
Figure 2.28 FOM and misclassification probability of stilbene detector in each counting rate region. ....	64
Figure 2.29 Energy histograms of NE213 detector neutron branch signal in each counting rate region. The total counts in each counting rate region is normalized to 1. The maximum $Q_{total}$ of d-d neutron can be derived from the intercept point between the extended energy histogram slope and the horizontal axis. Changes in maximum $Q_{total}$ of d-d neutron according to pulse counting rate is about 5%. ....	66
Figure 2.30 Energy histograms of stilbene detector neutron branch signal in each counting rate region. The total counts in each counting rate region is normalized to 1. The maximum $Q_{total}$ of d-d neutron can be derived from the intercept point between the extended energy histogram slope and the horizontal axis. Changes in maximum $Q_{total}$ of d-d neutron according to pulse counting rate is about 2.7%. ....	67
Figure 2.31 Time-resolved measurements of d-d neutron and TBN in two organic scintillators, NE213 (up) and stilbene (down). ....	69
Figure 2.32 Shot-integrated NE213 TBN counts versus TBN yield from NAS Si measurement. ....	70
Figure 2.33 Shot-integrated stilbene TBN counts versus TBN yield from NAS Si measurement. ....	71
Figure 2.34 Shot-integrated stilbene d-d counts versus d-d neutron yield from NAS In sample measurement. ....	71
Figure 2.35 Schematic diagram for operation principle of scintillating fiber detector. ....	72
Figure 2.36 Photos of installed scintillating fiber detectors (a) LANL Sci-Fi and (b) Toyama Sci-Fi ....	74

Figure 2.37 Photo of LANL Sci-Fi detector .....	74
Figure 2.38 Photo of Toyama Sci-Fi detector .....	75
Figure 2.39 Shot-integrated pulse height spectra of LANL Sci-Fi detector on three different plasma discharge scenarios. In NB-heated discharge with $I_p$ of 0.7 MA showed clearly different pulse height spectrum. Based on this difference, threshold level for triton burnup neutron signal is determined.....	77
Figure 2.40 Shot-integrated pulse height spectra of Toyama Sci-Fi on three different plasma discharge scenarios. Similar with LANL Sci-Fi result, in the NB-heated discharge with $I_p$ of 0.7 MA showed clearly different pulse height spectrum. Based on this difference, threshold level for triton burnup neutron signal is determined. ....	78
Figure 2.41 Shot-integrated TBN counts of LANL Sci-Fi and Toyama Sci-fi versus TBN yield from NAS Si measurement. ....	79
Figure 3.1 (a) Calculated confined fraction distribution in poloidal cross-section (interpolated result based on the calculated confined fraction on 680 positions) at KSTAR #21695, 7400 ms. The horizontal axis is radial position (m) and vertical axis is vertical position (m). (b) Plasma equilibrium at this timing.....	82
Figure 3.2 Calculated confined fraction distribution in poloidal cross-section (interpolated result based on the calculated confined fraction on 680 positions) in different plasma current cases (0.4 MA: #21756, 8900 ms, 0.6 MA: #21629, 5650 ms, 0.9 MA: #21655, 8800 ms). The horizontal axis is radial position (m) and vertical axis is vertical position (m).....	83
Figure 3.3 Interpolated result of calculated confined fraction distribution as a function of pitch and radial position at the $z=0$ position (discharge	

#21695, 7.4 s).....	84
Figure 3.4 Interpolated result of calculated confined fraction distribution as a function of pitch and radial position at the $z=0$ position (discharge #21683 6.790 s).....	85
Figure 3.5 Evaluated confined fraction profile according to effective plasma radius (#21695 7400 ms). ....	86
Figure 3.6 Estimated total confined fraction according to plasma current. Two kinds of peaking values for triton birth profile are assumed. ....	88
Figure 3.7 Triton energy loss rate changes according to finite ' $dt$ ' size.....	93
Figure 3.8 Comparison between analytic solution and numerical solution. Diffusion coefficient is set to $0.1 \text{ m}^2/\text{s}$ . In numerical solution, diffusion time step is 0.1 ms and radial step size is 1 mm. After 3 s from diffusion start with diffusion difference between analytic solution and numerical solution is 4.57%. Absolute difference is $8.99 \times 10^{-6}$ . ....	96
Figure 3.9 The time evolution of triton burnup neutron emission rate under 4 different slowing down time cases.....	98
Figure 4.1 Measured triton burnup ratio from NAS silicon sample and stilbene neutron branch data.....	99
Figure 4.2 Measured triton burnup ratio as a function of plasma current. For $I_p$ , flat-top region value is used.....	100
Figure 4.3 Measured triton burnup ratio as a function averaged value of core region $T_e$ during the discharge duration ( $T_e$ from Thomson scattering measurement at core region).....	102
Figure 4.4 Spectrogram of Mirnov coil in KSTAR discharge #21695 [81] .....	104
Figure 4.5 Measured time evolution of total neutron emission rate, triton burnup neutron emission rate and triton burnup ratio in discharge #21695.	

.....	105
Figure 4.6 Input plasma parameters at 7.4 s. From the top to bottom, $n_e$ ( $10^{19}/\text{m}^3$ ), $T_e$ (keV), $T_i$ (keV), 1 MeV triton confined fraction profile, d-d neutron rate profiles (triton birth profiles) (TRANSP result and peaking factor 6 assumed result) according to normalized effective radius. ....	107
Figure 4.7 Measured and calculated TBR in 7.4 s. Only random error from stilbene detector is considered in the measured TBR error. ....	108
Figure 4.8 Input plasma parameters at 4.45 s. From the top to bottom, $n_e$ ( $10^{19}/\text{m}^3$ ), $T_e$ (keV), $T_i$ (keV), 1 MeV triton confined fraction profiles, and d-d neutron rate profiles (triton birth profiles) according to normalized effective radius. ....	110
Figure 4.9 Measured and calculated TBR in 4.45 s (AE active phase). ....	111

# Chapter 1. Introduction

## 1.1. 3.5 MeV alpha from d-t fusion reaction

In the deuterium (D) and tritium (T) magnetic confinement fusion plasma, 3.5 MeV alpha particle and 14 MeV neutron can be produced from the deuteron (d) – triton (t) fusion reaction. The 14 MeV neutron is not confined in the plasma because as they are uncharged. The 3.5 MeV alpha particle can be confined in the plasma and act as an internal heating source for plasma sustainment. It is expected to survive inside the plasma long enough and transfer its energy to bulk plasma. When the plasma is sustained mainly by its internal heating, it is called burning plasma [1]. In burning plasma, high power amplification factor  $Q$  (defined as total fusion power divided by input heating power) can be achieved.

ITER will be the first device to study DT burning plasma and its aim is reach  $Q$  over 10 [1]. It means that over 67.7% of power loss in plasma should be sustained by its internal heating. If the energetic alpha particle is not confined sufficiently long inside the bulk plasma, i.e. loss to the vacuum vessel wall, the amount of required power for sustaining the fusion plasma from external heating source is increased. Therefore, power amplification factor  $Q$  decreases. Furthermore, if alpha particle loss is localized in certain area, it can make severe damage on the vacuum vessel wall [2]. Therefore, understanding alpha confinement in reactor-like conditions is essential for achieving burning plasma as well as machine protection [1, 3].

## 1.2. 1 MeV triton from d-d fusion reaction

In the most of present day fusion devices, the fusion plasma experiment is performed with deuterium gas due to the practical reasons such as price and easy of handling. Due to its similar kinetic properties (Table 1.1), 1 MeV tritons from d-d fusion reaction can be useful to study certain characteristics of the alpha confinement in DT plasmas [4]. Although its density is not sufficient to make collective behavior, as a test particle to study single particle motion under various plasma conditions it can be useful [5]. As shown in Fig. 1.1, in the same pitch ( $v_{\parallel}/v$ ) and same birth position, drift orbit of the triton is nearly identical with the drift orbit of the alpha. From its nominal energy, the velocity of triton is about 62% of the velocity of alpha and the Larmor radius of triton is about 93% of the Larmor radius of alpha. Its velocity distribution is also similar with that of alpha's [Table 1.1].

**Table 1.1 Kinetic properties of 1 MeV triton, 3.5 MeV alpha and 100 keV deuteron.**

	<b>Velocity distribution</b>	<b>Energy (velocity)</b>	<b>Larmor radius (at 3 T, <math>v_{\parallel}/v = 0.1</math>)</b>
t	Nearly isotropic	1 MeV ( $8.0 \times 10^6 m/s$ )	83 mm
$\alpha$	Nearly isotropic	3.5 MeV ( $1.3 \times 10^7 m/s$ )	89.6 mm
d (NB)	Anisotropic	100 keV ( $3.1 \times 10^6 m/s$ )	21.4 mm

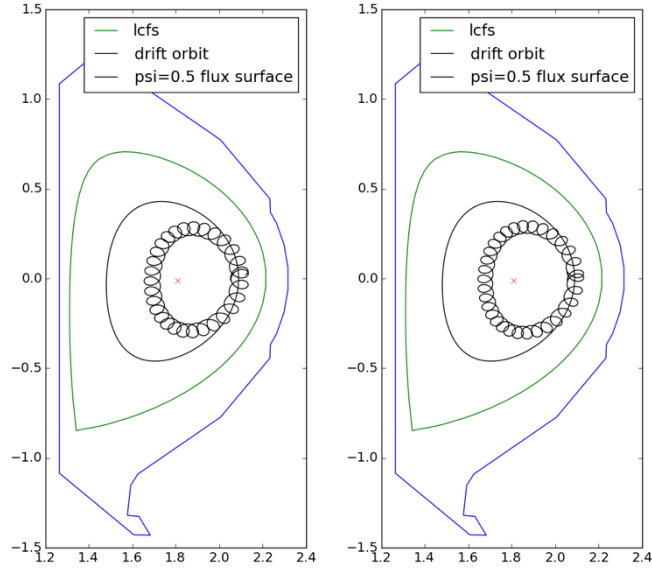


**Figure 1.1 Drift orbits of 3.5 MeV alpha (left) and 1 MeV triton (right) in the same initial birth position and pitch ( $v_{\parallel}/v$ ) condition.**

Confined 1 MeV tritons inside the bulk plasma slow down and become thermalize. While slowing down, there is possibility to make d-t fusion reaction and produce 14 MeV d-t neutron [4]. This secondary d-t fusion reaction is called triton burnup and the d-t neutron from the triton burnup is called triton burnup neutron (TBN). The ratio between triton burnup rate and triton source production rate is called triton burnup ratio. Since two branches in d-d fusion reaction have nearly the same cross-section, the burnup ratio can be obtained by measuring TBN emission rate and d-d neutron emission rate [5, 6].

Information of triton confinement can be obtained by measuring this triton burnup ratio. Triton burnup ratio in certain plasma depends both on the confinement and slowing down characteristics [7]. When triton produced, some of them makes large drift orbits which

cannot be confined inside the plasma then loss to the wall immediately. As shown in Fig. 1.2, the maximum of the d-t fusion reaction cross-section located around 170 keV of triton energy which is much lower than the birth energy of triton [8]. Thus, any events that happened during the slowing down, can change emission characteristics of TBN. Based on the Coulomb drag from background plasma, slowing down time of triton is about 1.5 times longer than that of 3.5 MeV alpha. Thus it is more sensitive to certain anomalous events during slowing down process that would be for alphas [9].

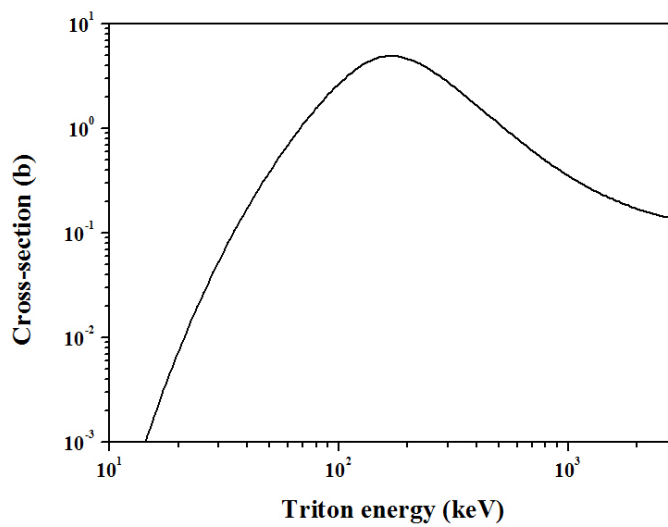


**Figure 1.2 D(t,n)α reaction cross-section according to the triton energy. Cross-section reached its maximum value at around 170 keV [8].**

Since the triton burnup ratio is combined result of many factors, in order to derive triton confinement characteristics from the measured burnup ratio, estimated burnup ratio in the target plasma is required [9]. Estimated burnup ratio can be evaluated by the calculated TBN emission based on well-established model about triton confinement and slowing down, and measured d-d neutron emission. By comparing the measured and estimated values, the amount of anomalous effect which is not considered in the models can be quantified.

This basic model without anomalous effect is called ‘classical model’ [7, 10, 11]. When calculate TBN emission based on the classical model, it can be divided into two parts. First part is prompt process. When triton produced, the drift orbit is determined by magnetic field at birth position and velocity vector of the triton. Depends on the drift orbit size its loss or confined characteristics is determined. Because this process happened nearly immediately when the triton produced, it is called prompt loss or first orbit loss. The prompt loss is largely depending on the poloidal magnetic field. In higher poloidal magnetic field, a drift orbit size squeezed and the amount of prompt loss is reduced. Thus in the higher plasma current, the more confined tritons are expected. The confined fraction of triton ( $f_c$ ) without prompt loss can be obtained from prompt loss fraction profile. From the product of the triton birth profile and  $f_c$ , confined triton density ( $n_t$ ) can be obtained.

The other part is time-dependent process. Confined tritons are slowed down due to Coulomb collisions with electrons and ions [7, 9, 10, 11]. The longer slowing down time the higher probability to have d-t fusion reaction with background deuteron. The amount of produced TBN can be expressed as the product of the  $n_t$  and expected number of triton

burnup neutron production until thermalize ( $P_{dt}$ ) [7]. In the electron drag dominant condition, triton burnup neutron emission is scaled with  $n_d T_e^{1.5}/n_e$ . Since only basic loss and collision terms are considered, the classical estimation can give maximum achievable triton burnup ratio in certain plasma condition.

Based on this methodology, triton burnup study has been carried out on several tokamaks; PLT [11,12], TFTR [9], JET [10, 13 14, 15], JT-60U [16-19], DIII-D [5], ASDEX [20], FT [21, 22] and a stellarator; LHD [23-27]. From their studies, when strong magnetohydrodynamic (MHD) instabilities are absent, measured triton burnup ratio matched within experimental error or close to theoretical expectation which is good news for alpha confinement in the DT plasma. When there are additional loss channels in particle and/or energy confinement of triton, such as, strong MHD event, toroidal field ripple, etc., classical estimation no longer adequate for triton confinement predictions. In this condition however, classical estimation still useful to quantify the amount of confinement degradation due to certain MHD activity. In addition to classical burnup theory, ad-hoc diffusive model might be useful for quantify the difference between measured and estimated values. An effective diffusion coefficient can be determined by matching estimated value with measured value [5, 16, 28].

In JT-60U, compared with normal magnetic shear, in the reversed magnetic shear case, the difference between estimated and measured burn up ratio increases [18]. It was due to its lowered poloidal magnetic field in the plasma core region for reversed shear case, triton orbit became larger and it is more easily affected by TF field ripple. The amount of decreases in triton burnup can be estimated by orbit following simulation which treat

ripple transport [18].

When there is beam-ion driven instabilities such as Alfvén eigenmodes (AEs) big difference between measured and estimated triton burnup was observed in DIII-D [5]. In order to evaluate an effect of the instability, difference between measured and estimated TBN emission was found and the estimated volume averaged effective diffusion coefficient was about  $1 \text{ m}^2/\text{s}$ .

### **1.3. Motivation**

In KSTAR [29] in order to achieve high performance plasmas, experiments with various advanced plasma operation scenarios are carried out. If triton burnup measurement and analyses tools are prepared, 1 MeV triton confinement study in these plasmas can be carried out. In many devices, including KSTAR, the confinement study of the fast ions, which produced by external heating (neutral beam injection, radio frequency heating), under various plasmas such as energetic particle instabilities are carried out [3, 30, 31]. By measuring triton burnup ratio in these conditions, different velocity domain fast ions, i.e. 1 MeV can be studied at the same time. This can be helpful to understand the fast ion confinement physics.

## 1.4. Objective and approach

The objective of this study is establishment of basis for triton burnup study in KSTAR. For triton burnup study two components are required; diagnostics for d-d neutron and TBN and calculation codes for estimated triton burnup ratio evaluation [9]. In order to measure d-d neutron emission rate, i.e. triton source rate, organic scintillator is used. The detector is absolutely calibrated by neutron activation system (NAS) with indium sample measurement results. For TBN emission rate measurement, same scintillation detector with d-d neutron but different discrimination level is used, and the measured result is absolutely calibrated by NAS silicon sample measurement results. For cross-check purpose, scintillating fiber detectors are also operated.

In order to evaluate estimated triton burnup ratio and analyze the measured value, triton burnup calculation codes based on classical theory are prepared. For prompt loss characteristics evaluation, full gyro-orbit following code Lorentz orbit (LORBIT) [32] is used. For slowing down and burnup calculation, time-dependent code is developed based on the previous studies in other devices [7, 33]. In KSTAR, usual plasma current level ( $\sim 0.4\text{-}0.7$  MA) is not sufficient to make prompt loss rate of 1 MeV triton negligible. In order to reliably estimate the triton burnup ratio, when evaluating confined triton density, statistically evaluated  $f_c$  based on LORBIT code and plasma equilibrium data and realistic triton source profile are employed.

In chapter 2, diagnostics specifications and operation results are described. In chapter 3, the details of analyses codes, evaluation routine and calculation results are shown. In

chapter 4, the measured triton burnup ratio from the diagnostics in chapter 2 is analyzed by using the codes in chapter 3.

## Chapter 2. Fusion neutron diagnostics

### 2.1. Neutron activation system (NAS)

#### 2.1.1. Operation principle

Neutron activation system (NAS) provides shot-integrated neutron yield by activation of neutron irradiated sample [13, 34-37]. Before the plasma discharge, a sample material whose reaction cross-section is selectively sensitive to target neutron energy range, is transferred to irradiation end via pneumatic transfer system. The sample is contained inside the transfer capsule for protection purpose. During the plasma discharge, the sample is irradiated by fusion neutrons, and after the discharge, sample capsule is retrieved to counting station. Sample activity is assayed using high purity germanium (HPGe) detector after certain amount of radiation cooling time. The radiation cooling time is determined based on the decay of competition reaction and/or dead time on the HPGe detector. From the measured activity the total amount of activated nuclei during discharge can be derived based on the constant reaction rate assumption (Eq. (2.1)).

$$N_{activated} = Rt_0 = \frac{\lambda C}{\alpha_\gamma \varepsilon e^{-\lambda t_1} (1 - e^{-\lambda \Delta t}) (1 - e^{-\lambda t_0})} t_0 \quad (2.1)$$

In Eq. (2.1),  $N_{activated}$  is the number of activated nuclide,  $\lambda$  is decay constant of the reaction,  $C$  is gamma counts,  $t_0$  is irradiation time,  $\alpha_\gamma$  is gamma abundance,  $\varepsilon$  is gamma detection efficiency of the HPGe detector at the target gamma-ray energy,  $t_1$  is radiation cooling time and  $\Delta t$  is gamma counting time [35].

In order to evaluate neutron yield during the discharge duration time, a relation between

neutron production and the number of activated target nuclei is necessary. The relation can be described as

$$N_{activated} = Y_n N_{target} \int \phi'(E) \sigma(E) dE \quad (2.2)$$

where,  $Y_n$  is neutron yield during irradiation time,  $\phi'$  is the neutron fluence per source neutron at the irradiation position,  $\sigma$  is the reaction cross-section, and  $N_{target}$  is the number of target nuclei. The  $N_{activated}$  can be determined from gamma counting (Eq. 2.1) and  $N_{target}$  can be determined from the sample mass. The integral term can be evaluated by in-situ calibration using well characterized neutron source with the support of neutron transport calculation. Due to the difference in real plasma condition and the neutron source, there is uncertainty in the evaluated integral value. The amount of uncertainty depends on the plasma condition can be evaluated by this neutronics calculation [38-40].

A physical meaning of the integral term is the number of activated nuclei (i.e. the number of reactions) per target nuclei per source neutron. This value has around  $10^{-31}$  order. Thus in the condition of  $10^{20}$  order of neutron yield, the fraction of activated nuclei is still less than  $10^{-10}$ . Therefore, the burn-up of target material is negligible. Due to this characteristics NAS can operate in very wide ranges of neutron yield. Furthermore, the nuclear reaction is not affected by electromagnetic waves and the reaction cross-section library is well-established. Thus, it can provide reliable and robust result. In terms of the installation interface, only small areas of irradiation end near the plasma is sufficient. When several sample materials with different reaction cross-section are used neutron spectrum at the irradiation position can be evaluated (multi-foil method) [41-43]. Thus NAS can be very powerful diagnostics in the future fusion device such as ITER and

DEMO, where neutron irradiation condition is severe.

### 2.1.2. Experimental setup

In KSTAR, ITER prototype NAS is installed and operated since 2011 KSTAR campaign [34]. The overall layout of KSTAR NAS is shown in Fig. 2.1 [34]. A re-entrant irradiation end is located at the F equatorial port and counting station and carousel are located D3 area of KSTAR torus hall. Via pneumatic transfer system capsule transferred to irradiation station and retrieved to counting station. During the experiment, entrance of KSTAR torus hall is exhibited due to safety reason. Thus all the NAS system is controlled remotely.

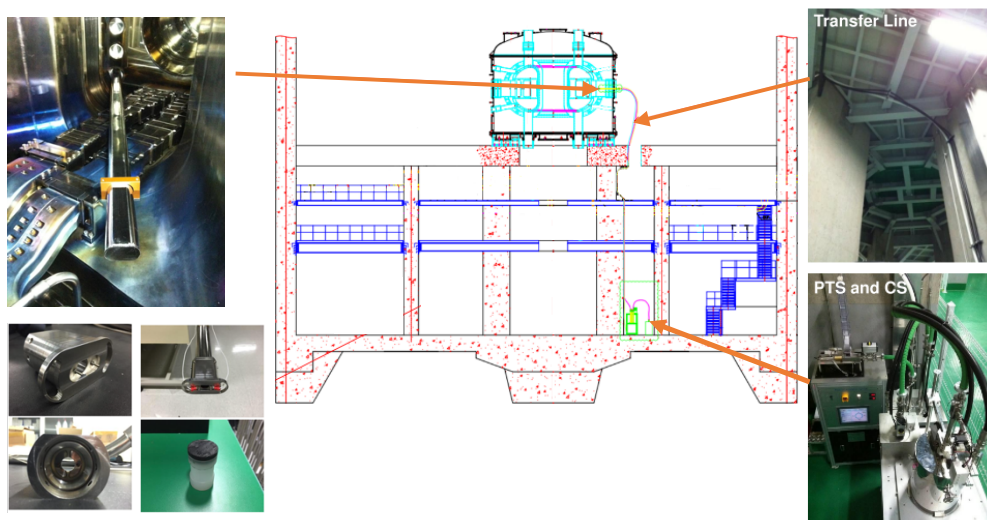


**Figure 2.1** The overall layout of KSTAR NAS [34]. Counter-clockwise from top left, irradiation end, capsule position monitoring system at the irradiation end and the capsule, pneumatic transfer system and counting station, and transfer line.

At the irradiation end, capsule position monitoring system using resistance measurement method are installed (Fig. 2.1) for confirmation of capsule arrival at the exact position. A transfer capsule is composed of polyethylene (PE) body and carbon-reinforced fiber composites (CFC) cover. The CFC cover is for the resistance measurement method at the irradiation end. The activation of PE and CFC is not problematic for sample gamma ray counting [44]. Furthermore, the amount of electromagnetic force due to conductivity on CFC is negligible for capsule transfer. The counting station consists of ORTEC-GEM25 series HPGe detector, digital signal processing unit DSPEC Pro and lead shielding. Energy and efficiency calibration of the HPGe detector has been carried out using standard gamma ray sources;  $^{133}\text{Ba}$ ,  $^{22}\text{Na}$ ,  $^{137}\text{Cs}$ ,  $^{60}\text{Co}$  and  $^{88}\text{Y}$ .

In KSTAR, d-d neutron yield has been measured by indium sample using  $^{115}\text{In}(n,n')^{115m}\text{In}$  reaction. A reaction threshold energy of this reaction is about 0.3 MeV and it has high cross-section at around 2.5 MeV neutron energy range (Fig. 2.2). After about one and half hours of cooling time from neutron irradiation, 336 keV gamma-ray radiated from  $^{115m}\text{In}$  is assayed using the HPGe detector during 5,000 s.

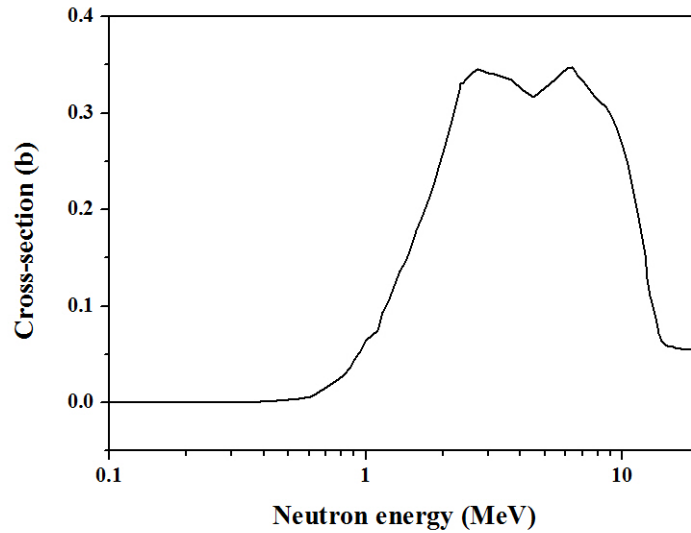


**Figure 2.2** The cross-section of  $^{115}\text{In}(n,n')^{115m}\text{In}$  reaction [45]

For the triton burnup neutron yield (TBN) measurement, appropriate sample material which has reaction that selectively sensitive to d-t neutron energy range is necessary. In addition to this, sufficient gamma-ray counting statistics has to be obtained under KSTAR operation condition. For the candidate sample materials which were used in other devices for the d-t neutron measurements, neutronics calculations are carried out for evaluation of expected activity under typical NB heated KSTAR plasma discharge neutron emission condition [46]. Based on HPGe detector efficiency and usual background level in KSTAR, minimum required gamma counting time exceeding the minimum detectable activity is obtained. Based on this calculation 4 available materials, silicon, copper, aluminum and iron are selected. Among the selected materials due to high expected activity and relatively simple measurement procedure compare with other reactions, silicon sample

$(^{28}\text{Si}(n,p)^{28}\text{Al})$  is routinely used for TBN yield measurement [46, 47]. The cross-section of the reaction  $^{28}\text{Si}(n,p)^{28}\text{Al}$  is shown in Fig. 2.3.

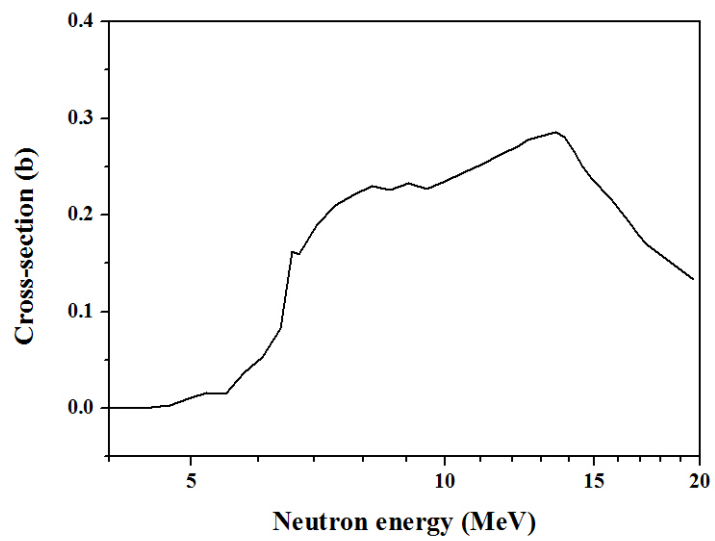


Figure 2.3 The cross-section of  $^{28}\text{Si}(n,p)^{28}\text{Al}$  reaction [45]

### **2.1.3. Neutron yield evaluation**

#### **2.1.3.1. KSTAR neutron transport model**

As described in the chapter 2.1.1, in order to evaluate neutron yield from gamma counts of activated sample, the integral term whose physical meaning is number of activated nuclei per target nuclei per source neutron has to be determined. In KSTAR, in-situ calibration of neutron diagnostics is not carried out, thus the integral term is solely derived by neutronics calculation using KSTAR MCNP neutron transport model [34]. The model is converted from computer-aided design (CAD) model of KSTAR. The KSTAR MCNP model is 90° section of the KSTAR and vacuum vessel, cryostat, superconducting coils and in-vessel components (graphite plasma facing components, passive stabilizers, neutral beam shine-through armor and in-vessel control coils) are modeled [34]. In the source part, the radial distribution is assumed to have parabolic shape with peaking factor 8 [48]. The energy distribution is assumed to be Maxwellian with mean energy of d-d neutron or d-t neutron depends on the calculation purpose. The emission velocity distribution is assumed to be isotropic.

### 2.1.3.2. d-d neutron yield

From the measured gamma-ray spectrum of activated indium sample (Fig. 2.4), the activity of  $^{115m}\text{In}$  is determined. Based on the activity and the evaluated integral term from neutronics calculation, d-d neutron yield in KSTAR is derived. The value of the integral term for  $^{115}\text{In}(n,n')^{115m}\text{In}$  reaction at the irradiation end position is  $5.56 \cdot 10^{-31}$ . Derived d-d neutron yield of plasma discharge which performed during 2018 KSTAR campaign is shown in Fig. 2.5-(a). In KSTAR, fusion neutron generation strongly depends on the neutral beam heating. Thus average neutron production rate can be derived by dividing the neutron yield by NB heating duration time. The derived average neutron production rate is shown in Fig. 2.5-(b).

Due to its radiation cooling time as well as gamma-ray counting time, only few discharges can be measured in a day. A shot-integrated neutron yield from NAS can be used for absolute calibration of a neutron flux monitor. In this case, operation reliability of the neutron flux monitor should be guaranteed. The organic scintillators which will be described in section 2.2.2 are absolutely calibrated by NAS indium sample and gives d-d neutron emission rate in every discharge.

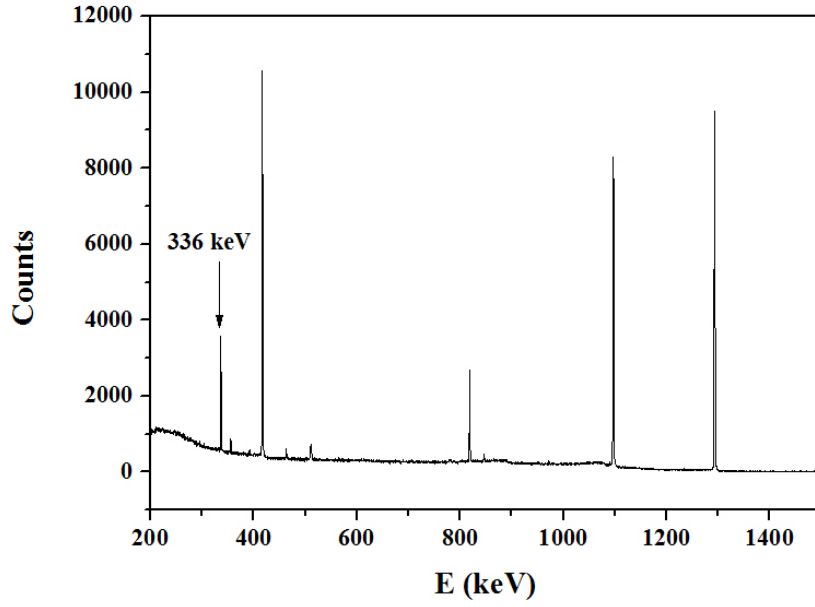
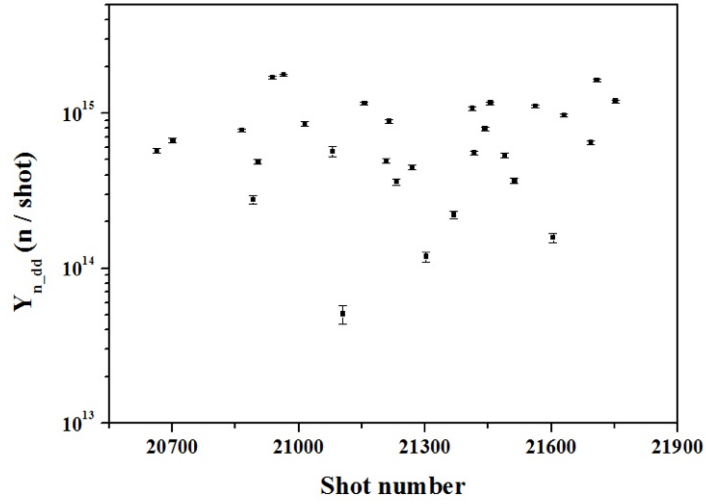
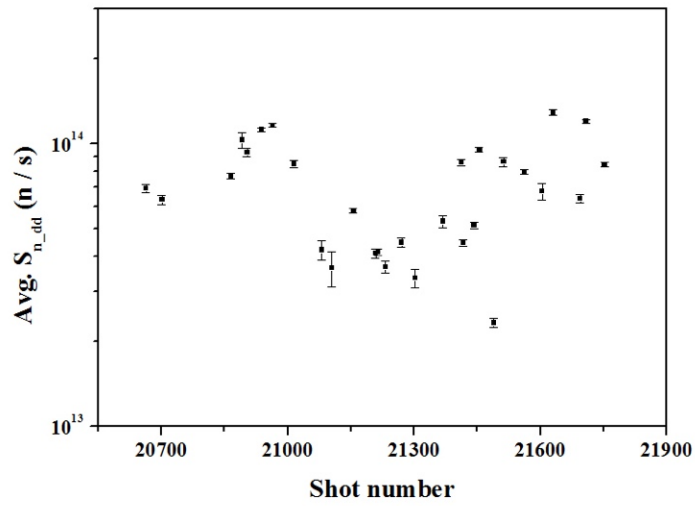


**Figure 2.4 Measured gamma-ray spectrum from activated indium sample which irradiated during the discharge #20939. The radiation cooling time was 13201 s, and gamma counting time was 5000 s.**



(a)



(b)

Figure 2.5 (a) d-d neutron yield and (b) d-d neutron average emission rate from NAS with indium sample. In the error bar, only counting error is included

### 2.1.3.3. Triton burnup neutron yield

The activity of  $^{28}\text{Si}(n,p)^{28}\text{Al}$  reaction is low compared with the activity of indium sample due to the lower triton burnup neutron yield. Since its half-life is relatively short ( $\sim 134$  s), sample gamma counting right after the irradiation is preferred. The measured gamma-ray spectrum from activated silicon sample is shown in Fig. 2.6. The total counts of 1779 keV full energy peak cannot be directly used due to the background radiation. Right after the plasma discharge, there is background gamma-ray whose full energy peak is exactly the same with the target gamma-ray full energy peak, 1779 keV [46]. This background gamma-ray is produced from the activation of surrounding aluminum structure which support the HPGe detector and lead shield. From the neutron capture reaction of aluminum ( $^{27}\text{Al}(n,\gamma)^{28}\text{Al}$ ) same daughter nuclide with  $^{28}\text{Si}(n,p)^{28}\text{Al}$  reaction can be produced (Fig. 2.7).

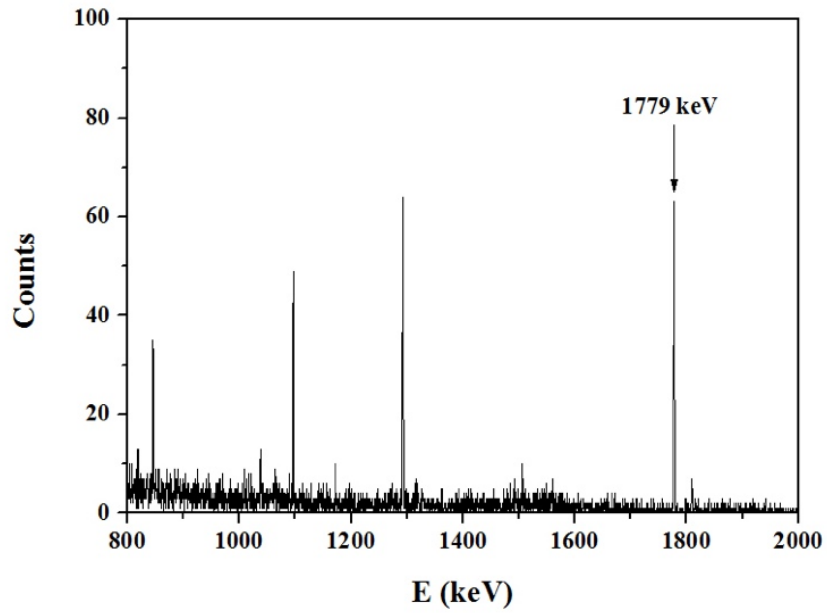


**Figure 2.6 Measured gamma-ray spectrum from activated silicon sample which irradiated during discharge #21574. Radiation cooling time and gamma-ray counting time were 56 s and 500 s respectively.**

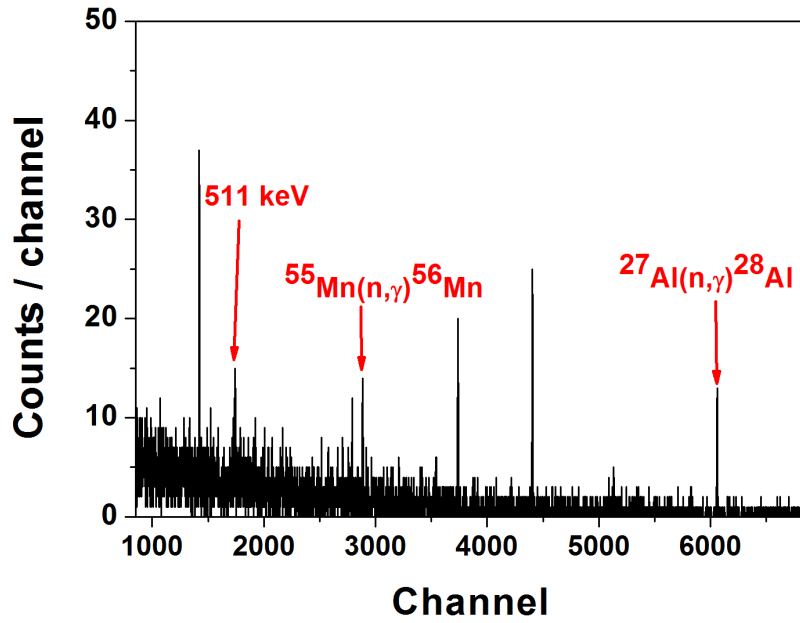


Figure 2.7 Background gamma spectrum at the KSTAR NAS counting station right after the typical neutral beam injected plasma discharge [46].

Depending on the plasma discharge scenario, the activity of the irradiated aluminum structure changes. Therefore, both the sample and background measurements within same shot interval are necessary [46]. Without direct measurement of background radiation, the expected background gamma counts can be indirectly determined, from the measured neutron yield in the target plasma discharge. In this way silicon sample gamma counting time can be maximized and better counting statistics can be achieved. For this purpose, the aluminum structure is considered as an irradiation sample, and the relationship between total neutron yield and the total number of activated target nuclide inside the aluminum structure ( $N_{activated\_Al-strt}$ ) is necessary.

The amount of recorded 1779 keV background gamma counts is expected to be proportional to  $N_{activated\_Al-strt}$  (Eq. 2.1). Since the gamma detection efficiency for aluminum structure (volume gamma source) is not identified, the exact value of  $N_{activated\_Al-strt}$  cannot be determined. The gamma detection efficiency for aluminum structure is expected to be unchanged, thus an effective value  $N_{eff}$  can be defined as the product of the detection efficiency and the  $N_{activated\_Al-strt}$ . The effective value  $N_{eff}$  is expected to be proportional to the d-d neutron yield, and the yield is proportional to shot-integrated neutron flux monitor counts ( $C_{NFM}$ ). Thus following linear relation between  $N_{eff}$  and  $C_{NFM}$  can be derived.

$$\begin{aligned}
 N_{eff} &= \varepsilon \alpha_{NFM} C_{NFM} N_{target} \int \phi'(E)\sigma(E)dE \\
 &= \beta \cdot C_{NFM}
 \end{aligned}
 \tag{2.3}$$

where,  $\alpha_{NFM}$  is the absolute calibration coefficient for NFM to change counts to the

amount of neutron production,  $\varepsilon$  is the gamma detection efficiency for aluminum structure and  $\beta$  is defined by the product among the  $\varepsilon$ ,  $\alpha_{NFM}$  and  $\int \phi'(E)\sigma(E)dE$ . From the ratio of  $N_{eff}$  and  $C_{NFM}$ ,  $\beta$  can be derived. If the  $\beta$  is not changed according to plasma discharge, we can use the  $\beta$  for evaluation of 1779 keV background gamma counts without direct measurement. As shown in Fig 2.8, the  $\beta$  value remained almost constant independent of the plasma discharge. Based on the error bar size in each measurement, weighted average and weighted standard deviation is evaluated. The average value is 1220.1 and the standard deviation is 66.9.

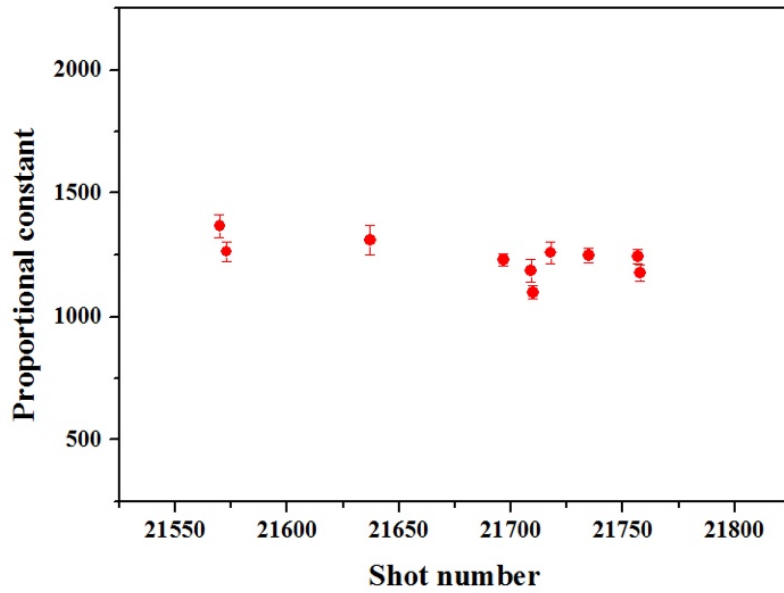
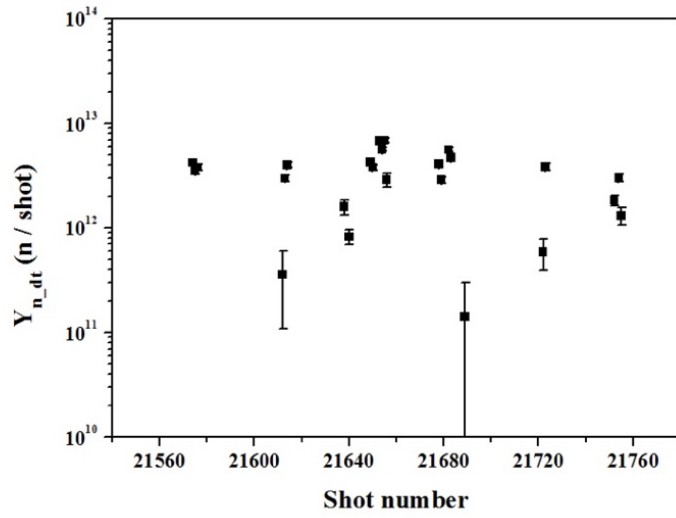
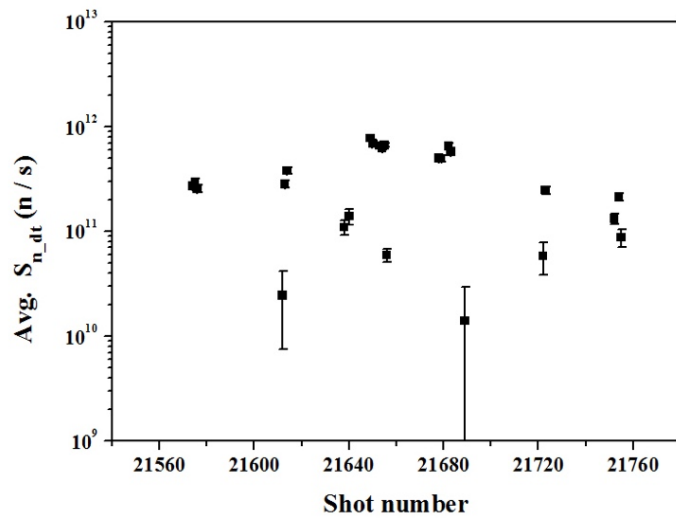


Figure 2.8 Evaluated  $\beta$  value in different plasma discharges. For neutron flux monitor data, the stilbene detector neutron branch data is used (Ch. 2.2.2). For the background gamma counts the 1779 keV gamma-peak is fitted by Gaussian function. In order to have good fitting result, background was measured when discharge (NB heated) time is over 15 s. In all the cases the error from the evaluated gamma peak area by Gaussian fitting is less than 5%. The error bar in the figure contains gamma peak fitting error and stilbene data counting error both.

From the measured gamma-ray spectrum of activated silicon sample (Fig. 2.6) and the indirect background compensation method which described in the previous page, the net counts of 1779 keV gamma-ray from silicon sample itself is determined. Based on the activity and the evaluated integral term from neutronics calculation TBN yield in KSTAR deuterium plasma is derived. The value of the integral term for  $^{28}\text{Si}(n,p)^{28}\text{Al}$  reaction at the irradiation end position is  $2.62 \cdot 10^{-31}$ . Derived TBN yield of a plasma discharge which performed during the 2018 KSTAR campaign is shown in Fig. 2.9-(a). The shot-integrated triton burnup neutron yield is about  $10^{11}$ - $10^{13}$  level. Average neutron emission rate during plasma discharge time is about  $10^{10}$ - $10^{12}$  n/s range [49].



(a)



(b)

**Figure 2.9 (a) Triton burnup neutron yield and (b) average emission rate from NAS silicon sample measurements during 2018 KSTAR campaign. The average neutron emission rate is evaluated by the yield divided by neutral beam injection duration time. In the error bar sample gamma counting error and error in background radiation compensation are included.**

## 2.2. Scintillation detectors

### 2.2.1. Overview of the system

In order to study triton confinement on various plasma conditions, not only shot-integrated measurement of d-d neutron and TBN yields but also time-resolved measurement is necessary. By using conventional neutron flux monitor such as fission chamber and  $^3\text{He}$  proportional counter which is absolutely calibrated by in-situ calibration and/or NAS measurement, d-d neutron emission rate can be evaluated. In the triton burnup neutron case due to its lower emission rate (less than 1% of d-d neutron emission rate), dedicated diagnostics that response is different only for d-t neutron energy range is required. In this chapter it is more focused on the time-resolved measurement of TBN due to its difficulties in measurement.

Previous studies on other devices, largely three kinds of diagnostics were used. First one is organic scintillator [9]. It responses neutron and gamma-ray both and by using a pulse shape discrimination technique neutron signals and gamma signals can be discriminated. It also has different response according to incident neutron energy, therefore d-d neutron and TBN emission rates can be measured at the same time. Second one is semi-conductor detector such as silicon-diode and diamond detector [5, 15, 19, 50]. This kind of detector use charged products from nuclear reaction such as  $\text{Si}(n,p)$ ,  $\text{Si}(n,\alpha)$  and  $\text{C}(n,\alpha)$  inside the detector itself for measuring TBN. The reactions have higher reaction threshold energy than d-d neutron energy, and the measured pulse signals can be discriminated from gamma-ray and d-d neutron signals by setting discrimination level in

pulse height [50]. Since it is relatively not sensitive to magnetic field, when it installed very near the plasma, it may have sufficient counts in a unit time thus high temporal resolution can be achieved. In silicon-diode case, it is rather easily damaged by neutron irradiation ( $\sim 10^{12}$  n/cm<sup>2</sup> [15]). Last one is scintillating fiber detector [16, 24, 27, 51-54]. It produces high pulse height signals especially for axially incident d-t neutron. Thus by setting threshold level in pulse height, d-t neutron signal component can be obtained. If we have a collimator, it can operate as good triton burnup camera as well. With the gain stabilizing circuit, it can provide superior temporal resolution [51].

In KSTAR, reliable d-d neutron emission rate measurement is also required as well as TBN emission rate measurement. Thus organic scintillator is selected as main diagnostics which provide d-d and triton burnup neutron emission rates at the same time [55]. Scintillating fiber detector is used as cross-check purpose at this moment.

## 2.2.2. Organic scintillators: NE213 and stilbene

### 2.2.2.1. Operation principle

The scintillation detector [56] is composed of scintillator and photo-detector. The photo-detector is optically coupled to the scintillator. When radiation interacts with a scintillator, scintillation light is produced. The photo-detector response to the scintillation light and produce usable current pulse signal. By analyzing the current pulse signal, we can identify a characteristics of incident radiation. Depending on the target radiation and measurement condition, appropriate scintillator and photo-detector can be selected.

Organic scintillator is widely used for the fast neutron detection purpose. It is hydrocarbon material and produce scintillation light when it interacts with charged particles (Fig. 2.10). After interaction between incident neutron and hydrogen inside the scintillator, recoiled proton can be produced. In gamma-ray case, recoiled electron (Compton scattered electron) is produced. Due to its different stopping power, scintillation light characteristics are different among the charged particles [56]. Proton has higher stopping power than that of electron. Thus it can deposit their energy relatively small concentrated area. In the recoiled-electron case, it deposits their energy relatively wide area. This makes difference in charge state density of scintillation molecule. As a result, slow component of scintillation light is different between recoiled-protons and recoiled-electrons [56]. By comparing total charge ( $Q_{total}$ ) and tail part charge ( $Q_{tail}$ ) of induced pulse on photo detector (Fig. 2.10), induced pulse signal can be classified whether it is produced from neutron or gamma-ray incident [56-58]. Generally, there is linearity between charged

particle energy and the amount of scintillation photons [59]. Thus we can discriminate d and TBN by comparing total charge of induced pulse.

The intensity of scintillation light is very weak and decays about 100 ns order thus, special photo-detector with fast response which can convert the scintillation light to measurable current pulse without adding a large amount of random noise is necessary. In this study for photo-detector case, fast response photo-multiplier tube (PMT) which is shielded by soft-iron magnetic shield is used. The output pulse signal from the PMT is recorded by 500 MHz sampling rate flash analog-to-digital convertor (FADC). Detailed specifications are described in following sections.

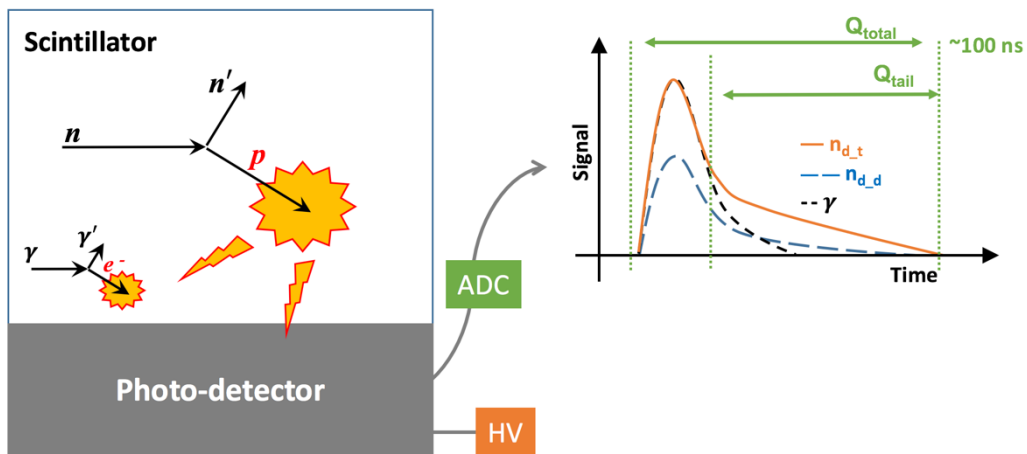


Figure 2.10 Schematic diagram for operation principle of organic scintillator.

## **2.2.2.2. Experimental setup**

### **2.2.2.2.1. Scintillator and photo-detector**

Two organic scintillators, NE213 and stilbene are used for time-resolved measurement of d-d and triton burnup neutrons. For fast neutron detection purpose, these scintillators are widely used in accelerators and magnetic confinement fusion devices [55, 60-68]. In NE213 case, the phase is liquid in room temperature. Due to this characteristics, large size detector can be manufactured relatively easily. It also can be used for neutron spectrometer by using unfolding technique [55, 60, 61]. Stilbene scintillator has more intense scintillation light than that of NE213 and also it showed better neutron/gamma discrimination performance [64]. In the present study, NE213 and stilbene scintillators are separately operated for cross-check purpose.

The size of NE213 scintillator is 50 mm in diameter and 10 mm in thickness. The scintillator is optically coupled to a PMT (Hamamatsu Photonics K.K., H7195MODB) using optical grease (Eljen, EJ-550). For stilbene scintillator case, 1-inch diameter and 1-inch thickness stilbene from Inradoptics is used. The stilbene scintillator is optically coupled to a PMT (Hamamatsu H11934-100-10) using the same optical grease.

The nominal energy of d-t neutron is about 5.5 times higher than that of d-d neutron. A scintillation light intensity is roughly proportional to recoiled proton energy, and the maximum energy of recoiled proton is proportional to the neutron energy. Thus in rough estimation, about 5.5 times intense scintillation light is expected for d-t neutron. Therefore, in order to measure d-d neutron and d-t neutron in one detector, appropriate gain level

setting is necessary due to limitation in input range in the digitizer. The analog input voltage range of the selected digitizer (described in the next section) is peak-to-peak 2 V.

The appropriate gain settings for each organic scintillation detector are determined, based on the d-t neutron irradiation test at the Intense 14 MeV Neutron Source Facility (OKTAVIAN) [69] in Osaka University, Japan. For NE213 scintillation detector, the maximum pulse height of the d-t neutron signal is  $\sim 1.7$  V with the PMT bias voltage setting of -1400 V (Fig. 2.11). For stilbene scintillation detector, the maximum pulse height of the d-t neutron signal is  $\sim 1.25$  V and  $\sim 2.7$  V with the PMT bias voltage setting of -650 V and -700 V respectively (Fig. 2.12). Based on the gain value of the stilbene scintillation detector PMT (H11934-100-10), bias voltage setting of -675 V has about 1.4 times higher gain than that of -650 V setting. Thus for bias voltage setting of -675 V, about 1.7 V of maximum pulse height is expected. The bias voltage settings for measuring d-d and d-t neutron signals by the same digitizer setting is -1400 V for NE213 scintillation detector and -675 V for stilbene scintillation detector.

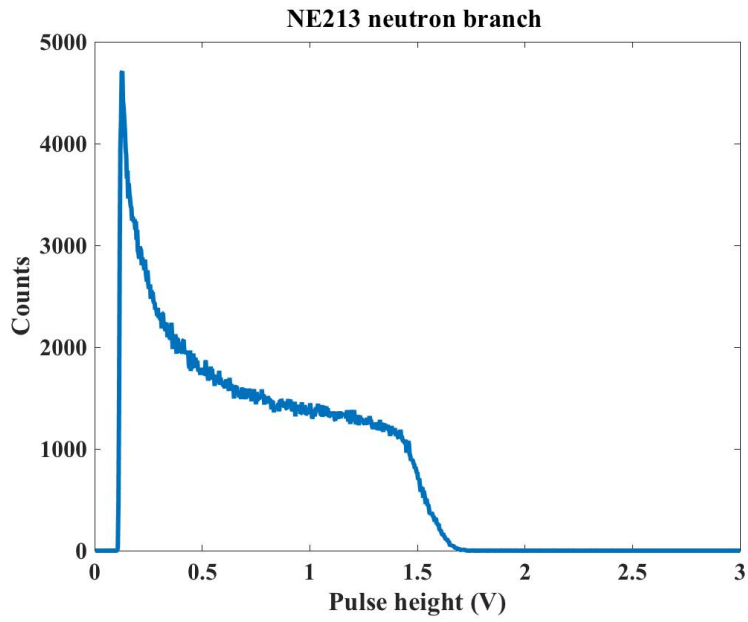


**Figure 2.11** Pulse height spectrum of neutron branch of the NE213 detector. Data obtained by APV8104- 14MW (Techno-AP). Bias voltage of PMT is -1400 V.

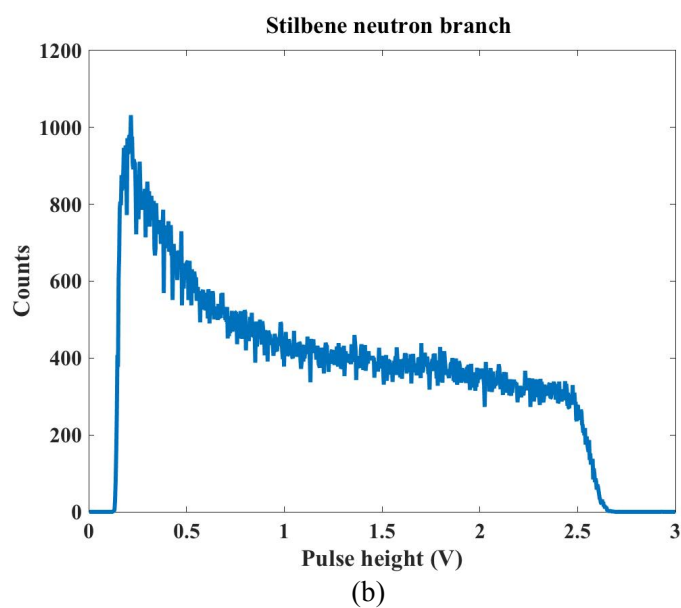
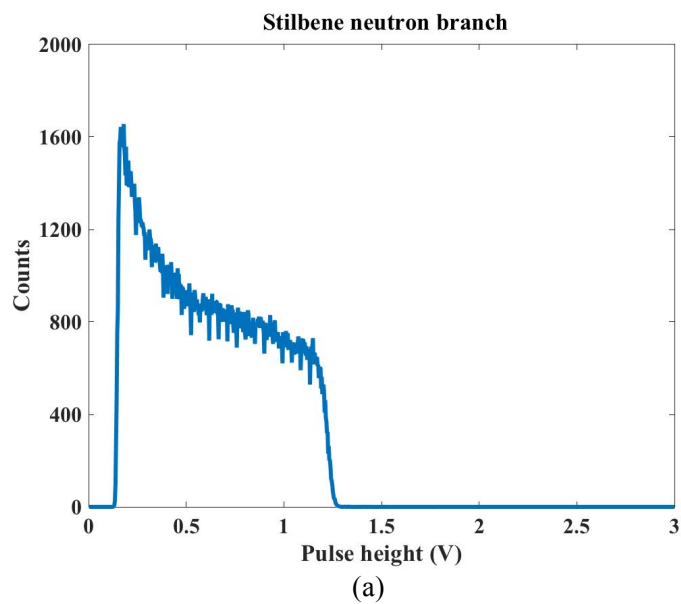


**Figure 2.12** Pulse height spectrum of neutron branch of the stilbene detector. Data obtained by APV8104- 14MW (Techno-AP). Bias voltage setting of PMT: (a) -650 V, gain $\sim 4.5 \times 10^4$ , (b) -700 V, gain $\sim 1 \times 10^5$ . For bias voltage of -675 V the gain is  $\sim 6.5 \times 10^4$ .

#### **2.2.2.2.2. Digitizer**

In order to record pulse signal on scintillation detector, flash analog-to-digital convertor (FADC) based digitizer, NKFADC500 (NOTICE [70], 4 ch., 500 MHz sampling rate, 12-bit resolution,  $2 V_{pp}$  analog input range and 8 GB onboard memory) is employed (Fig. 2.13). The minimum required sampling rate and bit-resolution for neutron and gamma-ray discrimination in an organic scintillation detector, can be determined in terms of figure of merit and misclassification probability [71].

When discharge started, a pulse whose amplitude exceed the threshold level is recorded. There are 8 options in the recording time window size; 116, 244, 500, 1012, 2036, 4084 and 8180 ns. In each digitized signal point has 2 byte of data size and the header size is 12 bytes. In the header, recording length (1 byte), module number (1 byte), channel number & trigger pattern (1 byte), waveform starting time (5 byte) and event number are recorded (4 byte).



**Figure 2.13 Photo of NKFADC500**

For organic scintillation detector operation purpose, 116 ns of recording time window size is used. An example of recorded pulse from organic scintillation detector is shown in Fig. 2.14. Basic noise level test with detector connected condition is carried out. During this test no radiation source is used. Total 10000 pulses are recorded by random triggering. For each recorded pulse, the baseline is evaluated. A variation in the baseline due to the noise is about 3 mV (Fig. 2.15).

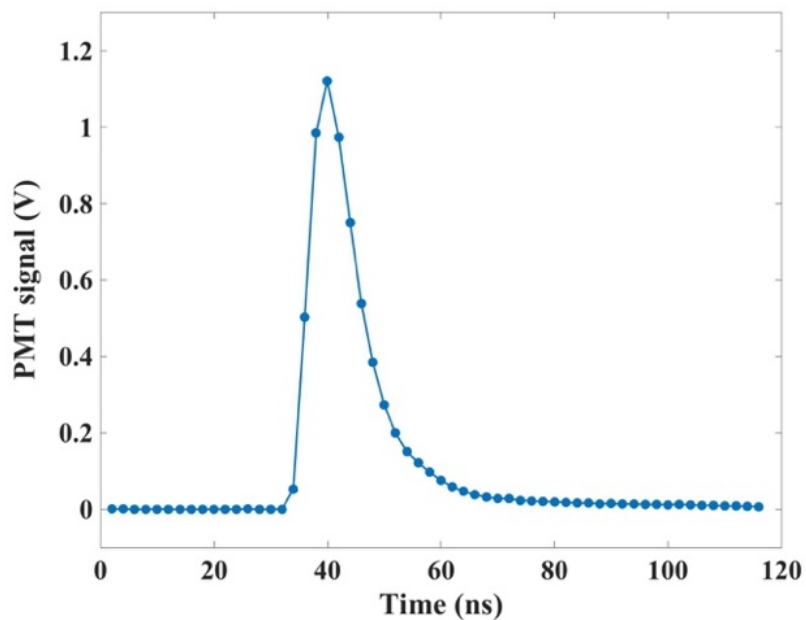


Figure 2.14 Example of the recorded waveform of stilbene scintillation detector.

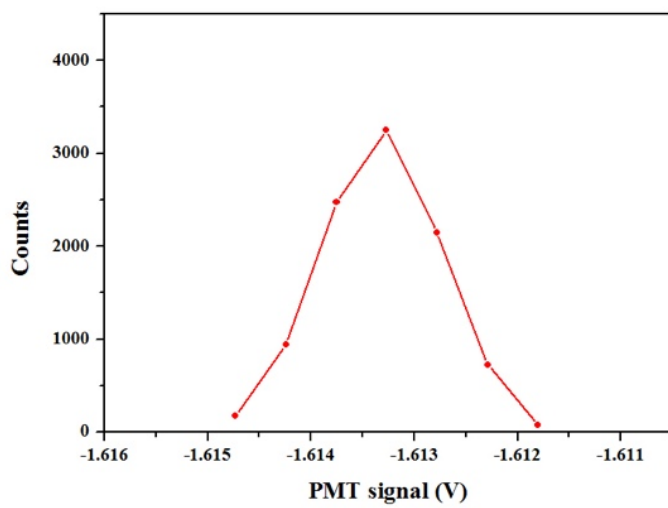


Figure 2.15 The baseline variation in recorded pulses.

During the plasma discharge, only the raw-waveform data is recorded. After the plasma discharge, off-line data analysis is carried out. For each recorded pulse, six quantities are derived, trigger time (ns), baseline, pulse height (V),  $Q_{total}$  (V·ns),  $Q_{tail}$  (V·ns) and PSD ( $Q_{tail}/Q_{total}$ ). For the trigger time, the waveform starting time which is recorded in the header is used. The baseline is evaluated by averaging first three data points in the recorded pulse. There is 8 ns of uncertainty in the internal clock of the digitizer for event starting time record. This amount of variation in trigger timing effectively modify the pulse integration window length. In this reason, based on the baseline and pre-set trigger level, trigger point is redefined for each pulse. The trigger level is 50 ADC channels in both organic scintillation detectors. The charge integration window range for the total charge ( $Q_{total}$ ) is from the 3 data point before the redefined trigger point to the 56<sup>th</sup> data point. The charge integration window range for the tail part charge ( $Q_{tail}$ ) is from the 12 data point after the redefined triggered point to the 56<sup>th</sup> data point.

### **2.2.2.2.3. Radiation shielding and installation in KSTAR**

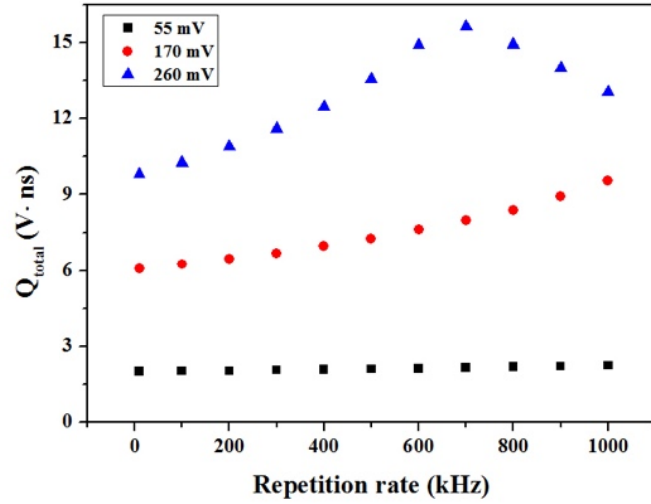
In order to obtain incident radiation information reliably using organic scintillation detectors, the distortion on the recorded pulse should be minimized. In the high counting rate condition, recorded pulse information can be distorted by pulse pile-up and/or PMT gain shift [72]. When more than one pulse occurs simultaneously or closely located in time it is called pulse pile-up [73]. When the pulse pile-up happened, without pile-up detection and reconstruction algorithm [73], it is recognized and processed as one pulse, so it leads to distortion of the pulse shape and decrease in counting efficiency as well. When gain shift occurs in a PMT, an energy information on the recorded pulse can be changed [74]. For the above reasons, in the detector side, the maximum achievable counting rate is limited by the amount of distortion in the recorded pulses due to the pulse pile-up and gain shift. The detector should be operated under this level in order to reliably discriminate neutron and gamma signals and also d-d neutron and TBN signals.

If the expected counting rate of the detector exceed the maximum achievable counting rate, additional radiation shielding is required in order to reduce the incident radiation flux. Installation position and required radiation shielding size of organic scintillators are determined based on the estimated pulse pile-up rate and gain shift according to the counting rate, and test operation result in KSTAR NB heated plasma discharge condition.

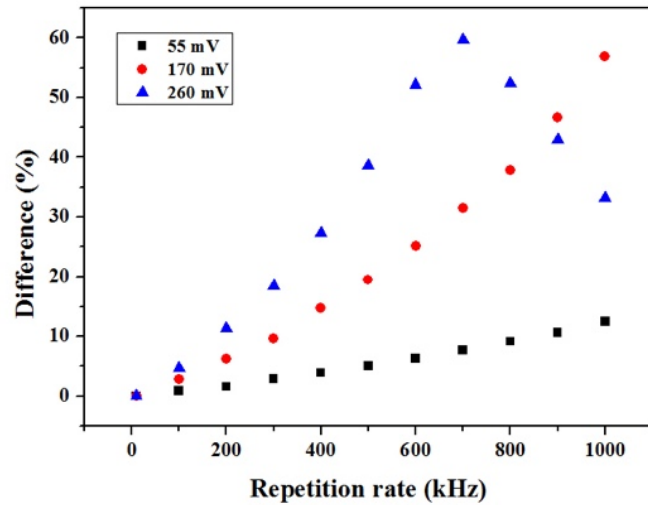
In the pulse pile-up case, expected pile-up rate can be roughly estimated based on pulse width and counting rate. When the counting rate is 1 MHz and the pulse width is 100 ns, the duty cycle can be thought to be as 10%. Since each event is independent and randomly occurred, from the rough estimation, the pile-up probability between successive two

events, i.e. pulse pile-up rate is 1%.

For the gain shift case, the effect depends on the photo-detector specification and characteristics of induced pulses such as pulse height and pulse width. In order to check the amount of gain shift according to the counting rate under certain induced pulse characteristics, a PMT test by using nanosecond pulsed laser (Thorlabs, NPL45B) is carried out. The laser and a PMT are installed inside the dark room. A repetition rate of the pulsed laser can be controlled by external trigger, and it is scanned from 10 kHz to 1 MHz. A pulse width of the pulsed laser is set to be 50 ns which is similar range with the pulse from organic scintillators. The rise and the falling time are less than 10 ns. The laser light is diffused by optical diffuser and the intensity is adjusted by using neutral density (ND) filters. In the output power of the laser, there is certain amount of variation. Thus when evaluate total charge of the induced pulse on PMT, it is averaged over 512 pulses. The test result of the PMT for the stilbene scintillator (H11934-100-10) is shown in Fig. 2.16.



(a)



(b)

Figure 2.16 (a) A changes of  $Q_{total}$  of induced pulse on H11934-100-10 PMT according to the repetition rate and pulse height. (b) The same data but the amount of variation in  $Q_{total}$  according to the repetition rate is expressed by the difference from the  $Q_{total}$  at the 10 kHz repetition rate condition.

As shown in Fig 2.16, the amount of gain shift is affected by the induced pulse characteristics as well as repetition rate. Thus in order to identify the amount of gain shift under KSTAR torus hall condition, a realistic information of induced pulse is required. In KSTAR torus hall, intense d-d neutron and prompt gamma ray fluxes are expected. The induced pulse characteristics are the combined result between d-d neutron and gamma-ray signals. In the absence of the realistic information, the expected gain shift behavior under KSTAR condition can be roughly estimated based on the d-t neutron irradiation test result. In the d-t neutron irradiation test (Fig. 2.11, 2.12) the maximum pulse height of the d-t neutron is about 1.7 V in each organic scintillation detectors. With the assumption of linearity between  $Q_{total}$  and pulse height, based on the difference in the nominal energy, about 5.5 times smaller maximum pulse height is expected for d-d neutron (~0.3 V). If we assume the pulse height distribution is flat, which overestimates the average pulse height than the real condition, the average pulse of 150 mV is expected from the neutron induced signals. Since the pulse width of the pulsed laser is set to be similar with the organic scintillator, only from the neutron induced signal, similar gain shift trend with that of 170 mV test condition might be expected.

In addition to the neutron induced signal, gamma induced signal also has to be considered when estimating the PMT gain shift. The gamma signal in the d-d neutron irradiation condition, the maximum pulse height is higher than that of d-d neutron [63]. If the amount of neutron and gamma-ray signals are in the similar level, the consideration of gamma induced signal causes the increase of average pulse height. Thus it will enhance the amount of gain shift. Based on the above consideration, under the KSTAR condition,

similar gain shift trend with 260 mV test condition might be expected. Thus in order to restrict the amount of gain shift according to the counting rate within few tens of percent, organic scintillation detector operation under few hundreds of thousands counts per second (CPS) would be desirable. The amount of gain shift in the real KSTAR operation case is described in Chapter 2.2.2.3.

The gain shift can be minimized by using additional circuit and/or correction system [51]. Also for pulse pile-up, the piled-up pulse can be identified and reconstructed by using sophisticated off-line data analysis routine [73]. In the present study, these kinds of active methods are not utilized.

An operation test in order to estimate counting rate level in real operation condition is carried in front of KSTAR D-port area. The distance is about 6 m from the center axis of the KSTAR. In the  $1 \cdot 10^{14}$  n/s d-d neutron emission rate condition, the estimated neutron flux by the MCNP [75] calculation at this position is about  $4.4 \cdot 10^6$  /cm<sup>2</sup>/s, and about one order of magnitude lower flux level for gamma flux. Without radiation shielding the maximum counting rate of NE213 scintillation detector with bias voltage of -1400 V exceeds several tens of MCPS in the typical H-mode discharge. In this condition, neutron and gamma-ray discrimination cannot be carried out due to severe pulse pile-up rate. In current KSTAR MCNP model, many structures which located outside the cryostat are not realized yet, in this reason, scattered neutron and prompt gamma-ray flux might be underestimated.

The installation position and radiation shielding specification is determined so that the detector counting rate does not exceed few hundreds of kCPS at the highest neutron

emission rate discharge. The NE213 detector position is changed from R=6 m position to R~12 m position (in the front side of D-port). In the vertical position, the detector located near the horizontal plane. The front side of the detector is shielded by (from the inside) 100 mm of lead and 200 mm of boron-polyethylene, in order to protect from the gamma-ray, and neutron radiation respectively [55, 63]. Also in the front side, there is a 20 mm diameter collimator hole (Fig. 2.17). The detector is viewing the KSTAR plasma perpendicularly in the equatorial plane. In the side, bottom and upper part of the detector are shielded by about 50 mm lead and 200 mm of boron-polyethylene. The signal from anode of the PMT (Hamamatsu Photonics K.K., H7195MODB) is directly fed into the digitizer via 16 m long Canare L-5D2W double shielded 50  $\Omega$  coaxial cable.

With this position and radiation shielding, the maximum counting rate in 5 MW of NB heated discharge (#19370) is less than 200 kCPS. Up to this counting rate condition, the effect of pulse pile-up on the neutron and gamma ray discrimination is not observed. The ratio of neutron counts to gamma counts is about 0.4. The amount of the gain shift is evaluated based on the maximum  $Q_{total}$  position of d-d neutron and it is less than 10% [63].

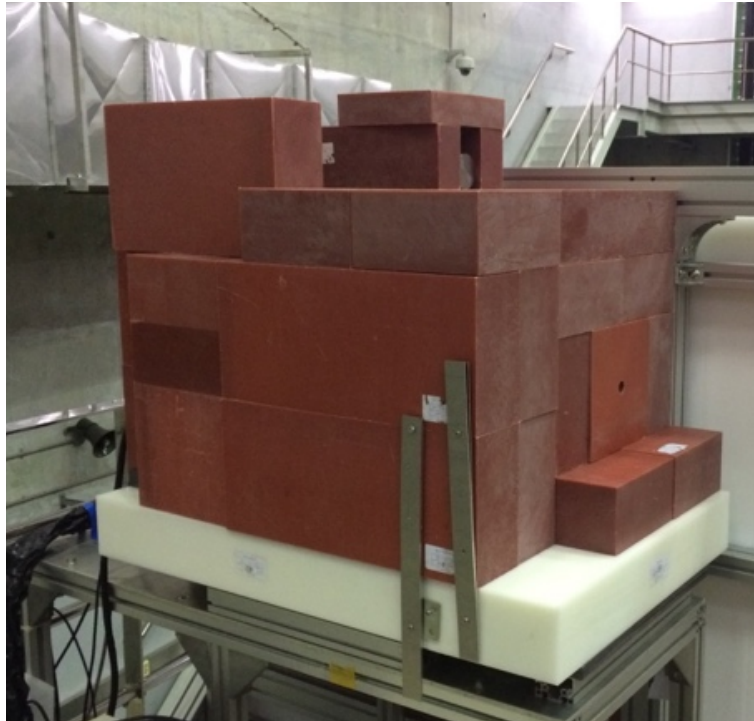
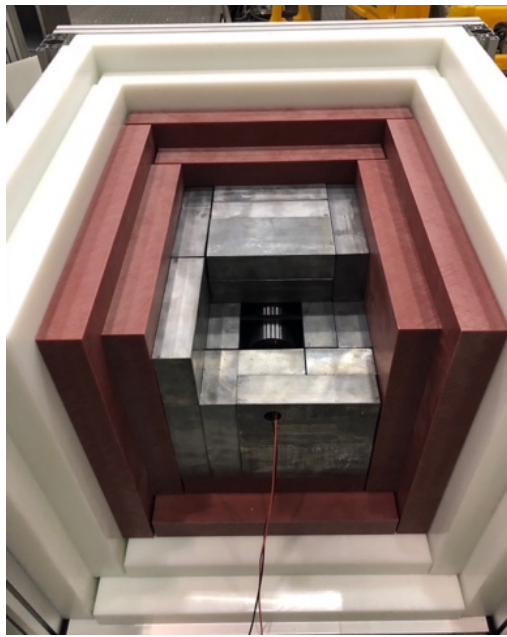


**Figure 2.17 Radiation shielding of NE213 scintillation detector. From the inside, the detector is surrounded by 10 mm thickness soft iron, lead blocks and boron-polyethylene blocks for magnetic field, gamma-ray and neutron shielding respectively.**

The stilbene scintillation detector is installed right beside the NE213 scintillation detector (Fig. 2.18). Based on the NE213 detector test result, the radiation shielding for stilbene scintillation detector is prepared. From the inside, the detector is surrounded by 10 mm thick soft iron, 100 mm thick lead, 100 mm thick boron-polyethylene and 100 mm thick high density polyethylene (HDPE). The radial position is similar with that of NE213 ( $R \sim 12$  m) and the vertical position is about 0.5 m lower than the horizontal plane. There is 20 mm diameter hole in the front side of the shielding for collimator purpose. The stilbene scintillation detector is viewing the KSTAR plasma perpendicularly. The anode output of the PMT (H11934-100-10) is directly fed into the digitizer via 16 m long Canare L-5D2W double shielded 50  $\Omega$  coaxial cable.



(a)



(b)

**Figure 2.18 (a) Radiation shielding of stilbene scintillation detector and (b) inside of the stilbene detector radiation shielding.**

The digitizer is installed inside the diagnostic cubicle located under the deck in the D-port area (Fig. 2.19). The plasma facing side is shielded by 100 mm thick HDPE blocks to prevent the deterioration of the digitizer performance during the experimental campaign. The overall positions for NE213 detector, stilbene detector and diagnostic cubicle are shown in Fig. 2.20.



**Figure 2.19 Diagnostic cubicle**

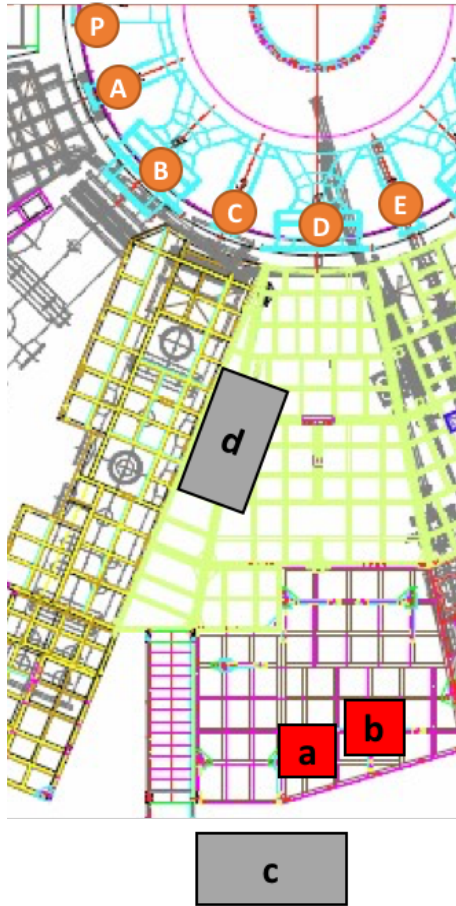


**Figure 2.20 Installation position of each compent, a: NE213 detector, b: stilbene detector, c: diagnostic cubicle and d: NE213 test position**

### 2.2.2.3. Operation stability and discrimination level setting

With the above settings two organic scintillators are operated in 2018 KSTAR campaign. From the recorded organic scintillation detector data during the plasma discharge, two-dimensional histogram of  $Q_{total}$  against PSD value ( $Q_{tail}/Q_{total}$ ) can be made as shown in Fig. 2.21. The x-axis  $Q_{total}$  represents the amount of scintillation light produced, and the y-axis PSD represents the pulse shape characteristics. As described in the organic scintillator operation principle section (Chapter 2.2.2.1), by using difference in the pulse shape, neutron and gamma-ray can be discriminated. The gamma-ray branch is located at the lower PSD value (PSD < ~0.14) and the neutron branch is located at the higher PSD value (PSD > ~0.14). By setting appropriate discrimination level on PSD, neutron and gamma ray signal can be discriminated. In the neutron branch region, above the  $Q_{total}$  of about 1 V·s, there TBN signals. Due to its lower emission rate than d-d neutron, the recorded counts are much less than that of the d-d neutron. By setting appropriate discrimination level on  $Q_{total}$ , d-d neutron and TBN signals can be discriminated.

Based on these  $n/\gamma$  and  $n_{dd}/n_{dt}$  discrimination levels, d-d neutron and TBN emission rates can be evaluated by one detector. In this section, these discrimination levels are determined and discrimination performance are evaluated according to counting rate.

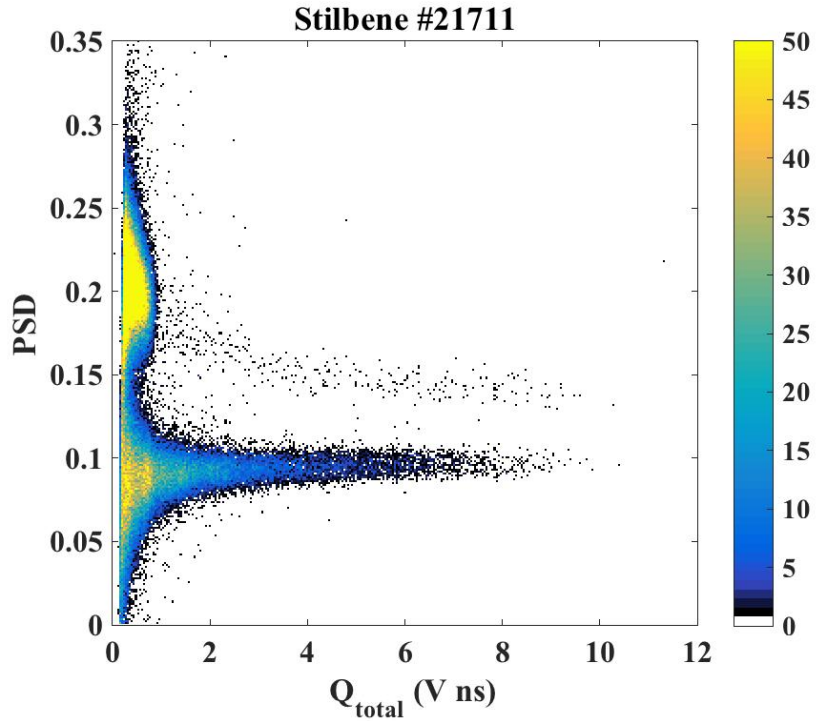


**Figure 2.21** Two-dimensional histogram of PSD value as function of  $Q_{total}$ . In this plot, all the data points recorded during the plasma discharge #21711 by stilbene detector are used. If some specific time information is required, this kind of 2D histogram also can be made by using data points which contained in that time-interval. Since neutron signal has larger tail charge to total charge ratio, i.e. larger PSD value, the neutron branch is located in the higher PSD value ( $> 0.14$ ), and the gamma-ray branch is located in the lower PSD value ( $< 0.14$ ).

In the high counting rate condition, due to the increased pulse pile-up probability, n/ $\gamma$  discrimination performance can be degraded. Before checking the performance degradation, the amount of pulse pile-up rate according to counting rate is estimated. By comparing the counting rate of the organic scintillation detector with un-saturated conventional neutron flux monitor, it can be verified that whether there is severe pulse pile-up happened or not. If there is severe pulse pile-up in the detector, piled-up pulse is recorded as one pulse, therefore the counting efficiency decreased and saturated behavior will be shown [62].

As shown in Fig. 2.22, the NE213 data showed good linearity with fission chamber data up to about 200 kCPS of counting rate. Therefore, up to this counting rate condition, there is no severe pulse pile-up which can decrease the counting efficiency. There is also good linearity between stilbene detector and NE213 (Fig. 2.23). For the same target discharge, stilbene detector showed lower counting rate than that of NE213. This might be due to the combined effect between different detection efficiency and different radiation shielding configuration.

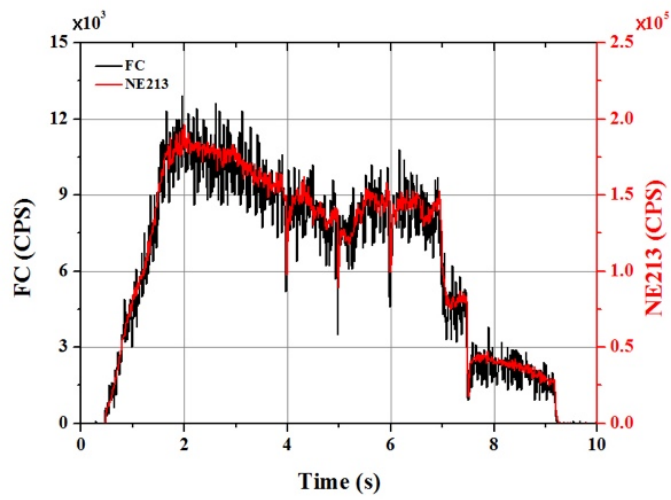
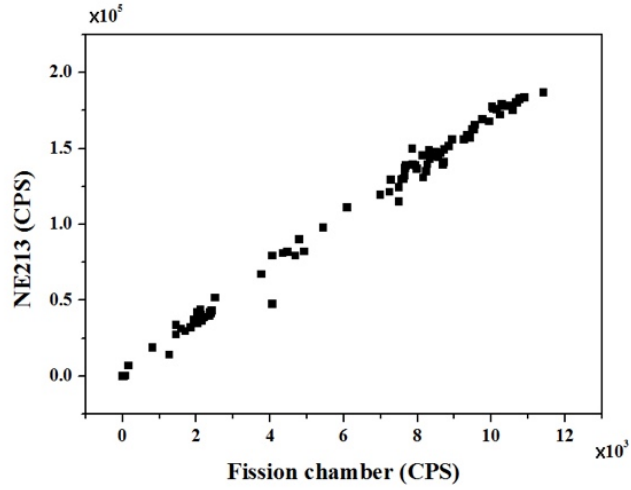


Figure 2.22 Linearity check between NE213 scintillation detector and fission chamber [62]

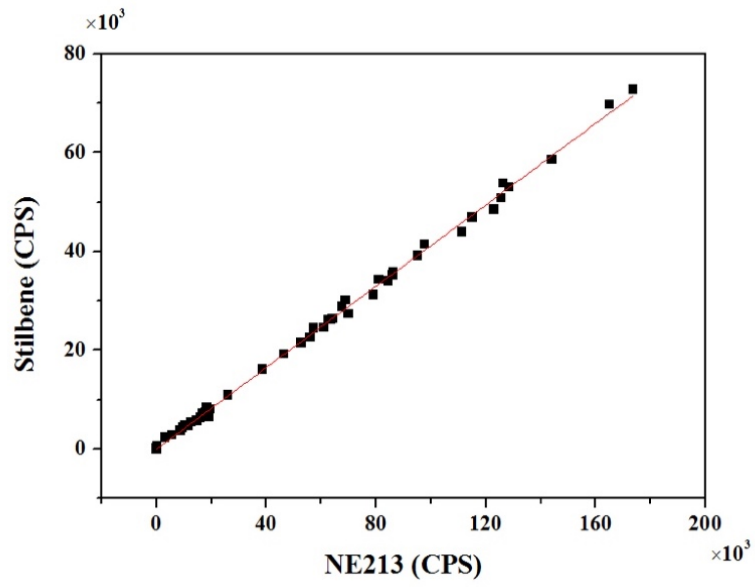
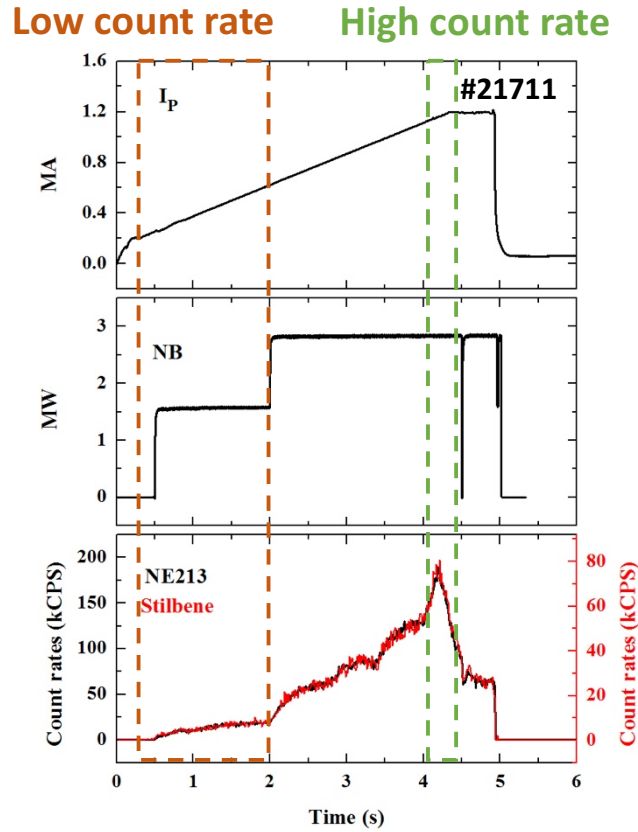


Figure 2.23 Linearity check between stilben scintillation detector and NE213

The effect of counting rate on the  $n/\gamma$  discrimination performance is evaluated. In order to check the high counting rate effect, two regions are selected one is low counting rate region and the other is high counting rate region. Target plasma is KSTAR plasma discharge #21711. This discharge records the maximum counting rate in 2018 KSTAR campaign. In the low counting rate region (0 - 2 s), the average counting rate for NE213 detector is 10 kCPS and for stilbene detector is 4.3 kCPS. In the high counting rate region (4.14 - 4.26 s), the average counting rate for NE213 is 171 kCPS and for stilbene detector is 72.2 kCPS. The discharge information is shown in Fig. 2.24.



**Figure 2.24 Plasma discharge #21711. Two different counting rate regions are shown. The time range in each region is set so that the number of counts in each region is similar.**

In these two regions, pulse shape discrimination performance is compared. In each region in specific  $Q_{total}$  range, 2-dimensional histogram of PSD according to  $Q_{total}$  can be changed to 1-dimensional histogram of PSD (Fig. 2.25). In the 1-dimensional histogram, neutron and gamma-ray branches can be fitted by Gaussian function. Based on the fitted lines, neutron and gamma ray discrimination performance can be evaluated in terms of figure of merit (FOM). It is defined by separation between neutron and gamma-ray peaks divided by summation of full width half maximum (HWHM) of two peaks [76]. Therefore,

in the higher FOM, clear separation of two peaks are expected. A discrimination level between neutron and gamma-ray can be determined as a valley position between two Gaussian fitted curves. In addition to FOM, by using overlapped region between two Gaussian fitted curves, misclassification probability [71] can be evaluated (Fig. 2.26). For example, in the neutron branch, small amount of portion can be affected from gamma-ray branch (denoted by ‘B’ in the Fig. 2.26). The misclassification probability can be evaluated by the area ‘B’ divided by the area ‘A’.

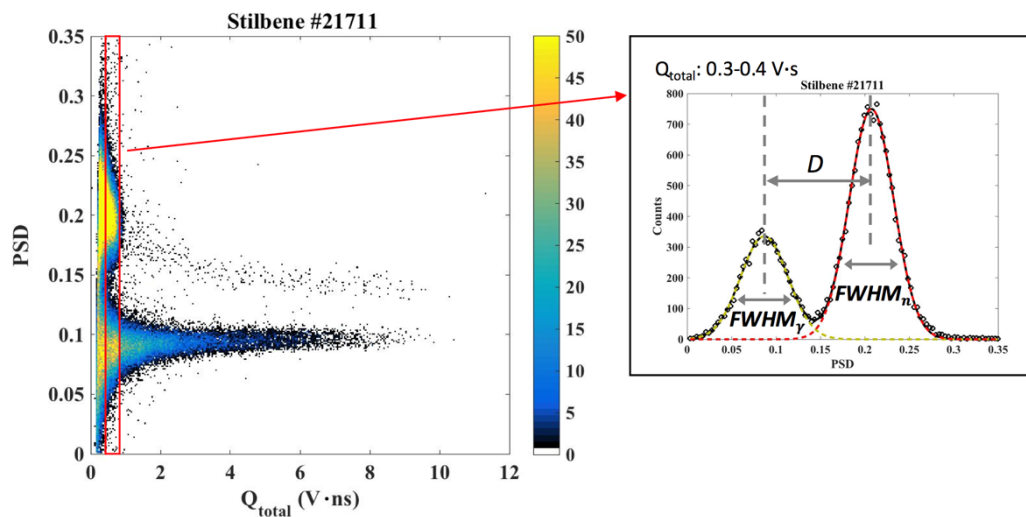


Figure 2.25 One-dimensional histogram of PSD in specific  $Q_{total}$  range. Figure of merit (FOM) =  $D / (FWHM_{\gamma} + FWHM_n)$ .

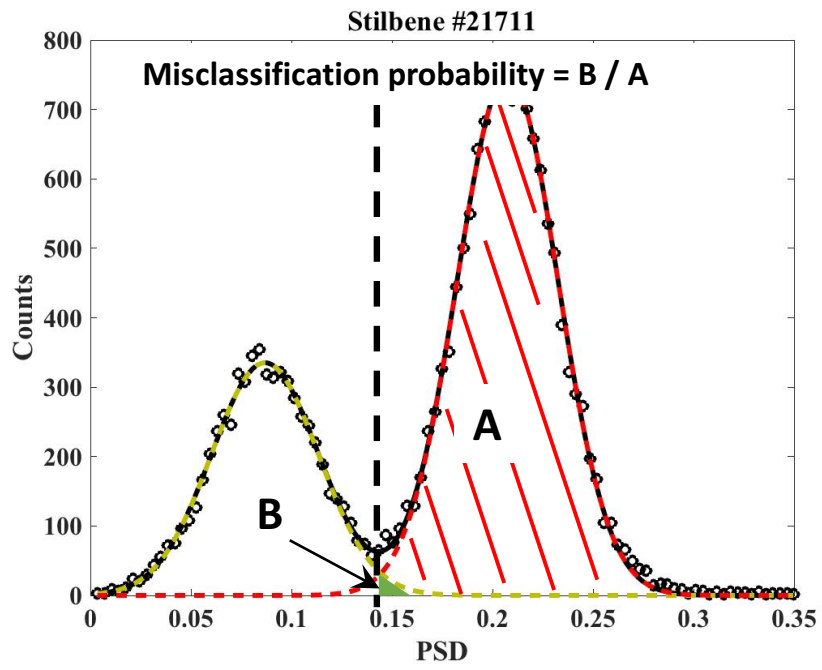


Figure 2.26 Misclassification probability in the neutron branch.

A changes of the FOM and the misclassification probability according to the counting rate region is shown in Fig. 2.27 (NE213 scintillator) and Fig. 2.28 (stilbene detector). In the FOM case, a reference value of 1.27 is also plotted [76]. This reference value is derived by two Gaussian distributions separated by the amount of three times in summation of standard deviations of each distribution, i.e.  $3(\sigma_{neutron} + \sigma_{gamma})$ .

In the both detectors, over about 0.5-0.6  $Q_{total}$  range, it started to exceed the reference value and the misclassification probability is less than 0.1 % in each detector and each counting rate region. In the stilbene detector case, the maximum degradation in FOM according to counting rate is about 10%, but it is still higher than the reference value. Thus neutron and gamma ray signals are well discriminated over 0.5-0.6  $Q_{total}$  range in terms of the FOM value and misclassification probability.

## NE213

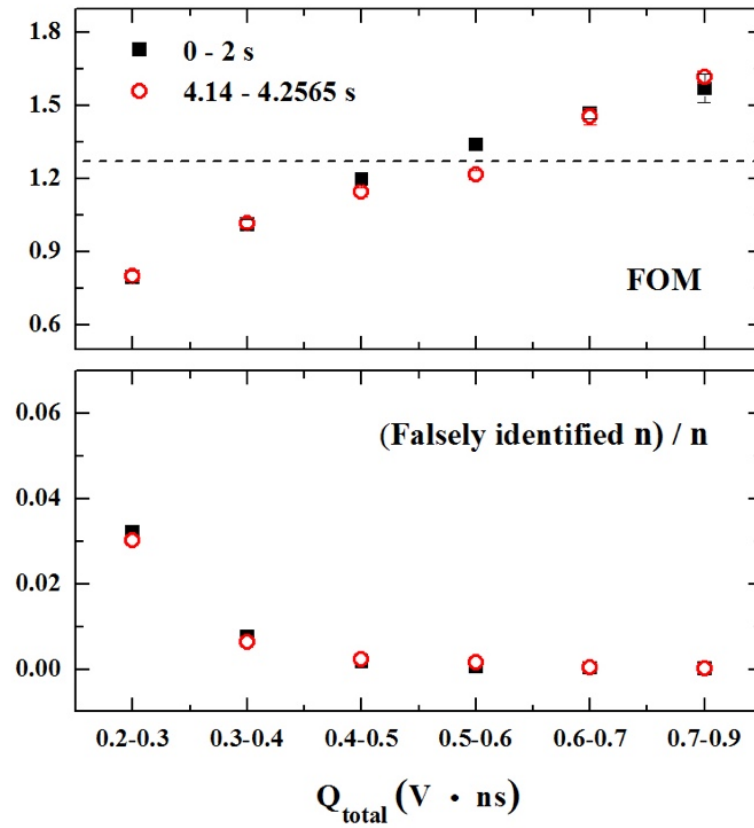


Figure 2.27 FOM and misclassification probability of NE213 detector in each counting rate region.

## Stilbene

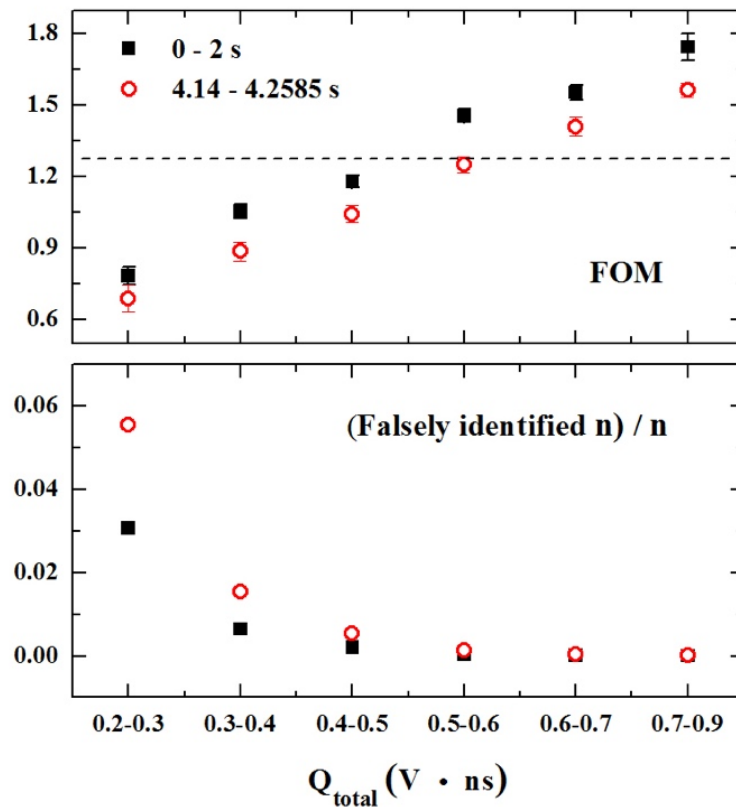
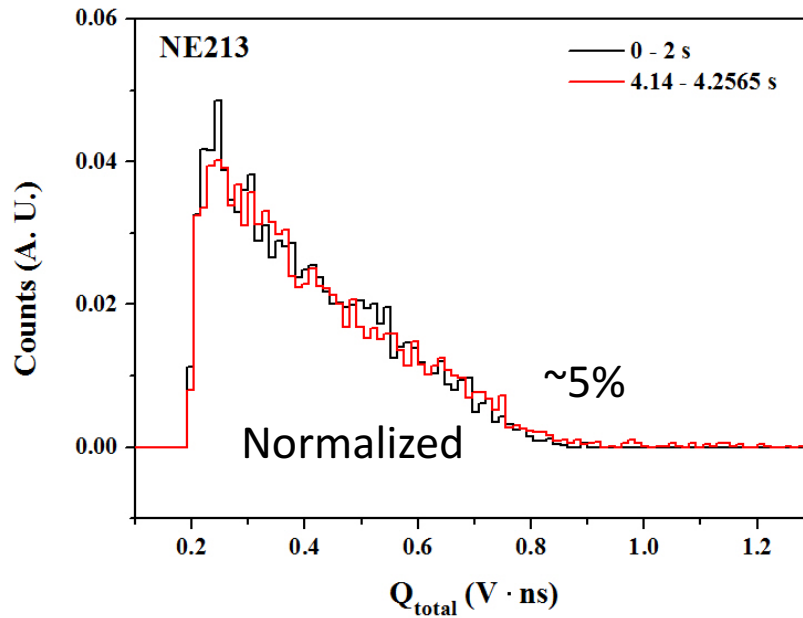


Figure 2.28 FOM and misclassification probability of stilbene detector in each counting rate region.

In KSTAR, the neutron production is dominated by neutral beam induced reaction; beam-target and beam-beam reactions. In the discharge #21711, acceleration voltage of neutral beam injection doesn't change. Therefore, a maximum value of  $Q_{total}$  of d-d neutron can be used as reference value for monitoring a changes in the PMT gain. The neutron branch energy histogram of NE213 detector and stilbene detector in each counting rate region is shown in Fig. 2.29 and Fig. 2.30 respectively. In the high counting rate condition, there is increases in maximum  $Q_{total}$  value of the d-d neutron. About 5% increases in the NE213 detector case and about 2.7% increases in the stilbene detector case. The discrimination level between d-d neutron and TBN is determined by considering this variation.



**Figure 2.29** Energy histograms of NE213 detector neutron branch signal in each counting rate region. The total counts in each counting rate region is normalized to 1. The maximum  $Q_{total}$  of d-d neutron can be derived from the intercept point between the extended energy histogram slope and the horizontal axis. Changes in maximum  $Q_{total}$  of d-d neutron according to pulse counting rate is about 5%.

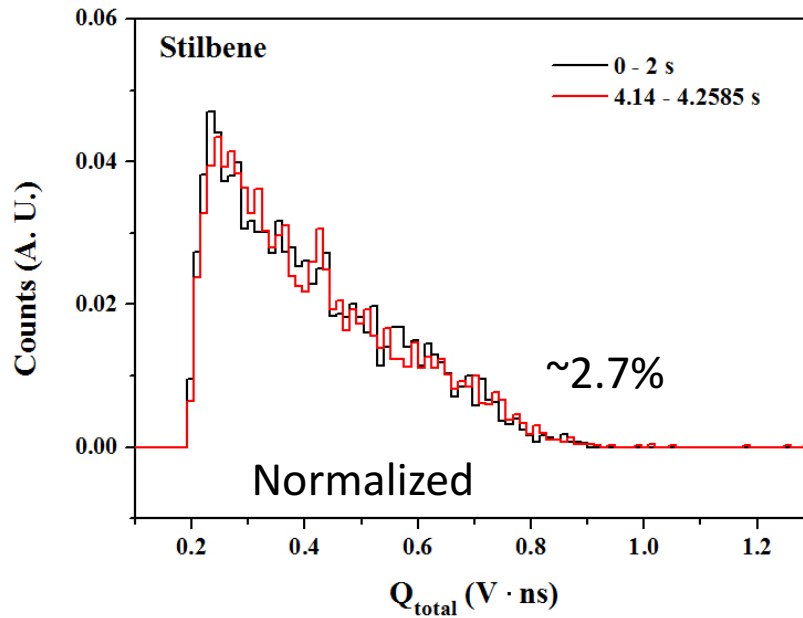


Figure 2.30 Energy histograms of stilbene detector neutron branch signal in each counting rate region. The total counts in each counting rate region is normalized to 1. The maximum  $Q_{total}$  of d-d neutron can be derived from the intercept point between the extended energy histogram slope and the horizontal axis. Changes in maximum  $Q_{total}$  of d-d neutron according to pulse counting rate is about 2.7%.

Discrimination levels for d-d and triton burnup neutrons are determined based on previous analyses. The discrimination levels are shown in Table 2.1. Although the maximum  $Q_{total}$  of d-d neutron is similar in NE213 detector and stilbene detector, due to some spurious pulses might be caused in the PMT, discrimination level in  $Q_{total}$  for triton burnup neutron in NE213 detector is set in the higher level than that of stilbene detector. Based on the above discrimination ranges, time dependent d-d neutron and triton burnup neutron counting rates are shown in Fig. 2.31.

**Table 2.1 Discrimination ranges for d-d neutron and triton burnup neutron in the organic scintillation detectors.**

	<b>d-d neutron</b>	<b>Triton burnup neutron</b>
NE213	PSD: 0.118-0.3 $Q_{total}$ : 0.5-12	PSD: 0.103-0.15 $Q_{total}$ : 3.5-12
Stilbene	PSD: 0.143-0.3 $Q_{total}$ : 0.5-12	PSD: 0.129-0.2 $Q_{total}$ : 1.2 -12

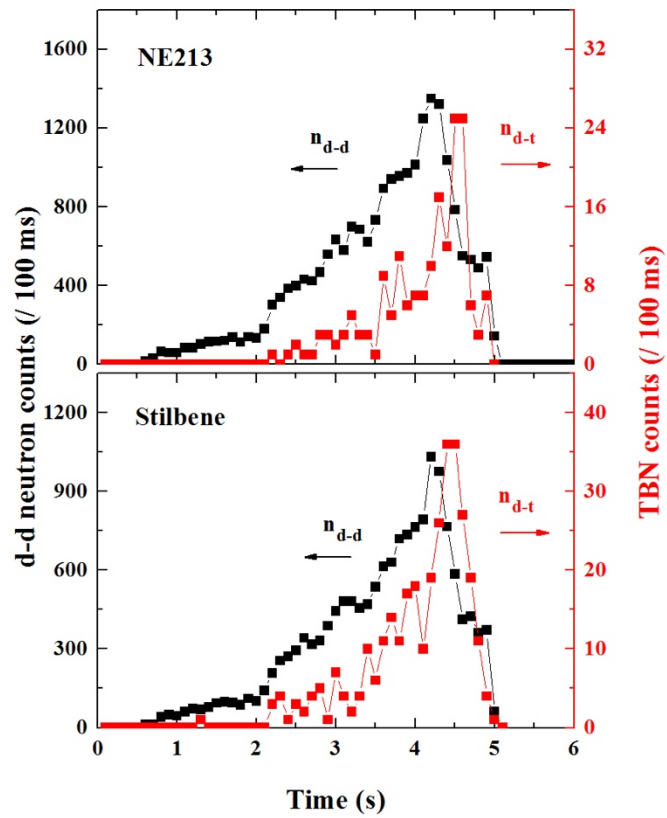
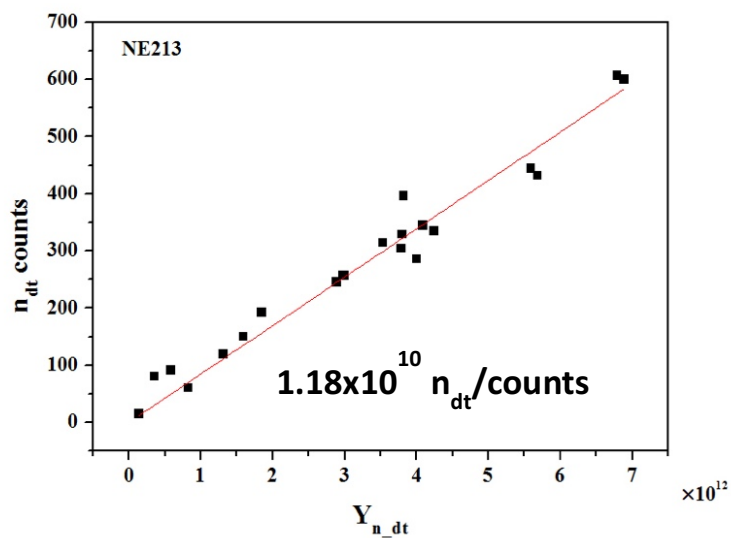


Figure 2.31 Time-resolved measurements of d-d neutron and TBN in two organic scintillators, NE213 (up) and stilbene (down).

A shot-integrated TBN signals on the NE213 detector and stilbene are compared with NAS silicon sample measurement results. As shown in Fig. 2.32 and Fig. 2.33, both detectors show good linearity with the NAS result. Based on the slope in this comparison, each detector is absolutely calibrated. Since the stilbene detector showed better counting efficiency for TBN and no spurious pulses are observed, the stilbene detector is used as main diagnostics. The d-d neutron part of stilbene is also compared with NAS indium sample measurement results and absolutely calibrated (Fig.2.34).



**Figure 2.32 Shot-integrated NE213 TBN counts versus TBN yield from NAS Si measurement.**

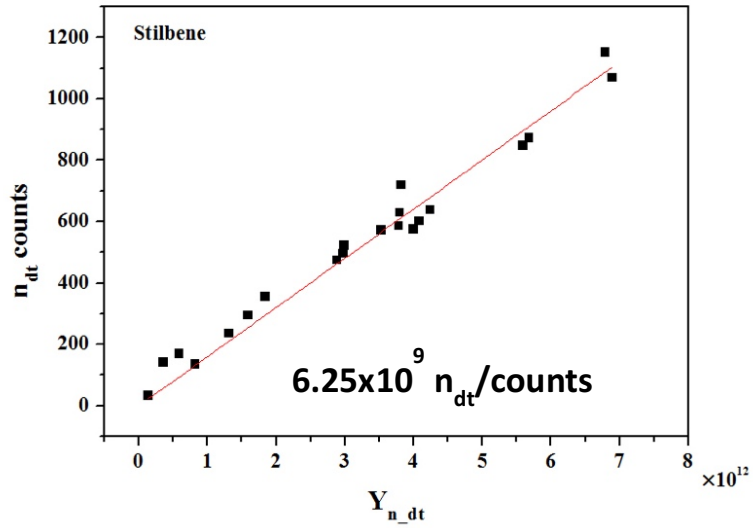


Figure 2.33 Shot-integrated stilbene TBN counts versus TBN yield from NAS Si measurement.

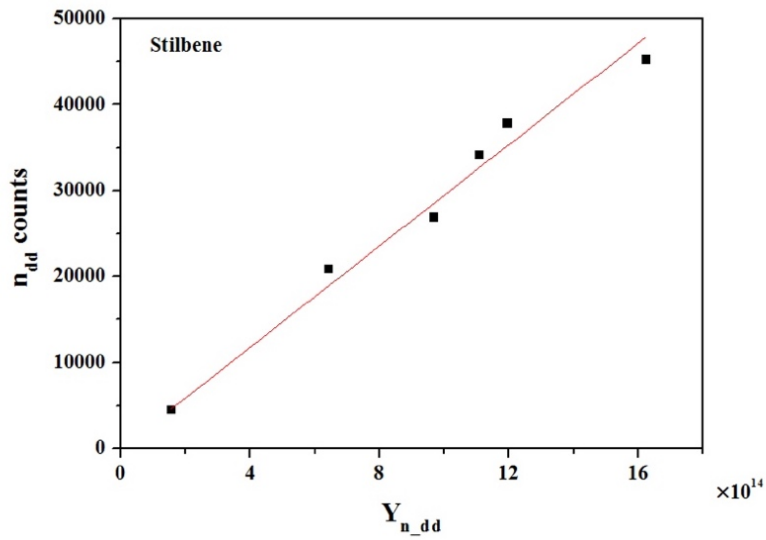


Figure 2.34 Shot-integrated stilbene d-d counts versus d-d neutron yield from NAS In sample measurement.

### 2.2.3. Scintillating fiber detector

For cross-check purpose and future better time-resolution triton burnup neutron diagnostics development [52], scintillating fiber detectors are installed and operated in KSTAR. A scintillating-fiber (Sci-Fi) detector has been successfully operated in TFTR, JT-60U and LHD [16, 24, 27, 51-54]. Due to its geometrical properties, high energy neutron which is incident on axial direction can produce larger pulse signal compared with d-d neutron, gamma-ray and obliquely incident d-t neutron (Fig. 2.35) [51]. Based on this characteristics, not only global triton burnup neutron emission rate measurement, with the collimator it can measure triton burnup neutron emission spatial profile.

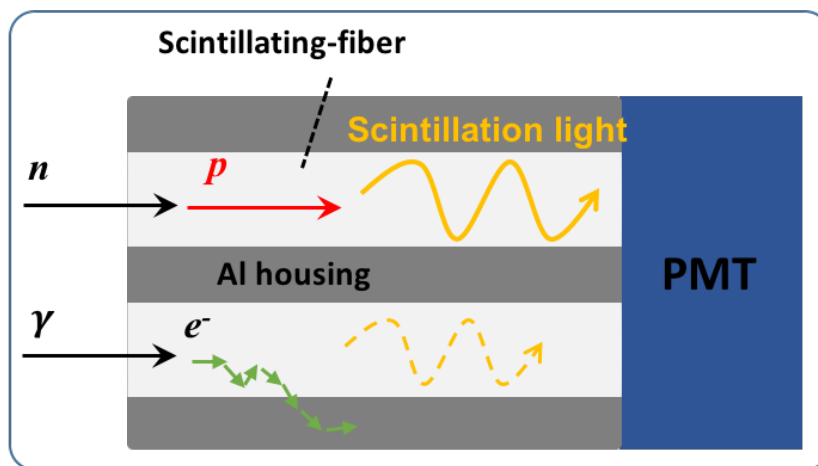
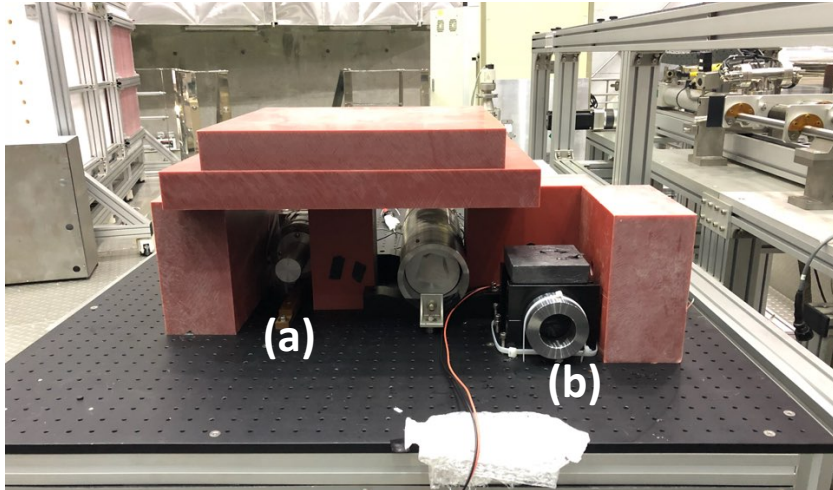


Figure 2.35 Schematic diagram for operation principle of scintillating fiber detector.

Two Sci-Fi detectors are installed in front of D-port (Fig. 2.36. 'd' position in Fig. 2.20). One is the same Sci-Fi detector which was operated successfully in JT-60U [16, 51, 54] and LHD. Since it is developed in Los Alamos National Laboratory, it is dubbed with LANL Sci-Fi (Fig. 2.37). The head part of the LANL Sci-Fi has 91 fibers whose diameter and length are 1 mm and 100 mm respectively are embedded inside the aluminum substrate. For photo-detector, Hamamatsu R2490-05 PMT which is surrounded by 10 mm thickness soft-iron magnetic shielding is used. In the LANL Sci-Fi, active phototube base is utilized. Due to this reason it consumes large electric power ( $\sim 2,000$  V and 10 mA). In order to match the power consumption of the PMT with maximum output power of HV power supply, and match the input range of the digitizer the anode output signal is fed into the digitizer via 10 times amplifying PM-amp (REPIC RPN-091). The operating bias voltage setting for the LANL Sci-Fi PMT is -1100 V.



**Figure 2.36** Photos of installed scintillating fiber detectors (a) LANL Sci-Fi and (b) Toyama Sci-Fi



**Figure 2.37** Photo of LANL Sci-Fi detector

The other Sci-Fi detector is developed by National Institute of Technology, Toyama College and National Institute for Fusion Science (Fig. 2.38). It is dubbed with Toyama Sci-Fi. Based on the neutron irradiation test and neutronics calculation the Sci-Fi head has more optimized size [53]. In the head part of the Toyama Sci-Fi, 100 scintillating fibers whose diameter and length are 1 mm and 50 mm respectively are embedded inside the aluminum substrate. For photo-detector Hamamatsu H11934-100-10 PMT is used with the bias voltage of -575 V. The PMT is surrounded by 10 mm thickness soft iron for magnetic field shielding. It is also operated with 10-times amplifying PM-amp (REPIC RPN-091) in order to reduce the bias voltage and minimize gain shift on the PMT.

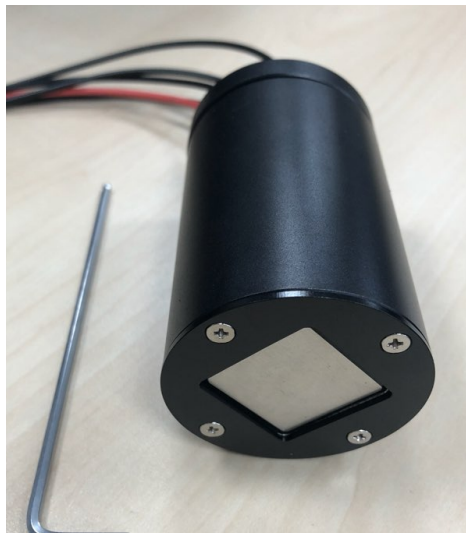


**Figure 2.38 Photo of Toyama Sci-Fi detector**

In the Sci-Fi detector, triton burnup neutron signal can be discriminated by setting appropriate discrimination level in the pulse height. In order to determine the discrimination level, operation result of each Sci-Fi detector is compared in the different plasma discharge scenarios, Ohmic discharge, NB heated discharges with different plasma current. In the Ohmic discharge, the amount of d-d fusion neutron production (also 1 MeV triton production) is much lower than NB heated plasma. Therefore, negligible high pulse height signals are expected in the Ohmic discharge. On the other hand, in the NB heated plasma discharge with the higher plasma current, relatively large amount of high pulse height signals is expected compared with the lower plasma current discharge.

Pulse height spectra of LANL Sci-Fi detector in three discharges are shown in Fig. 2.39. One is Ohmic discharge (#21738), the others are NB heated discharges with  $I_p$  of 0.5 MA (#21678) and 0.7 MA (#21695). Since the total number of pulse counts on LANL Sci-Fi in three discharge condition is different, each pulse height spectrum is normalized with the maximum pulse counts in each spectrum. In the Ohmic discharge there is nearly no pulse counts whose pulse height exceeds 0.15 V. In the NB heated plasma discharge with the higher  $I_p$  case (0.7 MA) however, there are pulse counts over 0.15 V. In the lower  $I_p$  case (0.5 MA), possibly due to the higher prompt loss characteristics, the pulse counts over 0.15 V are not clearly shown.

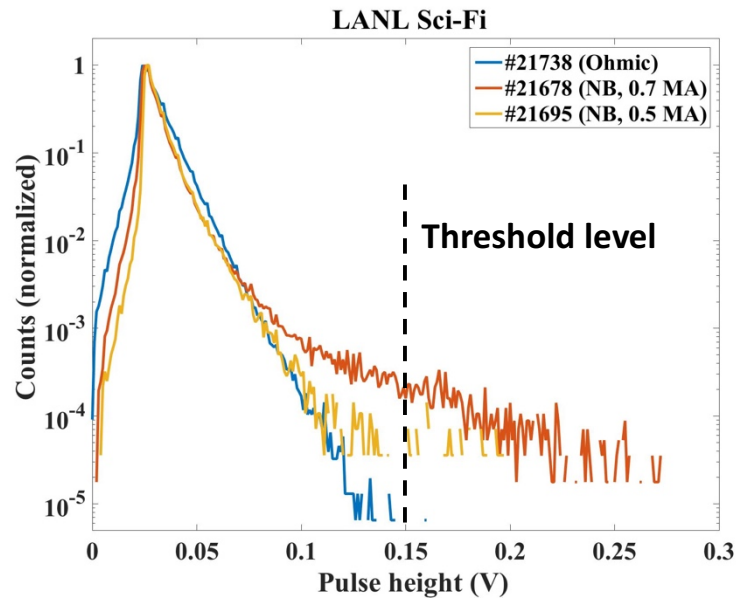
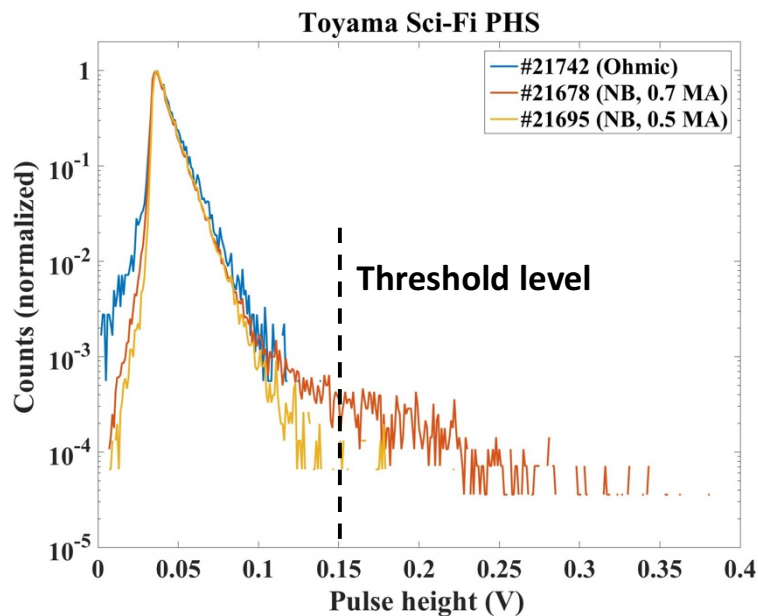


Figure 2.39 Shot-integrated pulse height spectra of LANL Sci-Fi detector on three different plasma discharge scenarios. In NB-heated discharge with  $I_p$  of 0.7 MA showed clearly different pulse height spectrum. Based on this difference, threshold level for triton burnup neutron signal is determined.

Similar characteristics is also shown in the Toyama Sci-Fi detector (Fig. 2.40). In the Ohmic discharge case, there is nearly no pulse counts over 0.15 V. On the other hand, in the NB heated plasma discharge with the higher  $I_p$  case pulse counts over 0.15 V are found. In the Toyama Sci-Fi case, since active phototube base is not used, there was large amount of gain shift in the discharge #21738, thus another Ohmic discharge (#21742) is used instead.



**Figure 2.40 Shot-integrated pulse height spectra of Toyama Sci-Fi on three different plasma discharge scenarios. Similar with LANL Sci-Fi result, in the NB-heated discharge with  $I_p$  of 0.7 MA showed clearly different pulse height spectrum. Based on this difference, threshold level for triton burnup neutron signal is determined.**

Based on the above comparison result, the discrimination level for TBN is determined as 0.15 V for both detectors. Shot-integrated TBN signals on the LANL Sci-Fi and Toyama Sci-Fi are compared with NAS silicon sample measurement results. As shown in Fig. 2.41 both detectors show good linearity with the NAS result. Based on the slope between the NAS silicon sample result and the Sci-Fi result, each detector is absolutely calibrated.

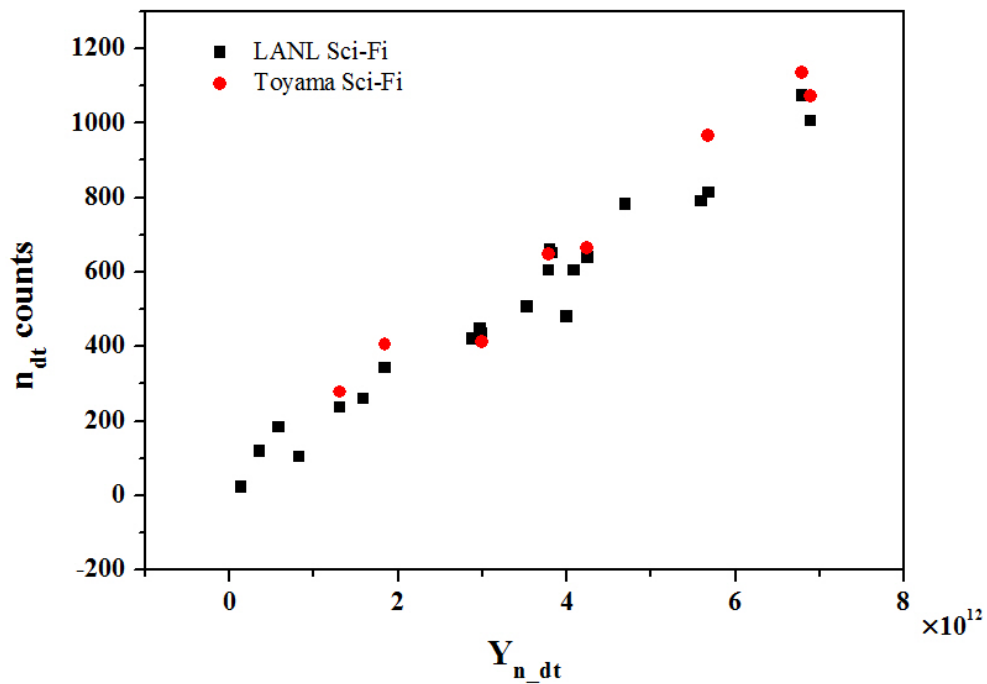


Figure 2.41 Shot-integrated TBN counts of LANL Sci-Fi and Toyama Sci-fi versus TBN yield from NAS Si measurement.

## **Chapter 3. Triton burnup analyses tools**

### **3.1. Prompt loss calculation**

#### **3.1.1. Lorentz Orbit code**

In KSTAR, the usual plasma current level is not sufficient to make prompt loss level negligible. Thus the evaluation of prompt loss is carried out in realistic way by using full gyro orbit following code. The Lorentz Orbit (LORBIT) code [32] utilized in this purpose. A full gyro orbit of fast particle under collisionless condition in the plasma equilibrium is found by numerically solve the Lorentz equation using the Runge-Kutta-Verner method. The original LORBIT code is modified and improved by Dr. T. Rhee of National Fusion Research Institute for application purpose in KSTAR. Fig. 1.1 in the Chapter 1 is also calculated by LORBIT code.

The plasma equilibrium and initial condition of 1 MeV triton are used as inputs for LORBIT code. In the initial condition of the triton, birth position and velocity distribution of test tritons are contained. The orbit calculation of a triton is finished when the triton heats the plasma facing components or pre-determined orbit following calculation time is over. The pre-determined orbit following time is 0.1 ms in the all LORBIT calculation in the present study. The orbit calculation is carried out on 680 positions in a poloidal cross-section; radial positions from 1.3 m to 2.25 m with 0.05 m interval and vertical position from -0.9 m to 0.75 m with 0.05 m interval. In each position, the orbits of 1,000 test tritons are calculated with isotropic velocity distribution by using random number generation.

For each test tritons, prompt-loss or confine is determined then the confined fraction in each position is statistically evaluated.

### 3.1.2. Confined fraction calculation result

The confined fraction calculation is carried out in plasma discharge #21695, 7.4 s timing. It is neutral beam heated discharge with  $I_p$  of 0.5 MA. A confined fraction is calculated on 680 points in a poloidal cross-section and the confined fraction for the remained part of the poloidal cross-section is evaluated by the interpolation. Confined fraction distribution on the poloidal plane is shown in the Fig. 3.1-(a). The confined fraction value is represented with color and the value is evaluated at the birth position of triton, not the guiding center. In Fig. 3.1-(b), plasma equilibrium data with same timing is shown. As shown in Fig. 3.1, the confined fraction is not a function of a flux surface.

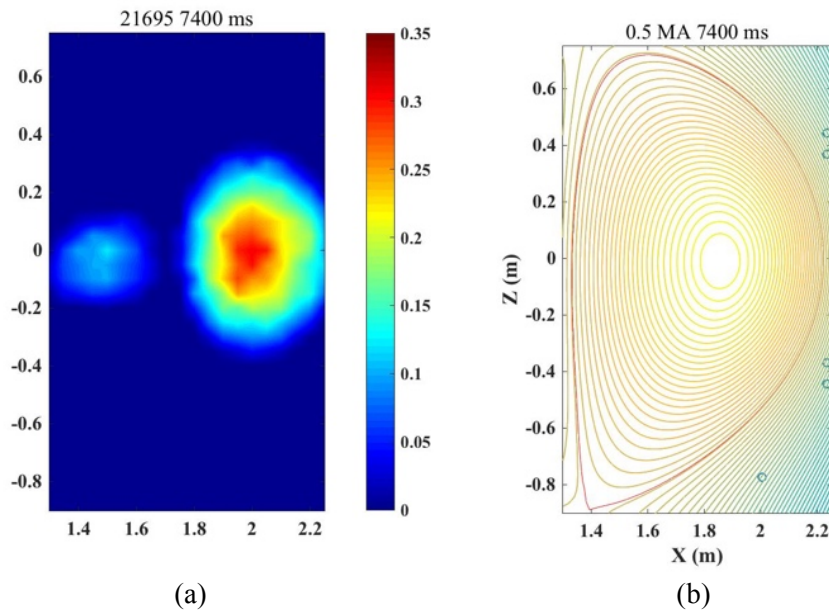


**Figure 3.1 (a) Calculated confined fraction distribution in poloidal cross-section (interpolated result based on the calculated confined fraction on 680 positions) at KSTAR #21695, 7400 ms. The horizontal axis is radial position (m) and vertical axis is vertical position (m). (b) Plasma equilibrium at this timing.**

In the same way, confined fraction calculation is carried out on different  $I_p$  cases. Confined fraction distributions on the poloidal plane under  $I_p$  of 0.4 MA, 0.6 MA and 0.9 MA are shown in Fig. 3.2. In the 0.4 MA case, the area that the triton can be confined is reduced compared with 0.5 MA case. Only in the low field side the triton can be confined. As  $I_p$  increases confined area increases and the maximum value of the confined fraction increases also.

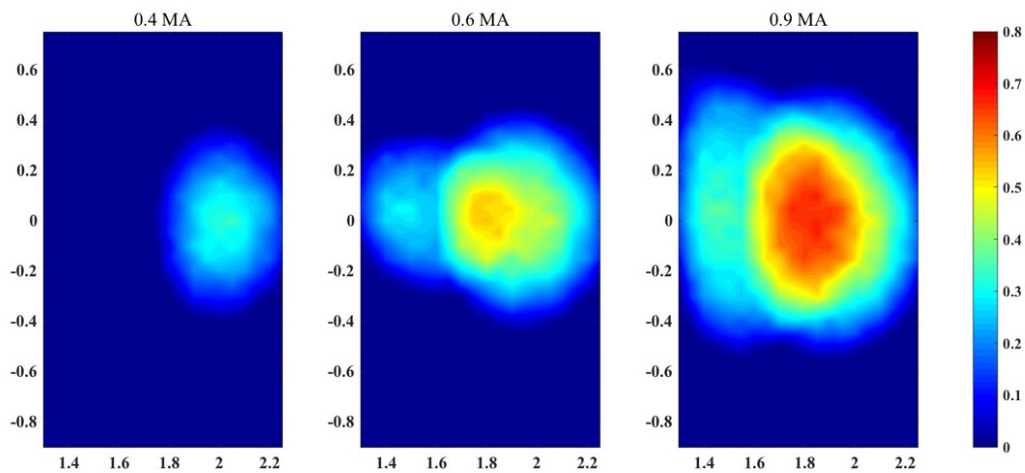


**Figure 3.2** Calculated confined fraction distribution in poloidal cross-section (interpolated result based on the calculated confined fraction on 680 positions) in different plasma current cases (0.4 MA: #21756, 8900 ms, 0.6 MA: #21629, 5650 ms, 0.9 MA: #21655, 8800 ms). The horizontal axis is radial position (m) and vertical axis is vertical position (m).

The confined fraction figure also can be plotted as a function of test triton pitch and radial position at a specific vertical position. The confined fraction according to the pitch and radial position at the horizontal plane ( $Z=0$ ) is shown in the Fig. 3.3. It is also interpolated result of the calculation result of 1000 test tritons in the each selected position. As shown in Fig. 3.2, in the high field side, only counter-going passing particles and, in the low field side only co-going passing particles can be confined [49]. A trapped triton case, due to its large drift orbit size, it cannot be confined in the plasma.

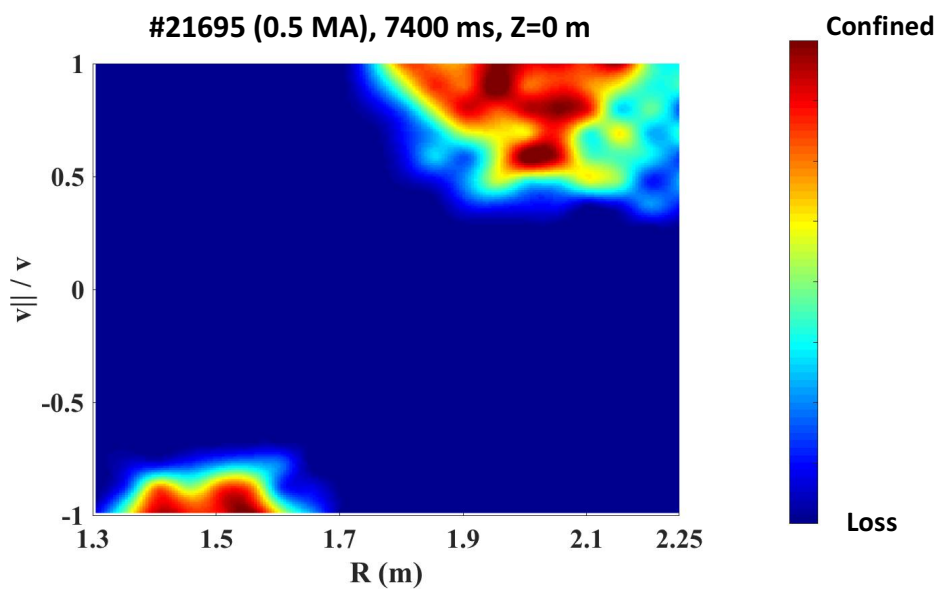


**Figure 3.3** Interpolated result of calculated confined fraction distribution as a function of pitch and radial position at the  $z=0$  position (discharge #21695, 7.4 s).

The confined fraction according to pitch and radial position at the  $z=0$  plane in the 1 MA plasma current case (#21683, 6.790 s timing) is shown in the Fig. 3.4. The confined pitch area is much larger than the 0.5 MA case. Similar with the 0.5 MA case, in the high field side only counter-going passing particles, and in the low field side co-going passing particles can be confined. In the core region, both co-going and counter going passing particles can be confined. Some tritons with stagnation orbit also can be confined near the core region. For the trapped triton case, it is still hard to be confined.

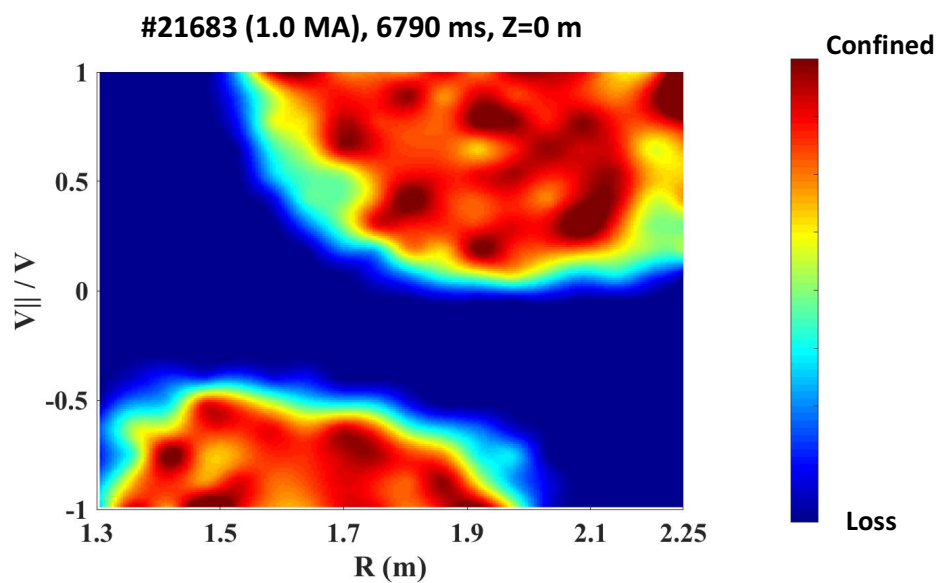


**Figure 3.4 Interpolated result of calculated confined fraction distribution as a function of pitch and radial position at the  $z=0$  position (discharge #21683 6.790 s).**

In the most of plasma parameter profiles such as  $n_e$  and  $T_e$  are provided as a function of flux surface. In order to match the data format with other plasma parameters, average confined fraction on each flux surfaces are evaluated. A confined fraction on the specific positions on a particular flux surface is evaluated by interpolation of the calculated confined fraction on the 680 positions. The average confined fraction on the flux surface is evaluated by averaging the interpolated confined fraction values at the points on the flux surface. The example of the calculated average confined fraction profile according to the normalized effective radius (square root of normalized toroidal flux) is shown in Fig. 3.5.

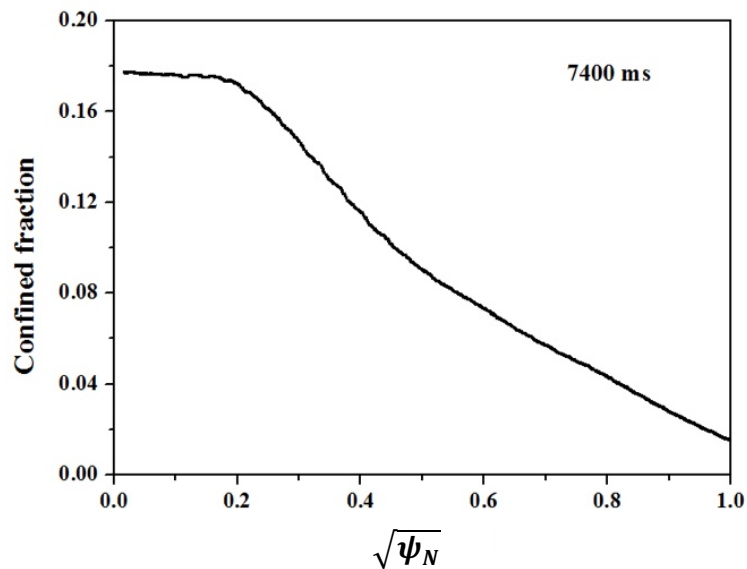


**Figure 3.5 Evaluated confined fraction profile according to effective plasma radius (#21695 7400 ms).**

Based on the calculated confined fraction profile and assumed triton birth profile, total confined fraction in the whole plasma is evaluated. In the evaluation five different  $I_p$  discharges are selected. For the triton birth profile, two different profiles are assumed based on the JET neutron camera measurement result [77]. The evaluated total confined fractions are shown in Fig. 3.6. As shown in Fig. 3.6, similar with other device result [9], as plasma current increase total confined fraction increase. In the 1 MA current case with triton birth profile of peaking factor 8, the total confined fraction of triton is about 60%. In the 0.4 MA case, the confined fraction value drops up to ~10%. For the broad triton birth profile case with the same confined fraction profile, it showed lower total confined fraction value.

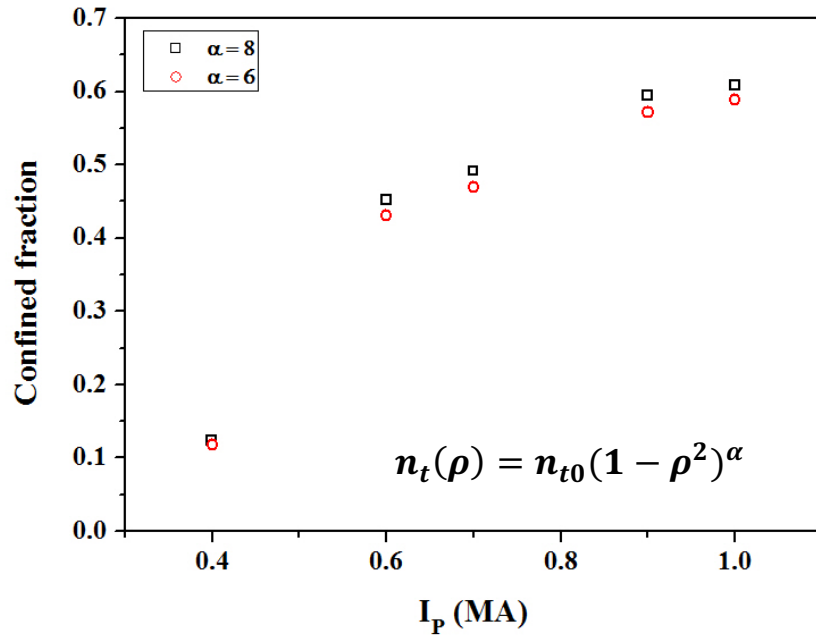


Figure 3.6 Estimated total confined fraction according to plasma current. Two kinds of peaking values for triton birth profile are assumed.

## 3.2. Slowing down and burnup calculation

### 3.2.1. Governing equation and calculation scheme

The total triton burnup neutron yield ( $Y_{n-dt}$ ) can be evaluated as multiplication between confined triton density ( $n_t$ ) and the number of expected d-t fusion reactions until thermalize ( $P_{dt}$ ) [7, 33].

$$Y_{n-dt} = n_t P_{dt} \quad (3.1)$$

The confined triton density ( $n_t$ ) can be determined by the product of the confined fraction ( $f_c$ ) and triton birth profile ( $t_{birth}$ ).

$$n_t = t_{birth} \cdot f_c \quad (3.2)$$

For the  $P_{dt}$  case, it can be described as follows,

$$P_{dt} = n_d \int_0^{t_{th}} \langle \sigma v \rangle dt = n_d \int_{E_0}^{E_{th}} \frac{\langle \sigma v \rangle dE}{dE/dt} \quad (3.3)$$

where  $t_{th}$  is the time required until thermalize to  $E_{th}$ ,  $E_0$  is the birth energy of the triton and  $n_d$  is the deuteron density. The deuteron density can be evaluated based on the electron density and effective ion charge ( $Z_{eff}$ ). In order to evaluate the integral term, the reactivity term and the slowing down rate have to be determined.

For the reactivity term case, it can be determined based on the beam-target reaction since the triton energy is much higher than that of background deuteron. In the background deuteron case, Maxwellian distribution with temperature  $T_i$  is assumed. The effect of deuteron beam-ion and thermalized triton is not considered in this calculation. The reactivity formula for beam-target reaction is like Eq. 3.4 [78],

$$\langle \sigma v \rangle_{bt} = \frac{1}{v_b v_{th} \sqrt{\pi}} \times \int_0^{\infty} \sigma v^2 \left[ e^{-\frac{(v-v_b)^2}{v_{th}^2}} - e^{-\frac{(v+v_b)^2}{v_{th}^2}} \right] dv \quad (3.4)$$

where  $v_{th}$  is deuteron ion thermal velocity ( $\sqrt{2T_i/m}$ ),  $v_b$  is the beam velocity and  $v$  is the relative velocity. For d-t fusion reaction cross-section, following formula is used [6].

$$\sigma(E) = \frac{S(E)}{E \exp(B_G/\sqrt{E})} \quad (3.5)$$

In the Eq. 3.5,  $E$  is the energy in the center of mass frame and  $S(E)$  is defined as,

$$S(E) = \frac{A_1 + E(A_2 + E(A_3 + E(A_4 + EA_5)))}{1 + E(B_1 + E(B_2 + E(B_3 + EB_4)))} \quad (3.6)$$

All the coefficients are described in the Table 3.1.

**Table 3.1 Coefficient for d-t fusion reaction cross-section [6]**

Coefficient	Value
$B_G$	34.3827
$A_1$	$6.927 \times 10^4$
$A_2$	$7.454 \times 10^8$
$A_3$	$2.050 \times 10^6$
$A_4$	$5.2002 \times 10^4$
$A_5$	0
$B_1$	$6.38 \times 10^1$
$B_2$	$-9.95 \times 10^{-1}$
$B_3$	$6.981 \times 10^{-5}$
$B_4$	$1.728 \times 10^{-4}$

The integrand term in the reactivity has peaked shape near the beam velocity. Therefore, with the finite integration range, the reactivity value can be evaluated. The reactivity is evaluated in the center of mass energy range of 0.5-550 keV with the  $dv$  of 1000 m/s. The variation in the reactivity value due to integral range under ion temperature of 4 keV condition is about 0.1%. For the smaller  $dv$  value, it gives no observable changes in the reactivity value.

For the slowing down term, energy loss rate due to Coulomb drag is represented as Eq. 3.7 [7, 79],

$$\frac{dE}{dt} = -\frac{\alpha}{\sqrt{E}} - \beta E \quad (3.7)$$

$$, \alpha = 1.81 \times 10^{-7} \ln \Lambda_{ii} A^{1/2} Z^2 \sum_j \frac{n_j Z_j^2}{A_j}$$

$$, \beta = 3.18 \times 10^{-9} \ln \Lambda_{ie} \frac{Z^2}{A} \frac{n_e}{T_e^{3/2}}$$

where,  $E$  is the triton energy  $T_e$  is the electron temperature in eV,  $n_e$  is the electron density in  $\text{cm}^{-3}$ ,  $A$  is the triton mass number,  $Z$  is the triton charge number and  $n_j$ ,  $Z_j$  and  $A_j$  are the ion density, mass number and charge number of  $j$  species ion respectively. The  $\ln \Lambda_{ii}$  and  $\ln \Lambda_{ie}$  are Coulomb logarithm for ion-ion and ion-electron collisions and these are determined as follows (Eq. 3.8).

$$\ln\Lambda_{ie} = 25.2 - \ln\left(\frac{n_e^{1/2}}{T_e}\right) \quad (3.8)$$

$$\ln\Lambda_{ii} = \ln\Lambda_{ie} + 9.03 - \frac{\ln T_e}{2}$$

In order to evaluate slowing down of triton in numerical way by using Eq. 3.7, finite size of  $dt$  is necessary. With the different  $dt$  size a slowing down rate with the same plasma condition is compared in Fig.3.7. The difference in the triton burnup neutron emission according to the selected time intervals is less than 0.1%.

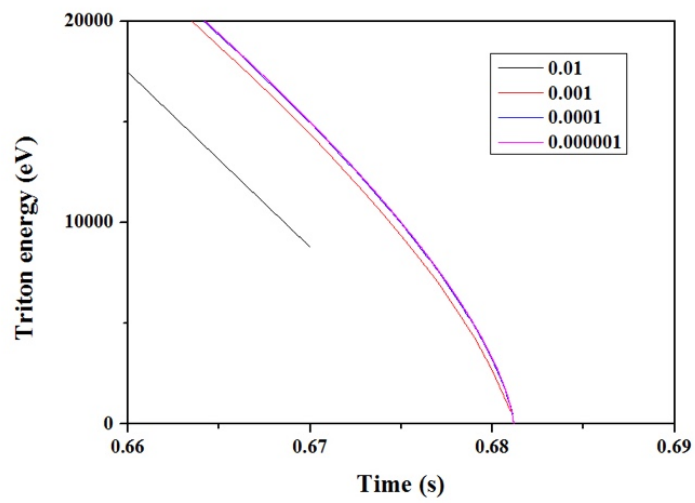
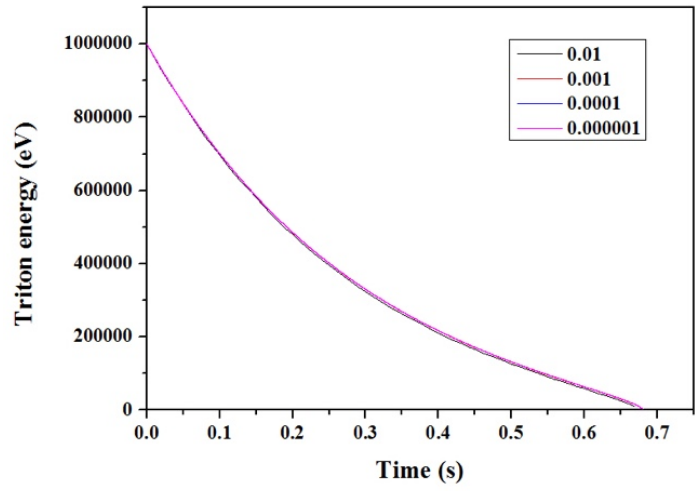


Figure 3.7 Triton energy loss rate changes according to finite 'dt' size.

### 3.2.2. Ad-hoc diffusive model

In the previous section when evaluate triton burnup neutron yield, initially confined triton remain confined until it thermalizes, i.e. it is assumed that the confinement time of fast triton is infinite. In the real situation however, it has finite confinement time and it can be degraded due to certain instability. If the confinement time is comparable or less than the slowing down time this infinite confinement time assumption is no longer adequate. The slowing down rate of triton is also can be different with the expectation from Coulomb drag. In these condition, the estimated triton burnup ratio has deviation from the measured triton burnup ratio. The deviation can be quantified by a volume averaged, effective diffusion coefficient  $D^*$  [5, 16, 28].

Based on the 1-dimensional diffusion equation in cylindrical geometry with  $D^*$ , a radial diffusion of fast triton is considered. The diffusion equation is solved numerically with the central difference method for derivative in space and Crank-Nicolson method for derivative in time.

$$\frac{\partial n(r, t)}{\partial t} = D^* \frac{1}{r} \frac{\partial}{\partial r} \left( r \frac{\partial n}{\partial r} \right) \quad (3.9)$$

In order to verify the numerical solver, the numerical solution is compared with analytic solution. The analytic solution of Eq. 3.9 which satisfying the boundary condition  $n(a) = 0$  is [80],

$$n(r, t) = n_0 J_0 \left( \frac{2.4r}{a} \right) \exp \left( \frac{-t}{\tau} \right), \quad (3.10)$$

where  $a$  is minor radius,  $J_0$  is zeroth-order Bessel function and  $\tau$  is defined by  $a^2/(2.4^2 D^*)$ . The comparison result is shown in Fig. 3.8. In this comparison, diffusion coefficient is  $0.1 \text{ m}^2/\text{s}$ , diffusion time step is  $0.1 \text{ ms}$  and radial step size is  $1 \text{ mm}$ . From the start of diffusion, total 5 timing result is described. After  $3 \text{ s}$  from the diffusion start the difference between numerical and analytic solutions is  $4.57\%$  in per cent and  $8.99 \times 10^{-6}$  in absolute value.

A radially diffused out triton passes different flux surfaces whose plasma parameters are different. Thus the slowing down characteristics depends on the traces which a triton passes. This effect is not considered in the slowing down with ad-hoc diffusive model. Thus it can cause certain amount of systematic error. The amount of the systematic error will depend on the  $n_e$  and  $T_e$  profiles.

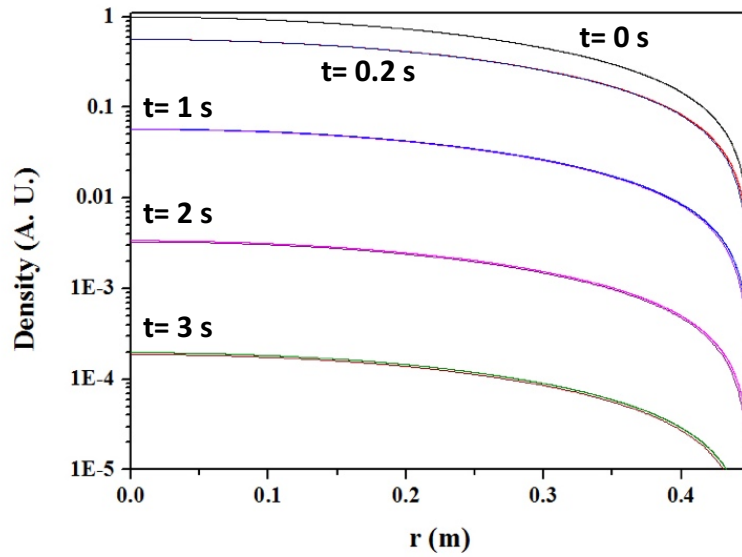


**Figure 3.8 Comparison between analytic solution and numerical solution. Diffusion coefficient is set to  $0.1 \text{ m}^2/\text{s}$ . In numerical solution, diffusion time step is  $0.1 \text{ ms}$  and radial step size is  $1 \text{ mm}$ . After  $3 \text{ s}$  from diffusion start with diffusion difference between analytic solution and numerical solution is  $4.57\%$ . Absolute difference is  $8.99 \times 10^{-6}$ .**

### 3.2.3. Slowing down and burnup calculation result

Based on the developed code, the calculation of triton burnup in different slowing down time is carried out under 0-dimension condition with the assumed plasma parameters;  $n_e$ ,  $T_i$ , and  $Z_{eff}$  are assume to be  $10^{19} /m^3$ , 1 keV and 2 respectively. The calculation is started with the initial confined triton density ( $n_t$ ) of  $5 \cdot 10^{10}/m^3$ . In order to modify the slowing down time,  $T_e$  is changed from 1 keV to 4 keV. The calculated slowing down and the amount of TBN emission rate is shown in Fig. 3.9. As  $T_e$  increases the slowing down time increases. In the longer slowing down time condition, the integrated area between TBN emission rate and time is larger than that of in the shorter slowing down time. Therefore, the amount of TBN yield is increased according to the increase in slowing down time. The triton burnup ratio for each case is 0.0032, 0.0078, 0.0125 and 0.0169 from shorter to longer slowing time respectively.

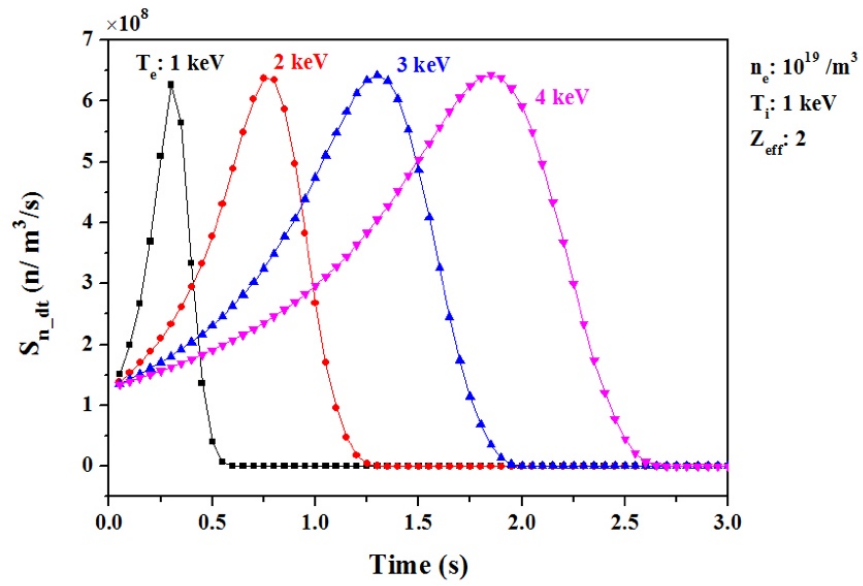


Figure 3.9 The time evolution of triton burnup neutron emission rate under 4 different slowing down time cases.

## Chapter 4. Analyses of triton burnup in KSTAR

### 4.1. Analyses of NAS measured result

A shot-integrated triton burnup ratio is evaluated based on the measured TBN yield from the NAS with silicon sample and measured total neutron yield from the stilbene detector neutron branch data. The shot-integrated value of the triton burnup ratio (TBR) is shown in Fig. 4.1. The maximum triton burnup ratio among the measured shot-integrated value is about 0.5%.

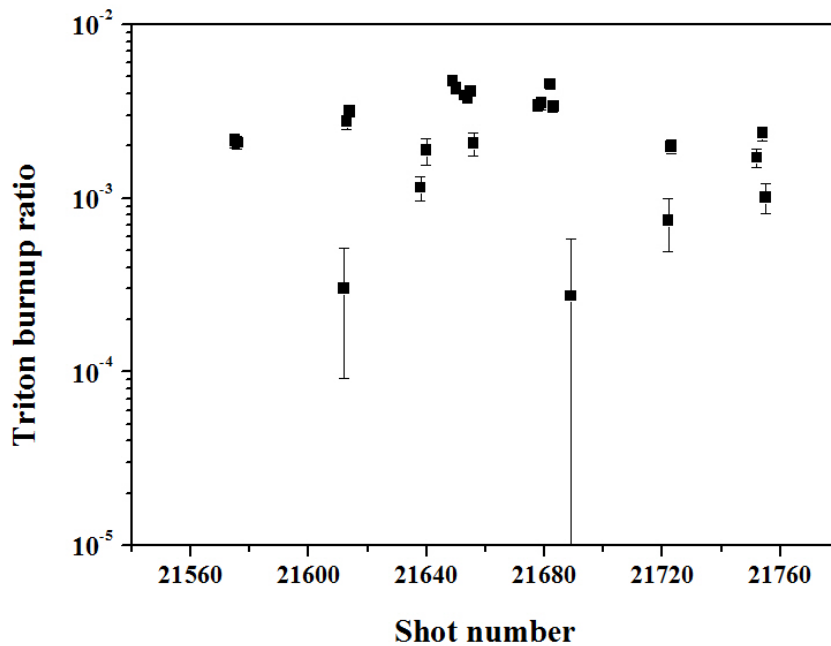
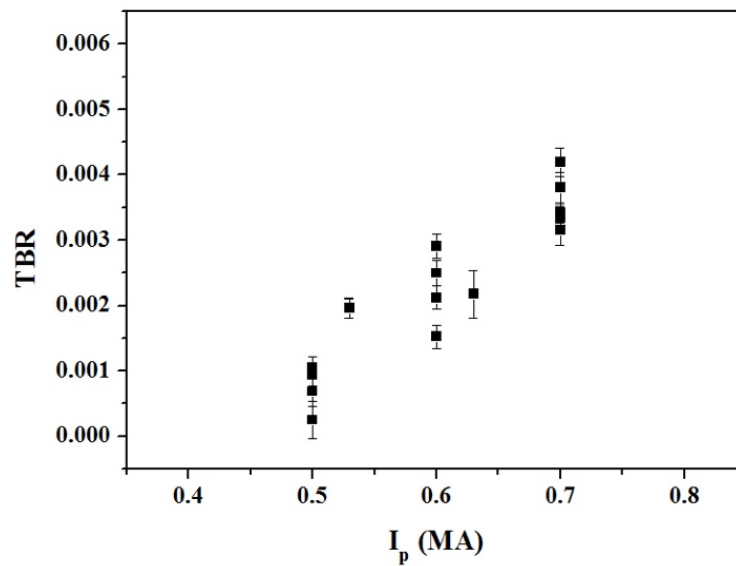


Figure 4.1 Measured triton burnup ratio from NAS silicon sample and stilbene neutron branch data.

As shown in Chapter 3, confined triton density is expected to increase with increasing  $I_p$ . Thus in the higher  $I_p$  condition the higher TBR is expected. The measured TBR is plotted according to the  $I_p$  in Fig. 4.2. Although the NAS silicon measurements were carried out only limited ranges of  $I_p$  (the operation of NAS is not automated), the increase tendency in TBR with increasing  $I_p$  is clearly shown.



**Figure 4.2 Measured triton burnup ratio as a function of plasma current. For  $I_p$ , flat-top region value is used.**

In the same  $I_p$  condition, there is variations in TBR. In classical theory, TBR depends also on the slowing down time. If TBR plot according to classical slowing down time in each  $I_p$  condition show good linearity, the variation could be mainly caused by different slowing down time in same  $I_p$  condition. In the electron drag dominant condition, the slowing down time is proportional to  $T_e^{1.5}/n_e$ . The TBN emission is also proportional to deuteron density. Deuteron density is a fraction of electron density. In the same effective ion charge ( $Z_{eff}$ ) condition, deuteron density and electron density dependence can be eliminated. Then the slowing down is a function of  $T_e$  only. In Fig. 4.3, TBR is plotted according to the averaged value of core region  $T_e$  during the discharge duration. Generally, the higher  $I_p$  and  $T_e$  show the higher TBR. In the same  $I_p$  condition however, the dependence on  $T_e$  is not clearly shown. Thus the variation in TBR under same  $I_p$  condition might be mainly caused by combined effect among the different current density profile, triton birth profile as well as MHD events during the discharge. Since NAS is shot-integrated measurement, there is clear limitation in identifying parametric dependence. In the next section by using time resolved TBR data from the stilbene detector, more precise analyses are carried out.

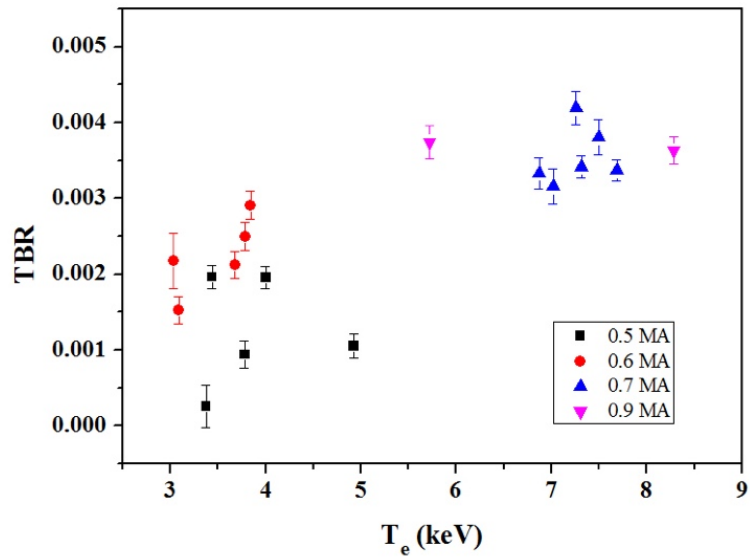
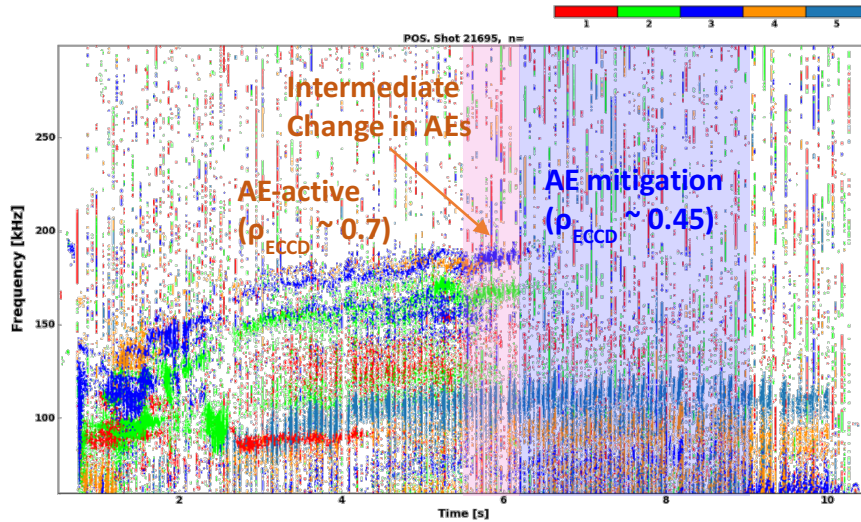


Figure 4.3 Measured triton burnup ratio as a function averaged value of core region  $T_e$  during the discharge duration ( $T_e$  from Thomson scattering measurement at core region).

## 4.2. Analyses of the scintillation detector result

As described in the Chapter 2, the organic scintillator can measure d-d neutron and TBN without changing the detector setting. Therefore, time evolution of TBR can be determined by one detector. By using measured time evolution of TBR, more reliable comparison with estimated TBR based on the classical theory is possible. For measured time evolution of TBR stilbene detector data is used, since stilbene detector showed stable operation and better  $n/\gamma$  ratio (0.95) compare with the NE213 detector (0.4).

The analyses are carried out on the discharge #21695 which is Alfvén instability control experiment by applying electron cyclotron resonance heating (ECH) at specific position [81]. In this discharge  $I_p$  and  $B_t$  are 0.5 MA and 1.8 T respectively and sawteeth and strong tearing modes are avoided. Two NB sources are injected whose acceleration voltages are 80 and 90 keV respectively, and the total injected NB power is 2.9 MW. By changing electron cyclotron current drive (ECCD) location from  $z=30$  cm (1.5-5.0 s) to  $z=15$  cm (5.5-9.0 s) at the EC resonance layer, Alfvén eigenmodes (AEs) are mitigated (Fig. 4.4).



**Figure 4.4 Spectrogram of Mirnov coil in KSTAR discharge #21695 [81]**

In this discharge measured result of stilbene detector is shown in Fig. 4.5. The black solid square, green solid triangle and red solid circle represent total neutron emission rate, TBN emission rate and triton burnup ratio respectively. In the AE active phase, beam ion confinement degraded and neutron rate drops about half. In this timing, strong loss signal is also observed in the fast ion loss detector (FILD). When the ECCD location changes from  $z=30$  cm to  $z=15$  cm, AE mitigated and beam ion confinement recovered then neutron rate also recovered and loss signal in FILD is reduced [81]. For TBN emission rate also increased in the AE mitigated phase. The changes in 1 MeV triton confinement characteristics between two phases can be compared by the TBR value in each phase. In the AE mitigated phase, TBR clearly increased thus 1 MeV triton confinement characteristics is also improved in the mitigated phase.

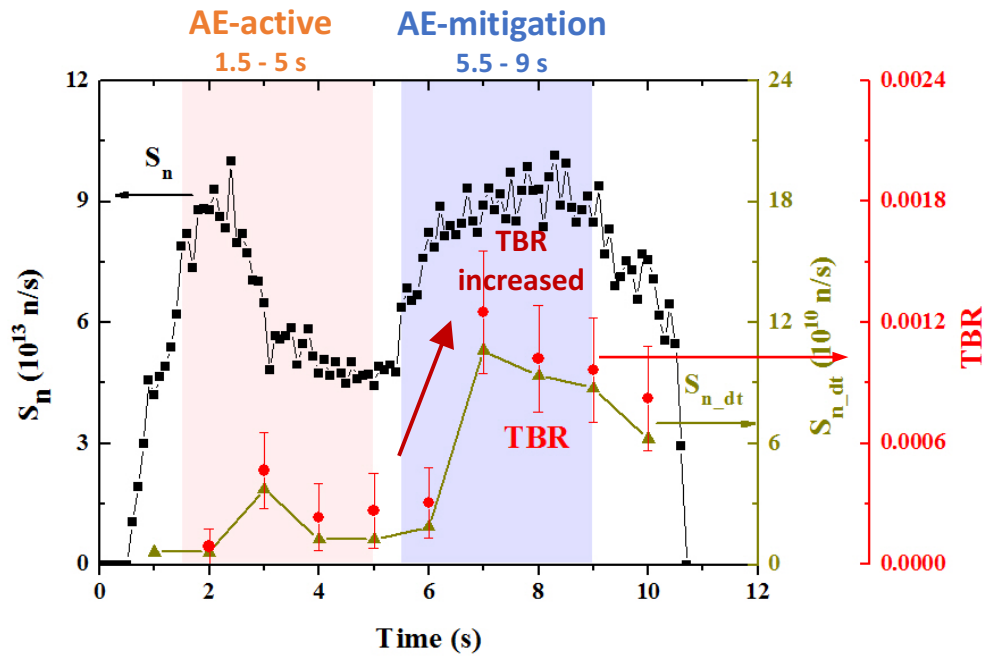


Figure 4.5 Measured time evolution of total neutron emission rate, triton burnup neutron emission rate and triton burnup ratio in discharge #21695.

The measured TBR analyses are carried out at the mitigated phase. In this phase, there is no strong MHD instabilities such as AE, sawteeth and TMs, thus estimated TBR by the two analyses codes (Chapter 3) is expected to be consistent with measured TBR. The analysis is carried out at 7.4 s timing. The plasma parameters which required for triton burnup calculation at this timing are shown in Fig. 4.6. Electron temperature and density are measured by Thomson scattering system and ion temperature is measured by charge exchanges recombination spectroscopy. Triton confined fraction profile is evaluated by LORBIT code and plasma equilibrium at this timing. For plasma equilibrium, kinetic

EFIT data is used. Triton birth profile is determined based on the calculated normalized d-d fusion reaction profile by TRANSP code [82] (d-d neutron emission profile is not measured in KSTAR) and measured d-d fusion neutron emission rate from stilbene detector. The effective ion charge is assumed to be 2. Since the TBN emission at certain timing is also affected by the tritons which are produced prior to that timing, it is assumed that the plasma condition is stable for 0.6 s which is the slowing down time at this plasma condition.

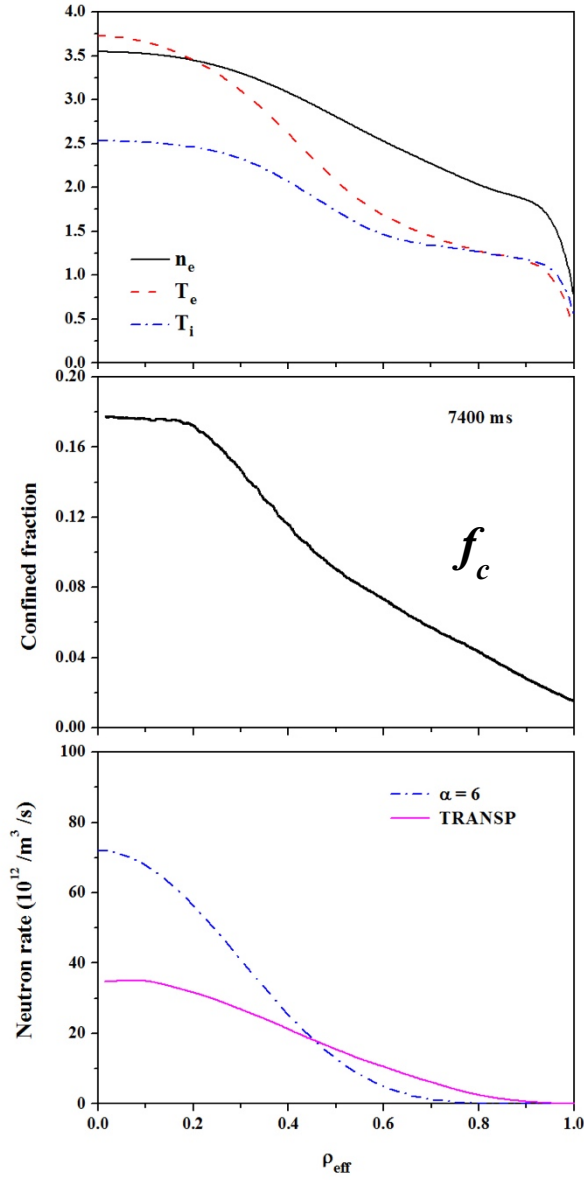
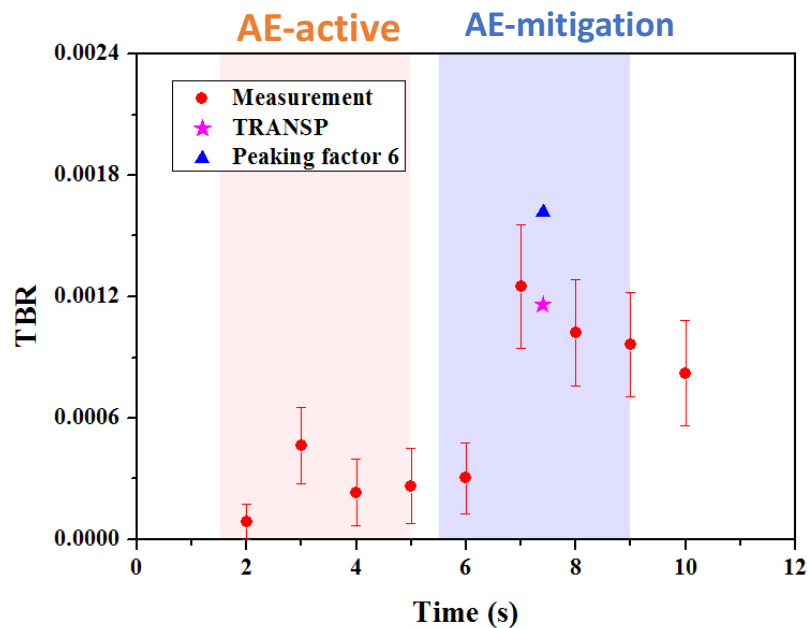


Figure 4.6 Input plasma parameters at 7.4 s. From the top to bottom,  $n_e$  ( $10^{19}/\text{m}^3$ ),  $T_e$  (keV),  $T_i$  (keV), 1 MeV triton confined fraction profile, d-d neutron rate profiles (triton birth profiles) (TRANSP result and peaking factor 6 assumed result) according to normalized effective radius.

Based on the plasma parameters (Fig. 4.6) and above mentioned assumptions, triton burnup neutron emission is calculated and by using measured d-d neutron emission rate at this timing, estimated TBR is finally evaluated. The calculated result is shown in Fig. 4.7. As shown in Fig. 4.7, the estimated TBR is consistent with measured TBR within experimental error. The total prompt loss rate in this condition is reached up to 87%. As shown in the Fig. 4.6 confined fraction profile plot, it is peaked shape near the core region. Thus not only confined fraction profile but also triton birth profile sensitively affects to the evaluation of the estimated TBR. If we use unreliably assumed triton birth profile, such as peaking factor 6 which was measured d-d neutron emission profile at the JET NB heated plasma [77], the estimated TBR deviate from the measured value (Fig. 4.7).



**Figure 4.7 Measured and calculated TBR in 7.4 s. Only random error from stilbene detector is considered in the measured TBR error.**

The AE active phase is also analyzed similar way with the AE mitigated phase. The target timing is 4.450 s. The plasma parameters are shown in Fig. 4.8. In this phase due to degradation in the beam-ion confinement, the triton birth profile is much more flattened. In order to evaluate beam ion confinement under AE condition, first NOVA code identifies the eigenmodes, then kick [83] and TRANSP combination simulate the beam ion behavior under AE condition [84]. The calculated d-d fusion reaction profile by the kick and TRANSP combination is used for the the triton birth profile. Also due to the degradation in beam-ion confinement, non-inductive current drive characteristics changes [84]. As a result, the current density profile became weakly reversed sheared profile, and the confined fraction profile degraded about half compared with the mitigated phase.

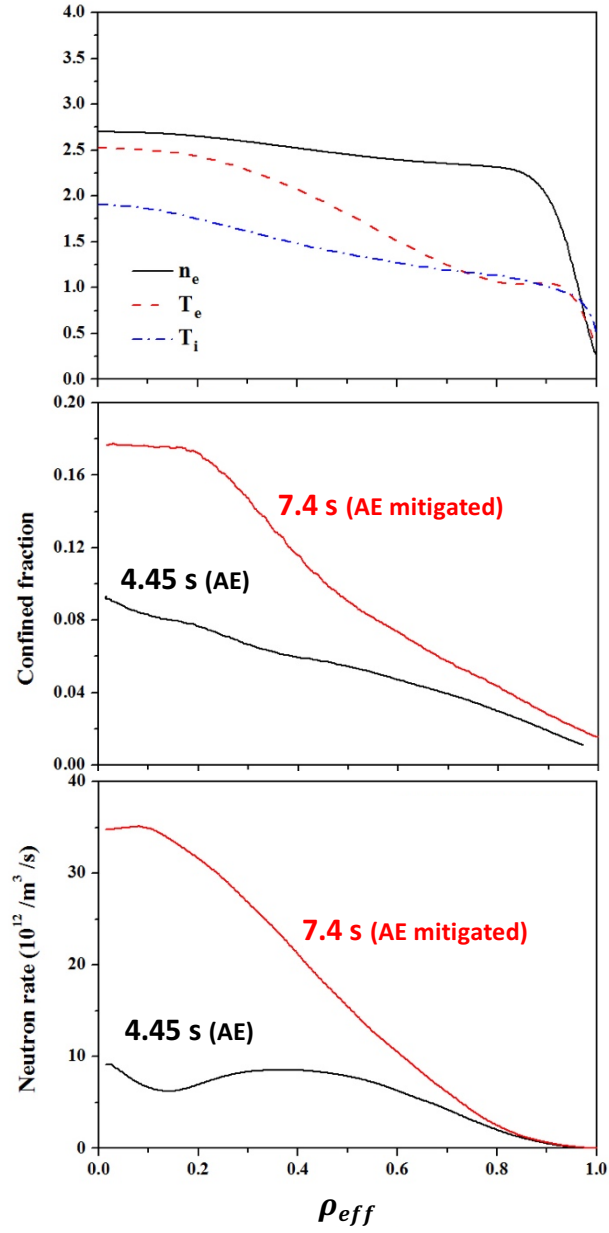


Figure 4.8 Input plasma parameters at 4.45 s. From the top to bottom,  $n_e$  ( $10^{19}/m^3$ ),  $T_e$  (keV),  $T_i$  (keV), 1 MeV triton confined fraction profiles, and d-d neutron rate profiles (triton birth profiles) according to normalized effective radius.

The estimated TBR at this timing is shown in Fig. 4.9. The estimated value is about 1.8 times larger than the measured value. The difference in the TBR between AE active and mitigated phase can be mostly explained by changes in classical parameters.

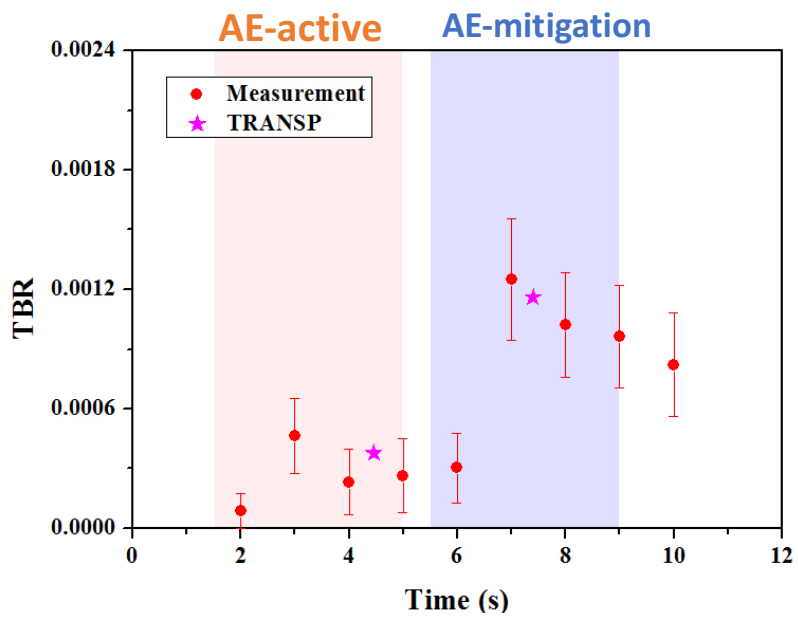


Figure 4.9 Measured and calculated TBR in 4.45 s (AE active phase).

## Chapter 5. Summary and conclusion

In order to experimentally study the confinement of 1 MeV triton based on the burnup method, d-d fusion neutron and triton burnup neutron (TBN) diagnostics are developed and triton burnup analyses codes are prepared.

Two kinds of diagnostic techniques are utilized. One is neutron activation system (NAS) which measure shot-integrated absolute neutron yield, and the other is scintillation detector which measure the time evolution of triton burnup neutron emission rate. The scintillation detector is absolutely calibrated by the NAS. In NAS, for d-d neutron and TBN yield measurements, indium and silicon samples are used respectively. For the silicon sample case, when evaluate the activity of neutron irradiated silicon sample, special background gamma-ray compensation method is applied, due to the exactly overlapped background gamma-ray which radiated from the surrounding structure near the counting station. Two organic scintillators are utilized in order to measure d-d neutron and TBN emission rates. Base on the d-t neutron generator test, the appropriate bias voltage level is determined. By considering the expected reliable operation regime and test operation result in KSTAR NB heated discharge, installation position and radiation shielding specifications are decided. The appropriate flash ADC based digizer is selected whose sampling rate is suitable for measurement of scintillation light from PMT, and on-board memory size is sufficient to operate under long-pulse discharge condition.

In order to analyze measured triton burnup, two kinds of codes are prepared. One is full gyro-orbit following code LORBIT [32] for prompt loss characteristics evaluation and the

other one is newly developed slowing down and burnup calculation code. By using LORBIT code and plasma equilibrium, the confined fraction profile is evaluated. Confined triton density profile is evaluated based on the confined fraction profile, normalized triton birth profile and d-d neutron emission rate. By using evaluated confined triton density and basic plasma parameter profiles TBN emission rate is calculated. Estimated triton burnup ratio is derived by the calculated TBN emission rate and measured d-d neutron emission rate.

The measured triton burnup ratio based on the NAS measurement show generally consistent result with the expectation from classical theory. Since it is shot-integrated measurements, however, many different effects are convoluted, thus more detailed analysis is hard to be carried out. By using time-resolved diagnostics, TBR value can be measured under specific plasma condition. Under stable plasma condition without strong MHD activity, the estimated TBR matched with the measured TBR within experimental error. Under Alfvénic activity condition, the estimated TBR is about 1.8 times higher than measured TBR.

From the present study, diagnostics for shot-integrated and time-resolved measurements of triton burnup neutron are established and triton burnup neutron emission from KSTAR plasma is measured for the first time. Independently operated three different diagnostics showed good matched result. The tools for measured TBR analyses are prepared and TBN emission rate calculation routine is established. Based on the codes and routine, under the stable but high prompt loss rate condition plasma, the measured and calculated TBR matched well. From this result, it might be inferred that triton prompt

loss and slowing down characteristics in KSTAR stable plasma condition can be explained by classical theory similar with previous studies in other devices. Furthermore, the analyses routine is works well in the high prompt loss condition (~87%). Under the Alfvénic activity condition, most of triton confinement degradation is caused by changes in classical parameters. It looks the effect of AEs is moderate for 1 MeV triton compare with beam-ion. In order to identify the interaction between 1 MeV triton and AEs, in-depth analysis is necessary.

In KSTAR, in addition to the beam-ion confinement experiment various high performance plasma experiments are carried out. Based on the established diagnostics and analyses tools, a database of the confinement characteristics of 1 MeV tritons can be established. The data base can be useful to estimate the interaction between background MHD activity and 3.5 MeV fusion alpha particle.

## Bibliography

- [1] B. J. Green and ITER International Team and Participant Teams, “ITER: burning plasma physics experiment”, *Plasma Phys. Control. Fusion* 45, 687 (2003)
- [2] R. B. White, E. Fredrickson, D. Darrow, M. Zarnstorff, R. Wilson, S. Sweben, K. Hill, Yang Chen, and Guoyong Fu, “Toroidal Alfvén eigenmode-induced ripple trapping”, *Phys. Plasmas* 2, 2871 (1995)
- [3] W.W. Heidbrink, G.J. Sadler, “The behavior of fast ions in tokamak experiments”, *Nucl. Fusion* 34, 535 (1994)
- [4] B. Wolle, “Tokamak plasma diagnostics based on measured neutron signals”, *Physics Reports* 312, 1-86 (1999)
- [5] H.H. Duong and W.W. Heidbrink, “Confinement of fusion produced MeV ions in the DIII-I tokamak”, *Nucl. Fusion* 33, 211 (1993)
- [6] H.-S. Bosch, G.M. Hale, “Improved formulas for fusion cross-sections and thermal reactivities”, *Nucl. Fusion* 32, 611 (1992)
- [7] P. Batistoni and Cris W. Barnes, “Computation of classical triton burnup with high plasma temperature and current”, *Plasma Phys. Control. Fusion* 33, 1735 (1991)
- [8] George H. Miley et al., “Fusion cross sections and reactivities”, University of Illinois, Urbana, Illinois, Report C00-2218-17 (1974)
- [9] C.W. Barnes et al., “Triton Burnup Measurements and Calculations on TFTR”, *Nucl. Fusion* 38, 597 (1998)
- [10] Henrik Sjöstrand et al., “Triton burn-up neutron emission in JET low current

- plasmas”, *J. Phys. D: Appl. Phys.* 41, 115208 (2008)
- [11] W.W. Heidbrink, R.E. Chrien, J.D. Strachan, “Burn-up of Fusion-produced Tritons and  $^3\text{He}$  Ions in PLT and PDX”, *Nucl. Fusion* 23, 917 (1983)
- [12] P. Colestock, J. D. Strachan, M. Ulrickson, and R. Chrien, “Confinement of Fusion-Produced Tritium in the Princeton Large Torus”, *Phys. Rev. Lett.* 43, 768 (1979)
- [13] O. N. Jarvis, “Neutron measurement techniques for tokamak plasmas”, *Plasma Phys. Control. Fusion* 36, 209 (1994)
- [14] O. N. Jarvis, “Neutron measurements from the preliminary tritium experiment at JET”, *Rev. Sci. Instrum.* 63, 4511 (1992)
- [15] S. Conroy, O. N. Jarvis, G. Sadler, G.B. Huxtable, “Time resolved measurements of triton burnup in JET plasma”, *Nucl. Fusion* 28, 2127 (1988)
- [16] T. Nishitani, M. Hoek, H. Harano, M. Isobe, K. Tobita, Y. Kusama, G. A. Wurden and R. E. Chrien, “Triton burn-up study in JT-60U”, *Plasma Phys. Control. Fusion* 38, 355 (1996)
- [17] M. Hoek, T. Nishitani, M. Carlsson, T. Carlsson, “Triton burnup measurements by neutron activation at JT-60U”, *Nucl. Instr. and Meth. in Phys. Res. A* 368, 804 (1996)
- [18] K. Tobita et al., “Loss of fast tritons in JT-60U reversed magnetic shear discharges”, *Nucl. Fusion* 37, 1583 (1997)
- [19] M. Isobe et al., “First measurements of triton burnup neutron spectra using a natural diamond detector on JT-60U”, *Fusion Engineering and Design* 34-35, 573 (1997)
- [20] M. Hoek, H.-S Bosch and W. Ullrich, “Triton burnup measurements at ASDEX Upgrade by neutron foil activation”, IPP-report, IPP-1/320 (1999)

- [21] P. Batistoni et al., “Measurements of triton burnup in low q discharges in the FT tokamak”, Nucl. Fusion 27, 1040 (1987)
- [22] P. Batistoni et al., “Triton confinement as inferred from fusion produced neutron measurements in the FT tokamak”, Nucl. Fusion 29, 1040 (1989)
- [23] M. Isobe et al., “Fusion neutron production with deuterium neutral beam injection and enhancement of energetic particle physics study in the large helical device”, Nucl. Fusion 58, 082004 (2018)
- [24] K. Ogawa et al., “Time-resolved triton burnup measurement using the scintillating fiber detector in the Large Helical Device”, Nucl. Fusion 58, 034002 (2018)
- [25] K. Ogawa et al., “Energetic ion confinement studies using comprehensive neutron diagnostics in the Large Helical Device”, Nucl. Fusion 59, 076017 (2019)
- [26] K. Ogawa et al., “Study of first orbit losses of 1 MeV tritons using the Lorentz orbit code in the LHD”, Plasma Sci. Technol. 21, 025102 (2019)
- [27] N. Pu, T. Nishitani, K. Ogawa, and M. Isobe, “Scintillating fiber detectors for time evolution measurement of the triton burnup on the Large Helical Device”, Rev. Sci. Instrum. 89, 10I105 (2018)
- [28] D. Anderson et al., “Influence of radial diffusion on triton burnup”, Nucl. Fusion 31, 2147 (1991)
- [29] G. S. Lee et al., “The KSTAR project: An advanced steady state superconducting tokamak experiment”, Nucl. Fusion 40, 575 (2000)
- [30] C.M. Muscatello et al., “Measurements of fast-ion transport by mode-particle resonances on DIII-D”, Nucl. Fusion 52, 103022 (2012)

- [31] W.W. Heidbrink et al., “An Investigation of beam driven Alfvén instabilities in the DIII-D tokamak”, Nucl. Fusion 31, 1635 (1991)
- [32] M. Isobe et al., “Lorentz alpha orbit calculation in search of position suitable for escaping alpha particle diagnostics in ITER”, J. Plasma Fusion Res. SERIES 8, 330 (2009)
- [33] K. Ogawa et al., “Time dependent neutron emission rate analysis for neutral-beam-heated deuterium plasmas in a helical system and tokamaks”, Plasma Phys. Control. Fusion 60, 095010 (2018)
- [34] M.S. Cheon et al., “Diagnostic neutron activation system for KSTAR”, JINST 7, C05009 (2012)
- [35] M. Hoek et al., “Initial results from neutron yield measurements by activation technique at JT-60U”, JAERI-M, 94-002 (1994)
- [36] L. Bertalot et al., “Calibration of the JET neutron activation system for DT operation”, Rev. Sci. Instrum. 70, 1137 (1999)
- [37] M. J. Loughlin et al., “Neutron transport calculations in support of neutron diagnostics at JET”, Rev. Sci. Instrum. 70, 1126 (1999)
- [38] T. Nishitani et al., “Absolute calibration of the JT-60U neutron monitors using a  $^{252}\text{Cf}$  neutron source”, Rev. Sci. Instrum. 63, 5270 (1992)
- [39] T. Nishitani et al., “Calibration experiment and the neutronics analyses on the LHD neutron flux monitors for the deuterium plasma experiment”, Fusion Engineering and Design 136, 210 (2018)
- [40] M. Sasao et al., “Fusion product diagnostics”, Fusion Sci. Technol.–Special Edition

- on “Plasma Diagnostics for Magnetic Fusion Research” 53, pp. 604-639 (2008)
- [41] Jungmin Jo et al., “Initial result of neutron energy spectrum reconstruction using multi-foil activation method in KSTAR”, *Fusion Engineering and Design* 136, 793 (2018)
- [42] B. Esposito et al., “Neutron spectrum measurements in DT discharges using activation techniques”, *Rev. Sci. Instrum.* 70, 1130 (1999)
- [43] John G. Kelly et al., “Benchmarking the Sandia pulsed reactor III cavity neutron spectrum for electronics parts calibration and testing”, *IEEE Trans. Nucl. Sci.* 40, 1418 (1993)
- [44] Y. Lee et al., “Preliminary study on capsule material for ITER neutron activation system” *Fusion Engineering and Design* 89, 1894 (2014)
- [45] R.A. Forrest, J. Kopecky and J.-C. Sublet, “The European Activation File: EAF-2007 neutron-induced cross section library”, UKAEA Report: UKAEA FUS 535, (2007)
- [46] Jungmin Jo et al., “Sample design and gamma-ray counting strategy of neutron activation system for triton burnup measurements in KSTAR”, *Fusion Engineering and Design* 109-111, 545 (2016)
- [47] G. Sadler et al., “Use of the  $^{28}\text{Si}(n,p)^{28}\text{Al}$  reaction for the measurement of 14 MeV neutrons from fusion plasmas”, *Rev. Sci. Instrum.* 61, 3175 (1990)
- [48] M.S. Cheon et al., “Design of ITER Neutron Activation System and Prototype Test at 2013 KSTAR Campaign”, presentation at KSTAR conference 2014, Jeongseon, Gangwon province, Republic of Korea

- [49] Jungmin Jo et al., “Triton burnup measurements in KSTAR using a neutron activation system”, *Rev. Sci. Instrum.* 87, 11D828 (2016)
- [50] T. Elevant et al., “Silicon surface barrier detector for fusion neutron spectroscopy”, *Rev. Sci. Instrum.* 57, 1763 (1986)
- [51] G. A. Wurden et al., “Scintillating-fiber 14 MeV neutron detector on TFTR during DT operation”, *Rev. Sci. Instrum.* 66, 901 (1995)
- [52] K. Ogawa et al., “High detection efficiency scintillating fiber detector for time-resolved measurement of triton burnup 14 MeV neutron in deuterium plasma experiment”, *Rev. Sci. Instrum.* 89, 10I101 (2018)
- [53] E. Takada et al., “Design optimization of a fast-neutron detector with scintillating fibers for triton burnup experiments at fusion experimental devices”, *Rev. Sci. Instrum.* 90, 043503 (2019)
- [54] T. Nishitani et al., “Triton burnup measurements using scintillating fiber detectors on JT-60U”, *Fusion Engineering and Design* 34-35, 563 (1997)
- [55] L. Giacomelli et al., “The compact neutron spectrometer at ASDEX Upgrade”, *Rev. Sci. Instrum.* 82, 123504 (2011)
- [56] Glenn F. Knoll, “Radiation Detection and Measurement 3rd Edition, Chapter 8”, John Wiley & Sons, New York (2010)
- [57] L. Giacomelli et al., “Evaluation of a digital data acquisition system and optimization of n- $\gamma$  discrimination for a compact neutron spectrometer”, *Rev. Sci. Instrum.* 82, 013505 (2011)
- [58] CAEN Application Note AN2506, “Digital Gamma Neutron discrimination with

Liquid Scintillators”

- [59] V. V. Verbinski et al., “Calibration of an organic scintillator for neutron spectrometry”, Nucl. Instr. and Meth. 65, 8 (1968)
- [60] S. Meigo, “Measurements of neutron spectra produced from a thick lead target bombarded with 0.5- and 1.5-GeV protons”, Nucl. Instr. and Meth. in Phys. Res. A 431, 521 (1999)
- [61] L. Giacomelli et al., “Neutron emission spectroscopy of D plasmas at JET with a compact liquid scintillating neutron spectrometer”, Rev. Sci. Instrum. 89, 10I113 (2018)
- [62] M. Ishikawa et al., “First measurement of neutron emission profile on JT-60U using stilbene neutron detector with neutron-gamma discrimination”, Rev. Sci. Instrum. 73, 4237 (2002)
- [63] Jungmin Jo et al., “Initial operation results of NE213 scintillation detector for time-resolved measurements on triton burnup in KSTAR”, Rev. Sci. Instrum. 89, 10I118 (2018)
- [64] K. Ogawa et al., “Progress in development of the neutron profile monitor for the large helical device”, Rev. Sci. Instrum. 85, 11E110 (2014)
- [65] J.M. Adams et al., “The JET neutron emission profile monitor”, Nucl. Instr. and Meth. in Phys. Res. A 329, 277 (1993)
- [66] M. Cecconello et al., “A neutron camera system for MAST”, Rev. Sci. Instrum. 81, 10D315 (2010)
- [67] Y. P. Zhang et al., “Development of the radial neutron camera system for the HL-2A

- tokamak”, Rev. Sci. Instrum. 87, 063503 (2016)
- [68] Yu. A. Kaschuck et al., “Neutron measurements during trace tritium experiments at JET using a stilbene detector”, 31st EPS Conference on Plasma Phys. London, 28 June – 2 July 2004 ECA Vol.28G, P-5.174 (2004)
- [69] I. Murata, Compendium of Neutron Beam Facilities for High Precision Nuclear Data Measurements (IAEA, Vienna, 2014), pp.110-118, IAEA-TECDOC-1743, <http://www-nds.iaea.org/publications/tecdocs/iaea-tecdoc-1743/>
- [70] <http://noticekorea.com>
- [71] Marek Flaska et al., “Influence of sampling properties of fast-waveform digitizers on neutron – gamma-ray, pulse-shape discrimination for organic scintillation detectors”, Nucl. Instr. and Meth. in Phys. Res. A 729, 456 (2013)
- [72] Daniele Marocco et al., “High count rate neutron spectrometry with liquid scintillation detectors”, IEEE Trans. Nucl. Sci. 56, 1168 (2009)
- [73] X.L. Luo et al., “Pulse pile-up identification and reconstruction for liquid scintillator based neutron detectors”, Nucl. Instr. and Meth. in Phys. Res. A 897, 59 (2018)
- [74] S. M. Robinson et al., “Effects of high count rate and gain shift on isotope identification algorithms”, IEEE Nuclear Science Symposium Conference Record, 1152 (2007)
- [75] X-5 Monte Carlo Team collaboration, “MCNP – a general Monte Carlo N-particle transport code, version 5”, Los Alamos National Laboratory, Los Alamos U.S.A. (2000)
- [76] Natalia Zaitseva et al., “Plastic scintillators with efficient neutron/gamma pulse

- shape discrimination” Nucl. Instr. and Meth. in Phys. Res. A 668, 88 (2012)
- [77] O.N. Jarvis et al., “Neutron profile measurements in the Joint European Torus”, Fusion Engineering and Design 34-35, 59 (1997)
- [78] Ou Wei et al., “Fusion reaction rate coefficient for different beam and target scenarios”, Chinese Phys. Lett. 32, 022801 (2015)
- [79] T. H. Stix, “Heating of toroidal plasmas by neutral injection”, Plasma Phys. 14, 367 (1972)
- [80] Kenro Miyamoto, “Plasma Physics for Nuclear Fusion”, MIT press, Cambridge, MA, (1987)
- [81] Junghee Kim et al., “Recent experiments on the ECH/ECCD-assisted Alfvén eigenmode control in KTAR”, 22nd ITPA Topical Group on Energetic Particles Meeting, Apr. (2019), Rovaniemi, Finland
- [82] R. J. Hawryluk, “An empirical approach to tokamak transport physics of plasmas Close to Thermonuclear Conditions (Brussels: CEC) vol 1, pp 19-46
- [83] M. Podestà et al., “A reduced fast ion transport model for the tokamak transport code TRANSP”, Plasma Phys. Control. Fusion 56, 055003 (2014)
- [84] J. S. Kang et al., “Numerical investigation of Alfvénic modes in recent KSTAR experiments”, 22nd ITPA Topical Group on Energetic Particles Meeting, Apr. (2019), Rovaniemi, Finland

## 국 문 초 록

# KSTAR에서의 1 MeV 트리톤 가둠 특성 연구를 위한 핵융합 중성자 측정을 이용한 트리톤 연소 해석

조 정 민

에너지시스템공학부

(핵융합 및 플라즈마 공학 전공)

서울대학교 대학원

중수소-삼중수소 핵융합 플라즈마에서의 3.5 MeV 핵융합 알파입자 가둠 특성의 이해는 내부가열이 지배적인 연소 플라즈마 (burning plasma) 달성 및, 진공용기의 손상 방지 측면에서 중요하다. 중수소 핵융합 반응으로 발생하는 1 MeV 트리톤은 그 역학적인 특성이 3.5 MeV 알파 입자와 유사하여, 알파 입자의 특정 특성을 모사하는 테스트 입자로서 효과적으로 활용될 수 있다.

발생한 1 MeV 트리톤 중 일부는 궤도의 크기가 커서 플라즈마 내부에 가뒀지 못한 채 즉각손실(prompt loss) 된다. 즉각손실 되지 않고 플라즈마 내부에 가뒀진 트리톤은 주변 플라즈마와의 쿨롱 충돌을 통해 주변 플라즈마와 열적 평형상태에 도달하게 된다. 열적 평형상태에 도달하는 도중, 주변 중수소 플라즈마와 중수소(d)-삼중수소(t) 핵융합 반응을 일으킬 수 있고,

이를 통해 14 MeV d-t 중성자(트리톤 연소 중성자)가 발생 할 수 있게 된다. 생성된 트리톤 중 약 1% 정도가 이와 같은 과정을 통해 연소되어 트리톤 연소 중성자를 발생시킨다. 중수소 핵융합의 두 가지(branch)인 트리톤 발생 가지와 중성자 발생 가지의 반응 단면적이 거의 같기 때문에, 트리톤의 생성량은 d-d 핵융합 중성자의 측정을 통해 유추 할 수 있고, 중수소 플라즈마에서의 d-d 핵융합 중성자 측정과 트리톤 연소 중성자 측정을 통해 트리톤 연소율을 구할 수 있다.

트리톤 연소 중성자의 발생은, d-t 핵융합 반응단면적의 피크 지점 에너지가 트리톤 발생 에너지인 1 MeV 보다 낮은 약 170 keV에 위치 함에 따라, 즉각손실 뿐만 아니라 열적평형에 이르는 과정에 발생한 여러 상황에 의해서도 영향을 받게 된다. 따라서 트리톤 연소율 측정을 통해 현재 플라즈마에서의 트리톤의 가둠 및 감속 특성에 대한 정보를 얻을 수 있다.

본 연구에서는 KSTAR 장치에서 진행되는 다양한 고성능 플라즈마 시나리오에서의 트리톤 가둠 특성 연구를 위하여, d-d 중성자 및 트리톤 연소 중성자 진단을 개발하였고, 특정 플라즈마 상황에서의 트리톤 연소 현상을 해석하기 위한 전산모사 코드들을 마련하였다. 개발된 중성자 진단들을 이용하여 실제 KSTAR 플라즈마 상황에서 트리톤 연소율을 측정하고, 해석 기반을 이용하여 이를 해석하였다.

진단은 크게 중성자 발생 절대량을 측정하는 진단과 시간에 따른 중성자 발생률의 변화를 측정하는 진단 두가지로 구성 되어있다. 플라즈마 방전

시간 동안 발생한 트리톤 연소 중성자 혹은 d-d 중성자의 총량은 중성자 방사화 진단을 이용하여 측정하였다. d-d 중성자 발생량은 2011년 KSTAR 캠페인때부터 인듐 시편을 통해 측정하였다. 트리톤 연소 중성자 발생량 측정은 뉴트로닉스 계산을 통해 KSTAR 상황에 적합한 시편으로 확인된 실리콘 시편을 사용하였다. 감마선 검출기가 위치한 영역에서, 방사화된 실리콘 시편에서 발생하는 측정대상 감마선과 같은 에너지의 배경 감마선이 발생하여, 시편 감마선 검출에 간섭을 줄 수 있고, 이는 또한 트리톤 연소 중성자 발생량 도출에 영향을 미치게 된다. 상시 운용되는 중성자속 모니터를 활용하여 문제가 되는 배경 감마선의 영향 정도를 배경 감마선의 별도 측정 없이 평가하는 방법을 사용하여 실리콘 시편의 방사화도 측정이 진행되었다.

트리톤 연소 중성자 및 d-d 핵융합 중성자의 발생률 측정은 섬광검출기들을 이용해 이루어졌다. 트리톤 연소 중성자와 d-d 핵융합 중성자의 동시 측정을 위해 유기섬광체를 사용하였다. 스틸벤과 NE213 두개의 유기섬광체가 독립적으로 운용 되었다. 각 유기섬광체에는 광전자증배기가 광학적으로 연결되어있다. 가속기 기반 d-t 중성자 발생장치에서의 테스트 결과를 통해, 현재 사용하는 디지털라이저의 아날로그 입력 범위에 d-t 중성자 신호가 적절하게 들어올 수 있도록 광전자증배기 이득률 값을 결정하였다. 디지털라이저는 각 트리거된 펄스들의 파형을 저장할 수 있다. 저장된 파형 정보에서 후-처리를 통해 트리거 시간, 발생한 전하,

펄스의 모양 정보가 도출된다. 전하 비교 방법을 통해 중성자와 감마선 신호를 구별하였고, 그 구별 성능은 성능지수(*figure of merit*)와 오-분류 확률을 통해 평가되었다. 전체전하  $0.6 \text{ V}\cdot\text{ns}$  이상의 범위에서 중성자 신호 영역에 감마선 신호가 포함되어 있을 확률은 0.1% 미만으로 확인 되었다.

두 섬광검출기와 더불어 트리톤 연소 중성자 측정의 교차 확인 목적 및 향후 고-시분해능 측정 준비의 일환으로 섬광파이버 검출기가 설치, 운용 되었다. 섬광파이버 검출기는 트리톤 연소 중성자에 대해서 특히 높은 펄스 신호를 발생시켜 d-d 중성자 및 감마선에 의한 신호와 분리 가능하다. 트리톤 생성량이 적어 트리톤 연소 중성자의 발생이 거의 없을 것으로 예상되는 플라즈마 상황과, 트리톤 생성량이 많고 가둠 특성이 좋아 트리톤 연소 중성자 발생 또한 많이 발생할 것으로 예상되는 플라즈마 상황에서, 펄스 파고 스펙트럼 상에 예상되는 방향으로의 뚜렷한 차이가 확인 되었고, 이를 통해 트리톤 연소 중성자 측정을 위한 신호 분리 레벨이 설정 되었다.

두 유기섬광체 및 섬광파이버 검출기로 측정한 방전시간동안 누적된 트리톤 연소 중성자 신호와, 중성자 방사화 진단을 통해 측정한 트리톤 연소 중성자 발생량 사이에 선형성이 확인되었고, 이를 통해 각 섬광검출기들이 절대 교정 되었다. 중성자 방사화 진단으로 구한 d-d 중성자 발생량과 유기섬광체로 측정한 방전시간동안 누적된 d-d 중성자 신호사이에도 선형성이 확인 되었고, 이를 이용하여 유기섬광체 검출기의 d-d 중성자 측정 영역이 절대 교정 되었다.

트리톤 연소 현상을 해석하기 위한 톨로 트리톤의 즉각손실을 계산하는 코드와 트리톤의 플라즈마 내에서의 감속과 d-t 핵융합 반응을 계산하는 코드가 마련되었다. 즉각손실은 트리톤의 자기장내에서의 자이로 모션을 전부 따라가는 Lorentz Orbit 코드와 플라즈마 평형을 이용하여 계산하였다. 각 자속표면에서의 즉각손실률은, 한 폴로이달 평면 내 680개 위치에서 통계적 방법으로 계산된 즉각손실률을 기반으로 결정되었다. 가뒀진 트리톤의 감속과 d-t 핵융합 반응의 계산은, 기존에 다른 장치들에서 활용되던 코드들을 기반으로 새로 개발한 코드를 통해 진행되었다. 이 코드에서는 기본적으로 각 트리톤들이 생성된 자속표면 위치에서 감속된다고 가정하고, 주변 플라즈마와의 쿨롱 상호작용을 통해 감속되는 상황을 모사한다. 또한 이 코드에서는 반경험적인 (semi-empirical) 방법으로 부피평균 유효확산계수를 구하여 고속-트리톤의 가둠 시간이 유한한 경우에 대해서 모사 할 수 있다.

트리톤 연소 해석 톨과 가정한 플라즈마 파라미터를 활용하여 계산한 트리톤 연소율은, 고전이론에서 예측하는 바와 같이, 플라즈마 전류가 증가할수록 그리고 트리톤의 감속시간이 길어질수록 증가하는 경향성을 보여주었다. 중성자 방사화 진단을 이용하여 측정한 결과에서도 플라즈마 전류가 증가할수록 트리톤 연소율이 증가하는 모습을 보여주었다. 하지만 같은 플라즈마 전류 상황에서도 트리톤 연소율에 있어 일정 정도 편차를 갖는 것이 확인되었다. 이는 같은 플라즈마 전류 상황에서도 플라즈마 전류

밀도 및 트리톤 발생분포가 달라, 즉각손실 정도가 크게 다를 수 있음과 추가적인 자기유체역학적 현상이 포함 될 수 있음에 지배적으로 기인하는 것으로 예측된다.

섬광검출기를 이용한 시분해 트리톤 연소율 측정 결과와 분석하고자 하는 타이밍에서의 플라즈마 파라미터들을 이용하여 좀 더 자세한 트리톤 연소 해석을 진행하였다. 대상 플라즈마는 알벤 (Alfvén) 불안정성 제어 실험이 진행된 플라즈마 방전 #21695번으로, 해석하는 시점은 불안정성이 제어된 7.4 초 시점이다. 이 시점에서는 1 MeV 트리톤의 가둠 특성을 악화시키는 강한 불안정성이 없는 상황으로, 고전이론을 기반으로 도출한 트리톤 연소율 추정치와 비교하기 적절한 플라즈마 상황이다. 이 방전의 플라즈마 전류는 0.5 MA로 즉각손실률이 클 것으로 예상된다. 해당 시점에서의 플라즈마 평형 데이터와 LORBIT 코드를 이용하여 계산한 트리톤 가둠 비율 분포와, TRANSP으로 계산된 트리톤 생성 분포, 그리고 측정된 d-d 중성자 발생률을 이용하여 이 시점에서 플라즈마에 가둬진 트리톤의 밀도,  $n_t$ 를 계산하였다. 트리톤 생성 직후 에너지보다 d-t 핵융합 반응단면적의 피크 에너지 위치가 더 낮은 곳에 위치함에 따라, 이 플라즈마에서의 트리톤 감속시간인 0.6 초 동안 같은 플라즈마가 유지 되었다는 가정으로 계산이 진행되었다. 이러한 과정을 통해 계산한 트리톤 연소율은 추정치와 측정오차 범위내에서 일치하는 결과를 보여주었다.

본 연구를 통해 KSTAR 장치에서 트리톤 연소율의 시간에 따른 변화를

측정 할 수 있는 진단 시스템을 개발하였고, 트리톤 연소를 해석할 수 있는 코드들을 마련하여 트리톤 연소 해석의 기틀을 마련하였다. 개발된 진단을 실제 KSTAR 플라즈마 방전 상황에서 운용하여 트리톤 연소율의 시간에 따른 변화를 측정하였고, 해석 툴들을 이용하여 측정 결과를 해석하였다. 강한 불안정성이 발생하지 않아 안정적인 상황이지만 즉각손실률이 약 87%로 높은 플라즈마 시점에서, 개발된 진단을 통해 측정한 트리톤 연소율과 코드들을 통해 추산한 값이 측정 오차 내에서 잘 일치하는 모습을 확인하였다. 이를 통해 다른 장치들에서 보여주었던 결과와 같이 안정적인 플라즈마 상황에서의 트리톤의 가둠 특성이 고전이론을 통해서 설명 될 수 있음을 유추 할 수 있다.

현재 KSTAR에서는 다양한 고성능 플라즈마 실험들이 진행되고 있다. 이러한 실험들에서 본 연구를 통해 개발한 진단과 해석 코드들을 활용함으로써 1 MeV 에너지를 갖는 트리톤의 가둠 특성에 대한 데이터 베이스를 정립해 나갈 수 있고, 이 데이터베이스는 각 상황에서의 3.5 MeV 알파입자 거동 유추에 유용하게 활용될 수 있을 것으로 기대한다.

**주요어:** 핵융합 플라즈마, 1 MeV 트리톤, 트리톤 연소, 트리톤 연소 중성자, d-d 중성자, 중성자 진단, KSTAR, 중성자 방사화 시스템, 섬광검출기, 플라즈마 진단, 고에너지 입자 가둠 특성

**학 번:** 2014-31126